CHAPTER 2

GF-OVJP Nozzle Design

2.1. Overview

The guard flow-enhanced organic vapor jet printing (GF-OVJP) tool is designed to deposit organic materials and control the film growth and quality via its processing parameters. GF-OVJP has many independently controllable processing parameters, including nozzle geometry, choice of carrier gas (*CG*) and guard flow (*GF*) gases, *CG* and *GF* mass flow rates, evaporation source and substrate temperatures, nozzle substrate spacing '*s*', nozzle and substrate X and Y translation speed (v_X, v_Y), some of which are shown in **Figure 2-1**. The properties of organic films grown by this technique are dependent on these parameters and the dependence relationship is the focus of this chapter. Organic semiconductor device applications have certain requirements of the active layer films that need to be met in order to ensure high performance. For example, in OLED display application, each individual color pixel of the pixel triad must have high resolution (with a pixel diameter of ~ 100 - 300 μm), high mobility of charge within each active layer, low roughness of the films to avoid pinholes and current shunting, etc. Usually, for device applications, film crystallinity, roughness, deposit resolution and deposition rate play important roles in determining the film quality. In the sections below, dependence of the film quality on individual processing parameter is discussed in detail.

2.2. Nozzle geometry

The nozzle geometry is the primary parameter that influences the deposit profile and film quality. Shtein et al., [1] McGraw et al., [2] and Arnold et al. [3] have reported the influence of OVJP nozzle geometry on the deposit shape and profile. GF-OVJP has two coaxial concentric nozzles influencing the jet fluid dynamics and deposit profile. Depending on the application and film requirements, the nozzle geometry can be chosen.

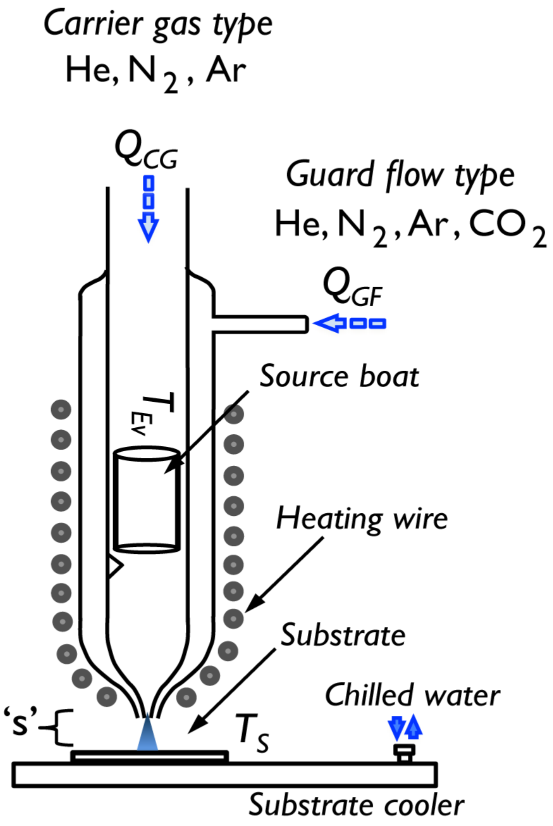

Figure 2-1. GF-OVJP nozzle schematic with the independently controllable parameters that influence the deposit profile and film quality.

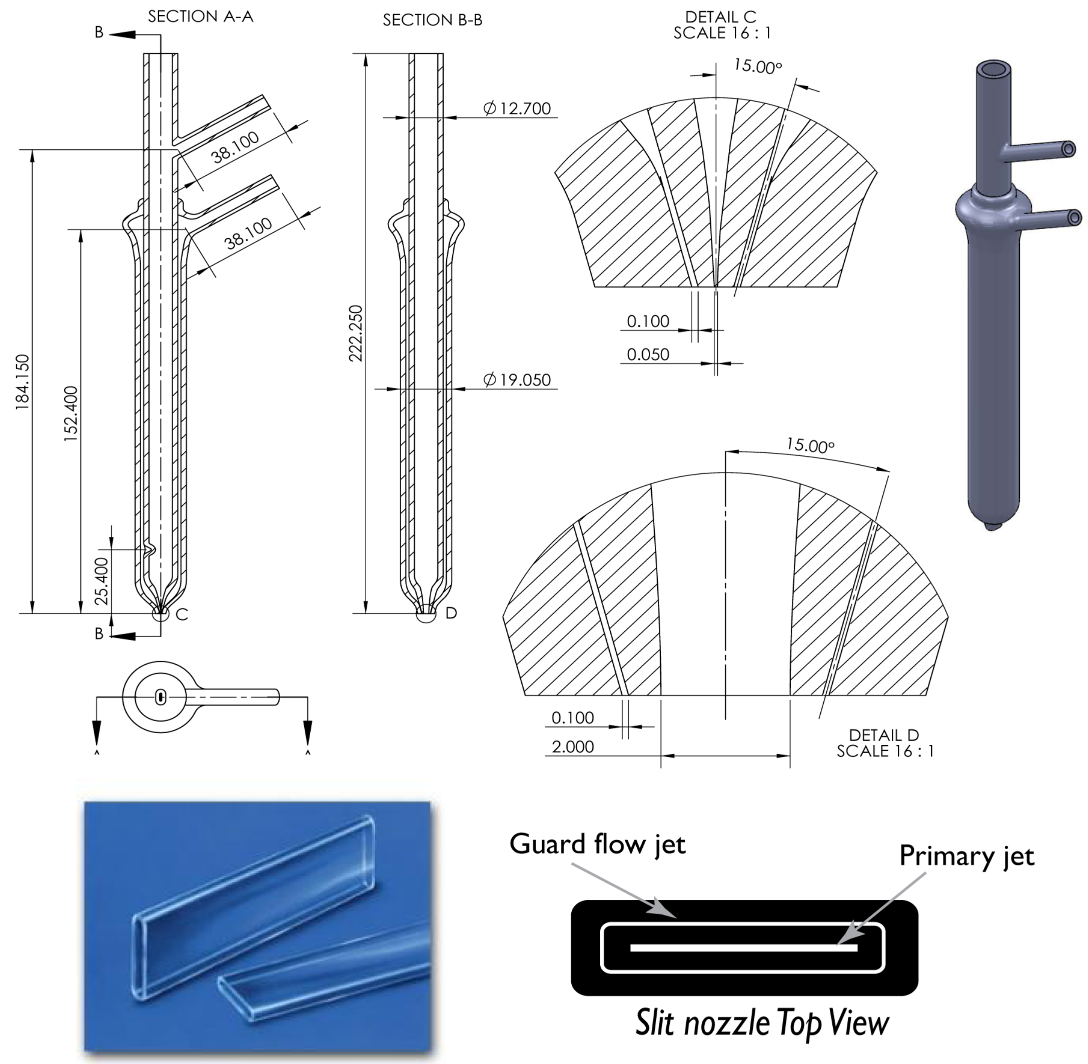

Figure 2-2. Slit nozzle geometry with a 50 μm x 2 mm opening for the *CG* jet, surrounded by a 100 μm *GF* opening shown here in the CAD drawing and the nozzle exit cross-section schematic at the bottom right. Bottom left shows the glass slit capillaries commercially available (VitroCom) to fabricate such a nozzle.

GF-OVJP nozzles can be made from quartz glass or metal. Since glass is easier to mold and fuse, all the work in this thesis has be done with Quartz glass nozzles. First, the shape of the nozzle needs to be determined depending on the application. For example, OLEDs often need to be patterned and a circular nozzle geometry can be used to deposit circular organic patterns or pixels. On the other hand, OPVs usually require large area organic deposits which need large, planar area film coverage at high deposition rates. For this application, a rectangular slit nozzle can be designed and translated perpendicular to the slit length to deposit large area films of uniform thickness over a planar substrate. **Figure 2.2** shows the CAD drawing, cross-section schematic and commercially available glass capillaries that can be used to make these slit nozzles. The slit nozzle's *CG* jet cross-section aspect ratio should be >20 to ensure film thickness uniformity along the length of the deposit, and negligible edge effects.

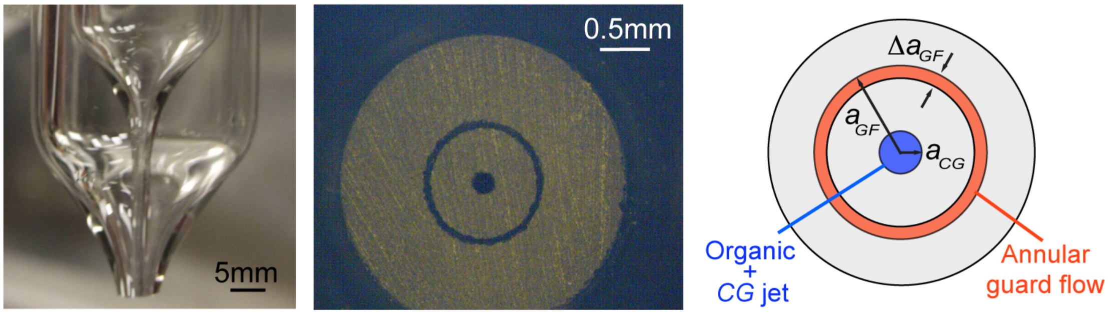

Figure 2-3. GF-OVJP circular nozzle side view and cross-section images with the geometry parameters labeled. [4]

The work in this thesis has been done with circular cross-section nozzles. Two glass tubes placed one inside the other, with outer diameters ½" and ¾", with the latter being shorter than the former, are aligned coaxially and fused at the back end. The front ends are pulled together, cooled and ground along the nozzle axis to form the nozzle exit of the required dimensions. a_{CG} and a_{GF} are the radii of the inner and out nozzles, respectively.

Depending on the inner nozzle wall thickness after pulling and grinding the nozzles Δa_{GF} is the *GF* nozzle opening, as shown in **Fig. 2-3**. The angle of the outer wall of the inner tube with respect to the axis of the tubes determines the angle of the guard flow jet (α). The main design factor to consider when choosing a_{CG} is the dimension of pixel size required for the application. The ratio of pixel diameter of an OLED to the recommended nozzle diameter (pixel diameter/$2a_{CG}$) ranges from 1.3 to 2, depending on the nozzle-substrate separation distance, discussed in the next section. After fixing the value of a_{CG}, a_{GF} has to be set to be approximately three to six times of a_{CG}. From simulation it was found that when $a_{GF}/a_{CG} < 2$ the primary jet experiences turbulence before reaching the substrate, while for $a_{GF}/a_{CG} > 7$ air is trapped in the pocket between the *CG* and *GF* jets. The velocity magnitude of the *CG* and *GF* jet up on exiting the nozzle is determined by ratio of the mass flow rates, Q_{CG} and Q_{GF}, to the product of the molar mass of the gas and the nozzle exit area. So, the exit velocities are given by $v_{CG} = Q_{CG}/(M_{CG} \bullet \pi \bullet a_{CG}^2)$ and $v_{GF} = Q_{GF} \Big/ M_{GF} \cdot \pi \cdot \left((a_{GF}^{outer})^2 - (a_{GF}^{inner})^2 \right)$, where $\Delta a_{GF} = (a_{GF}^{outer} - a_{GF}^{inner})$. In order to have a high velocity laminar jet the nozzle exit velocities should be ~ 200 m/s. Thus, Δa_{GF} can be set in order to attain these *GF* exit velocities for a chosen range of Q_{GF}. The only way to achieve laminar jet flow ($Re < 4 \times 10^5$) after the exit of the nozzle is to have the nozzle exit aspect ratio, i.e. length of the nozzle/$2a_{CG} > 10$. These are all the considerations to keep in mind when designing the nozzle before glass blowing.

2.3. Nozzle-substrate separation distance

The nozzle-substrate separation distance '*s*' is an important parameter which influences the behavior of the jets before reaching the substrate and therefore impacts the resolution of the deposited pixel, the degree of penetration of air molecules inside the organic jet stream and deposition rate. The light blue lines in **Fig. 2-4** schematic shows the hypothetical lines of the *CG* and *GF* jets. When the substrate is placed close to or beyond

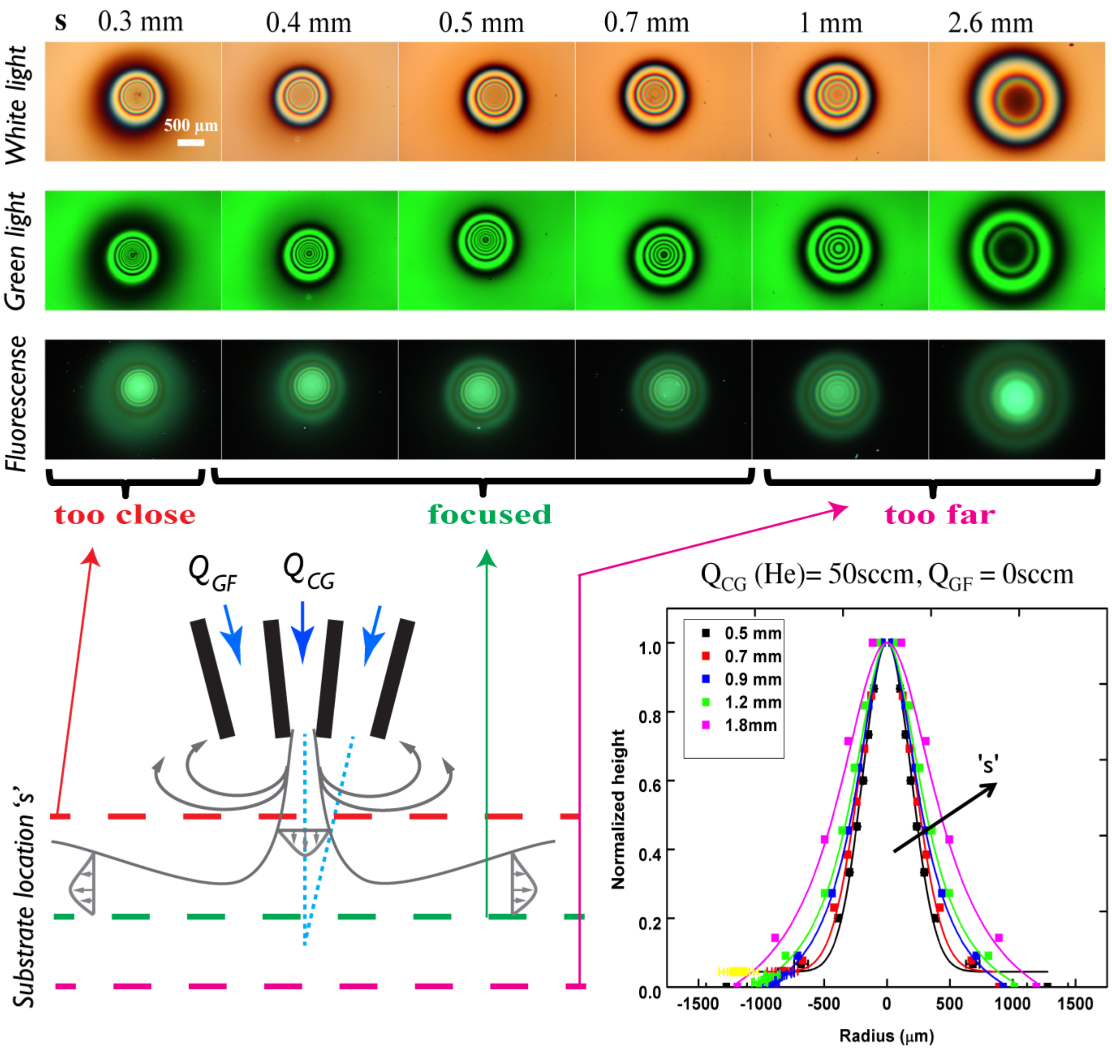

Figure 2-4. Effect of nozzle-substrate separation distance on deposit profile. There is a 's' sweet spot to get focused deposits at optimal deposition rates. When the substrate is placed too close or too far from the nozzle, turbulence is introduced in the organic + carrier gas jet, causing disruption in the deposited profile. [5]

the intersection point, the jet streams undergo turbulent mixing [6] which results in broadening of the pixel and loss of shielding of the organic vapor laden carrier gas jet from the ambient air. When '*s*' is too small, i.e. the substrate is too close to the nozzle, the stagnation zone created due to *CG* jet impingement on the substrate is too large, causing the jets to disperse and thus broadening the pixel and roughening the film. The optimized value verified through simulation and experiments for the GF-OVJP tool is s/a_{CG} = 2 – 4, for an α of 15°.

2.4. Carrier gas and guard flow gas type

The inert carrier gas and guard flow jets have different functions in the GF-OVJP system. The carrier gas flows in to the inner tube, picks up the sublimated small molecular organic vapor, forms a jet at the CG nozzle exit and impinges onto the substrate. The heavier organic molecules have a higher momentum than the lighter *CG* molecules in the jet, and are more collimated, as shown in **Figure 2-5**.

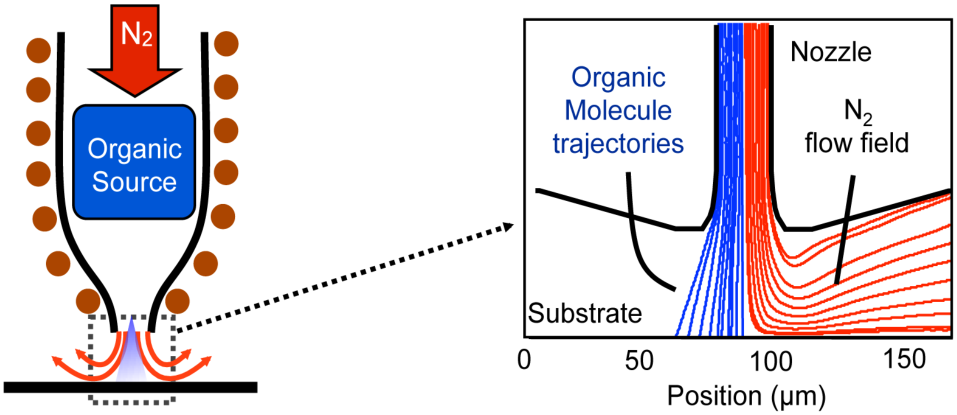

Figure 2-5. Trajectory of organic and carrier gas molecules in the *CG* jet. [1]

The molar mass and size of the carrier gas molecules play an important role in establishing the film quality. Sublimated organic moles have a higher diffusivity, $D_{O\,CG}$ (given by Chapman Enskog equation, **Eq. 2.1**) in lighter carrier gas like Helium than a heavier *CG*, like Argon.

$$D_{O\cdot CG} = \frac{2}{3}\sqrt{\frac{k_B^3 \cdot N_A}{\pi^3}} \cdot \frac{\sqrt{T^3 \cdot \left(1/(2M_O) + 1/(2M_{CG})\right)}}{P \cdot \Omega_{O\cdot CG} \cdot \left(\frac{\sigma_O + \sigma_{CG}}{2}\right)} \qquad (2.1)$$

where k_B and N_A are the Boltzmann constant and Avogadro number, T (K) is the evaporation zone temperature, P (bar) is the pressure, M (g/mol) is the molar mass, σ (Å) is the collision diameter of each species and Ω is the collision integral (close to 1). *O* and *CG* are the organic and carrier gas species, respectively. When M_{CG} and σ_{CG} are smaller, more organic material would be accommodated in the *CG* stream in the evaporation zone of the inner tube. For the GF-OVJP system, for most small molecular semiconductor materials, $D_{O\,CG}$ for He is 3 times higher than Ar as *CG*, and 1.5 times for N_2.

M_O/M_{CG} also determines the pattern dispersion due to horizontal momentum transfer to the organic molecules from collisions with the diverging carrier gas. For example, when He is chosen as the *CG*, less momentum is transferred to the organic molecules at the substrate and hence the organics have a more collimated trajectory, increasing the pattern resolution. This is shown in **Figure 2-6**. On the other hand, M_{GF}/M_{CG} determines the effectiveness of the guard flow to restrict pattern dispersion and shield the *CG* jet laden with hot organic vapor from the ambient oxygen and moisture. When the M_{GF}/M_{CG} is high, for a choice of Ar or CO_2 as the guard flow gas and He or N_2 for the *CG*, and the *CG* and *GF* jets having similar velocities, the *GF* gas molecules have higher momentum and can confine the *CG* jet better, making the deposits more collimated, while keeping the ambient air molecules out of the deposition zone.

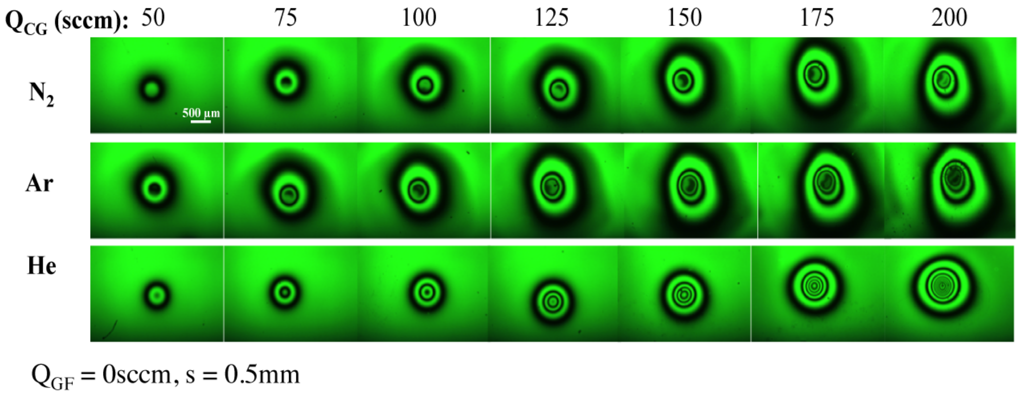

Figure 2-6. Pattern dispersion depends on the choice of carrier gas. [5]

In this thesis, N_2 is used as both the carrier gas and guard flow to isolate the thermal and flow effects of *GF* on the deposited films, without introducing additional variables. However, it is recommended that He be used as the *CG* and Ar be used as *GF* for future work with GF-OVJP.

2.5. Carrier gas and guard flow mass flow rates

The flow rates of *CG* and *GF* jets have a direct impact on the film quality and deposition rate and are controlled by mass flow controllers (MFCs). The kinetic energy of the organic molecules right above the substrate, along with the thermal energy, determines the crystallinity fo the deposited films. The admolecules, upon reaching the substrate, can diffuse in the film to find the lowest energy state. When the kinetic energy is high the films are usually crystalline. The kinetic energy of the organic admolecules is proportional to v_{CG}^2. And v_{CG}, in turn, is given by $Q_{CG}/(M_{CG}\bullet\pi\bullet a_{CG}^2)$. The activation energy required for crystallization of the film (or crystallization energy) has a square dependence on Q_{CG} enabling the GF-OVJP user some degree of control of the film morphology using this independently controllable parameter. Note that the lower bound of Q_{CG} is fixed by minimum velocity of the organic molecules to collimate and reach the substrate for deposition. As shown in **Fig. 2-6**, Q_{CG} also influences the pattern resolution.

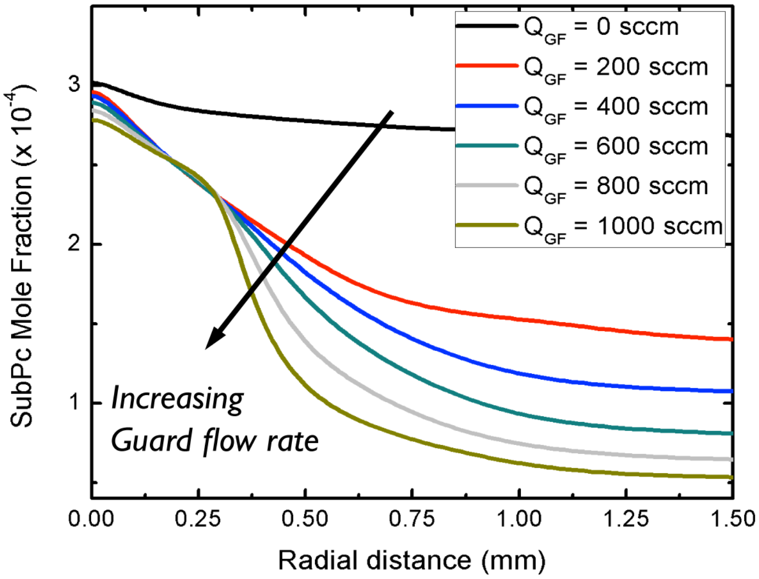

Figure 2-7. Pattern resolution improves with increase in guard flow rate as shown in the organic vapor concentration on the substrate with radial distance from the nozzle axis, while depositing an OPV donor material, SubPc. [7]

The *GF* mass flow rate is to be chosen depending on the sensitivity of the organic species to ambient air. Many organic materials, at elevated temperatures, react with ambient oxygen and moisture. *GF* jet isolates the deposition zone from the ambient, creating a pocket of inert atmosphere around the organic jet during deposition. The organic molecules, once deposited, in the cooled solid film have higher resistance to reaction with air molecules and degradation. So the primary objective of the *GF* is to shield the organic molecules and *CG* jet from air. It is found and reported in **Chapters 3-5**, how Q_{CG} can also be used as an additional handle for controlling the morphology of the deposited films as it imparts both kinetic and thermal energies to the organic molecules *on route* to the substrate. Q_{GF} is also an excellent parameter to improve pattern resolution without the need for any mechanical components. With an appropriate choice of a_{CG}, a_{GF}, Δa_{GF}, and s, increasing confines the *CG* and organic vapor, to change the shape of the deposited profile and improve resolution, an example of which is shown in **Fig. 2-7**. Most of the thesis is a report of the influence of guard flow rate, Q_{GF}, on the flow dynamics, film morphology and the resulting device performance.

2.6. Source temperature

In the GF-OVJP apparatus, the organic material powder, commercially purchased, is sandwiched in quartz wool and placed in a source boat, as shown in **Figure 2-1** (a kink is provided in the inner tube to fix the location of the source boat relative to the nozzle), and heated above the sublimation temperature of the organic material, to a temperature T_{Ev}. A thermocouple is positioned inside the source boat which provides the input to a digital PID temperature controller, which in turn controls the current across the heating tape that wraps the nozzle, in order to maintain a fixed T_{Ev} temperature. The temperature profile along the axis of the nozzle is measured (example shown in **Figure 2-8**) to ensure that the vapor pressure at the source at these temperatures is enough for high evaporation rates of the material. As observed from **Fig. 2-8**, the temperature along the nozzle axis drops below the sublimation temperature (dashed line) right before the nozzle exit. This is because the thermal insulation covering the nozzle is not effective near the narrow section of the nozzle exit. This, however, is beneficial, since the *CG* jet temperature after exiting the nozzle and on the substrate should be below 50°C for complete condensation of the organic vapor immediately up on striking the substrate (depending on sticking coefficient of the organic on the substrate).

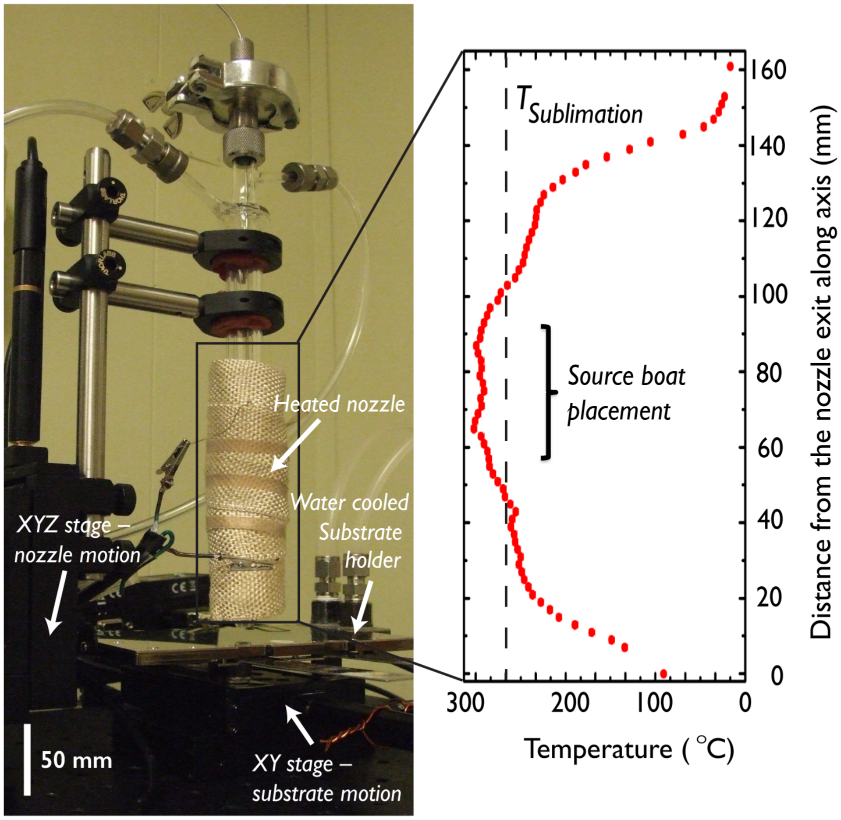

Figure 2-8. Temperature profile along the axis of the nozzle, indicating the evaporation zone in which the source boat is placed.

The source material evaporation rate has an Arrhenius relationship with T_{Ev}. Hence, the amount of material sublimated into the carrier gas stream, in the evaporation zone, increases exponentially with T_{Ev}, but only up to a point. In the 'diffusion-limited' regime, as T_{Ev} is increased the *CG* flow can accommodate and carry all the organic molecules up to the point, where the carrier gas is saturated with sublimated organic vapor and cannot carry any more, irrespective of further increases in T_{Ev}. The latter is the GF-OVJP 'kinetic-limited' regime. These regimes have been further discussed in **Chapter 6**. The upper limit of T_{Ev} is the temperature at which the material undergoes chemical decomposition. T_{Ev} can also affect the morphology of the deposited film. As the source temperature is increase the *CG* and *GF* jet stream also have higher temperatures, since the heating tape wraps around the whole nozzle and the temperature is maintained only by one thermocouple in the source boat. Increase in T_{Ev} results in higher thermal energy of the organic molecules impinging on the substrate, and therefore, affect both the crystallinity and the roughness of the films deposited. GF-OVJP is capable of producing unique morphologies due to this capability of a top-down annealing process during deposition.

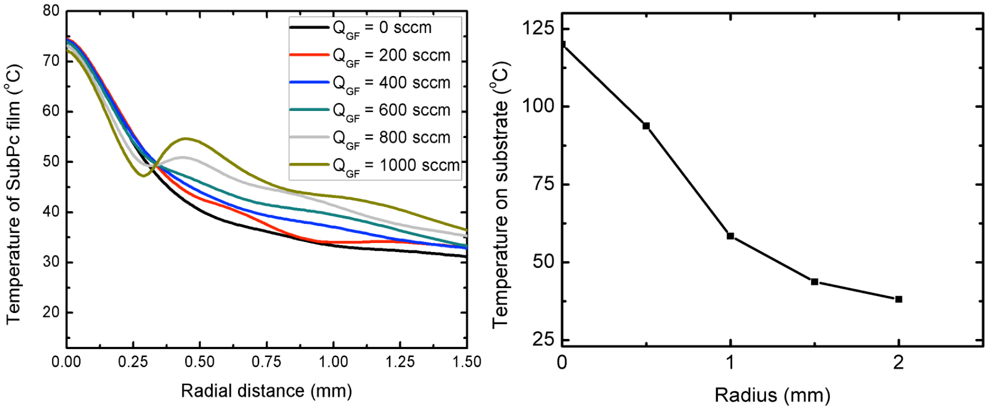

Figure 2-9. Simulated and measured temperatures on the surface of the substrate show a drastic drop in film temperature in the radial direction from the nozzle axis.

Another unique feature of GF-OVJP is that it enables self-purification of the organic materials. Since the source material is heated and held at a specific evaporation temperature, the low temperature impurities in the material are blown out at the very beginning. Then only the desired organic material can be deposited for long periods leaving behind the high temperature impurities in the source boat. In the work in this thesis, T_{Ev} is always maintained at approximately 20°C above the sublimation temperature of the organic material.

2.7. Substrate temperature

GF-OVJP enables deposition of organic materials at any substrate temperature, T_S, below 50°C. However, the film properties like roughness and crystallinity are much improved at low T_S. The substrate is placed on a water chilled substrate holder and can be taken down to ~ 8°C, or the dew point of the room, before there is moisture condensation on the substrate. But, as reported in this thesis, the quality of the films deposited in air at higher substrate temperatures by GF-OVJP is comparable to VTE deposited films, despite this limitation. The temperature of the jet right below the nozzle axis is high and drops off to near room temperatures in the radial direction from the nozzle axis, as shown in **Figure 2-9**. The temperature of the film measured at a radius of 2 mm from the nozzle axis is below 35°C and hence the material in the solid film is not reactive with the ambient air, in spite of being exposed to it. A more detailed discussion on this topic is available in **Chapter 5**.

A simple heat transport model is presented here to quantify the amount of energy transferred from the *CG* and *GF* jets to the deposited film and the amount of energy stored in the film available for crystallization.

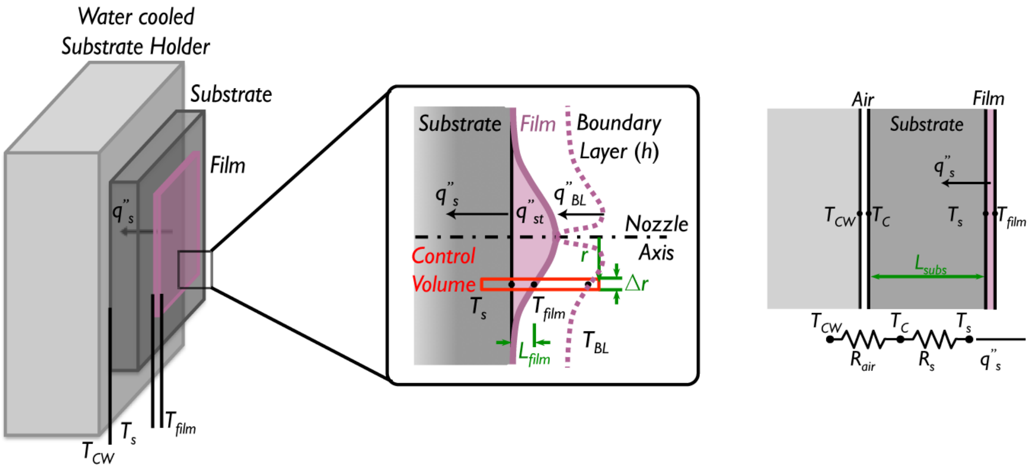

Figure 2-10. Heat transport model of flow of energy from the boundary layer (BL) of the jet, to the film, into the substrate and finally to the water chilled substrate holder.

The temperature of the water cooled substrate holder is held constant, T_{CW}. When the substrate is fixed to the substrate holder, unless heat transfer lubricant like silver paste is used, the bottom surface of the substrate and the top surface of the holder are not in perfect contact. There is always a layer of air trapped with a resistance of R_{air} and the temperature at this point is T_C. Assuming that the thickness of the substrate, L_S and the thermal conductivity, k_S are known, the heat transported from the substrate to the holder is given by **Eq. 2.2** and shown in **Fig. 2.10** (right).

$$q''_S = \frac{T_S - T_{CW}}{R_{air} + L_S / k_S} \tag{2.2}$$

Next, consider the energy flow from right to left of the control volume (at radial distance '***r***' from the nozzle axis) shown in **Fig. 2-10** (middle). The heat transport is given by $q''_{in} - q''_{out} = q''_{st}$, where q''_{st} is the heat stored in the organic film. Assuming the convective heat transfer coefficient, *h*, in the boundary layer (BL) is known and q''_{out} is the equal to q''_S calculated from **Eq. 2.2**, the instantaneous heat stored in the film is given by

$$\mathrm{q}''_{st} = h(T_{BL} - T_{film}) - \frac{\mathrm{T_S - T_{CW}}}{\mathrm{R_{air} + L_S / k_S}} \tag{2.3}$$

where T_{film} and T_{BL} are the temperatures on to of the film and *BL* respectively. If the film deposition rate, r^{r}_{dep} (nm/s) is known at each ***r***, then $dt = r^{r}_{dep}.dz$ where *z* is the direction along the nozzle axis. From the second degree heat equation, the following differential equation is obtained relating the temperature inside the film to its properties.

$$\frac{dT}{dt} = r^{r}_{dep}\frac{dT}{dz} = \frac{k_{film}}{\rho C_P}\frac{d^2T}{dz^2} + \frac{\partial \dot{\mathrm{q}}''_{st}}{\rho C_P} \tag{2.4}$$

where $\int \partial \dot{\mathrm{q}}''_{st} = \mathrm{q}''_{st}$. Integrating Eq. 2.4 across the length of the film, L_{film}, the temperature at the top of the film can be obtained as

$$T_{film} = \mathrm{T_S}\left(\frac{L_S - a}{L_S} - \frac{a}{L_S}e^{-L_{film}/a}\right) + \frac{aT_{CW}}{L_S}\left(e^{-L_{film}/a} - 1\right) + \frac{a\mathrm{q}''_{st}}{k_{film}}\left(a + L_{film}\right) \tag{2.5}$$

where $a = \frac{k_{film}}{r^{r}_{dep}\rho C_P}$. From **Eq. 2.3** and **2.5**, by equating T_{film}, the energy stored in the film at '***r***' from the nozzle axis at any moment during deposition can be evaluated, giving the expression in **Equation 2.6**.

$$\mathrm{q}''_{st} \cdot A = T_{BL} + \mathrm{T_S}\left(1 - B\right) + T_{CW} \cdot B \tag{2.6}$$

where $A = h^{-1} - \frac{a}{k_{film}}\left(a + L_{film}\right)$ and $B = \frac{a}{L_S}\left(e^{-L_{film}/a} - 1\right) - \frac{h^{-1}}{R_{air} + L_S / k_S}$. If the energy of crystallization of the organic film is known, the GF-OVJP system can be designed to enhance the crystallinity of the film by maintaining ($q_{st} - \Delta H_{Condensation}$) above this crystallization energy, where $q_{st} = \oint_{FilmArea} q''_{st}$.

2.8. Substrate/Nozzle translation speed

The GF-OVJP nozzle and substrate holder are both mounted on XYZ translation stages and can be used to draw any predefined pattern. Only one of them is moved relative to the other for pattern deposition. Z translation stage is used to set a particular nozzle-substrate separation distance. The relative X and Y translation rates are given by v_X and v_Y. For a given set of process parameters and deposition conditions, the flux of organic molecules in the jet is fixed. The translation velocity then determines the deposition or growth rate. The translation rate to be used to get a required film thickness is decided based on the thickness - translation calibration that is done prior to the start of other experiments. For large area deposits of a particular thickness '*t*', the substrate is translated in a dithered pattern [1] to deposit closely spaced line deposits and a particular translation speed v_X. The thickness – translation relationship is then calibrated from $t \bullet v_X = C$, where *C* is the calibration constant. More details are provided in **Appendix A** and **Ch. 5**.

2.9. References

[1] M. Shtein, P. Peumans, J. B. Benziger, and S. R. Forrest, "Direct mask-free patterning of molecular organic semiconductors using organic vapor jet printing", *J. Appl. Phys.*, **2004**, *96*, 4500.

[2] G. J. McGraw, S. R. Forrest, "Fluid dynamics and mass transport in organic vapor jet printing," *J. Appl. Phys.*, **2012**, *111*, 043501.

[3] M. S. Arnold, G. J. McGraw, S. R. Forrest, and R. R. Lunt, "Direct vapor jet printing of three color segment organic light emitting devices for white light illumination," *Appl. Phys. Lett.*, **2008**, *92*, 053301.

[4] S. Biswas, K. P. Pipe, M. Shtein, "Solvent-free, direct printing of organic semiconductors in atmosphere", *Appl. Phys. Lett.* **2010**, *96*, 263301

[5] O. Shalev, S. Biswas, D. Hinz, M. Shtein, "Influence of carrier gas and guard flow gas properties on patterning resolution of molecular semiconductor films deposited by GF-OVJP", **2014**, (*in preparation*).

[6] E. Bitziou, N. C. Rudd, M. A. Edwards, and P. R. Unwin, "Visualization and Modeling of the Hydrodynamics of an Impinging Microjet", *Anal. Chem.*, **2006**, 78, 1435.

[7] S. Biswas, K. A. Luck, M. Shtein, "Guard flow-enhanced organic vapor jet printing of photovoltaic donor materials in air", *Org. Electron.* **2012**, *13*, 2905.

CHAPTER 3

Fabrication of OLEDs by GF-OVJP

3.1. Requirements for OLED active materials deposition

OLEDs are a commercial success in the mobile display industry and are making headway in the flexible large area displays and solid-state lighting markets as well, due to their light weight, thin form factor, potential low costs and high power efficiency. In addition, organic materials can be deposited on any kind of substrate, including non-planar and flexible, at relatively low temperatures compared to inorganics. Some examples of commercially available OLED applications are shown in **Figure 3-1**.

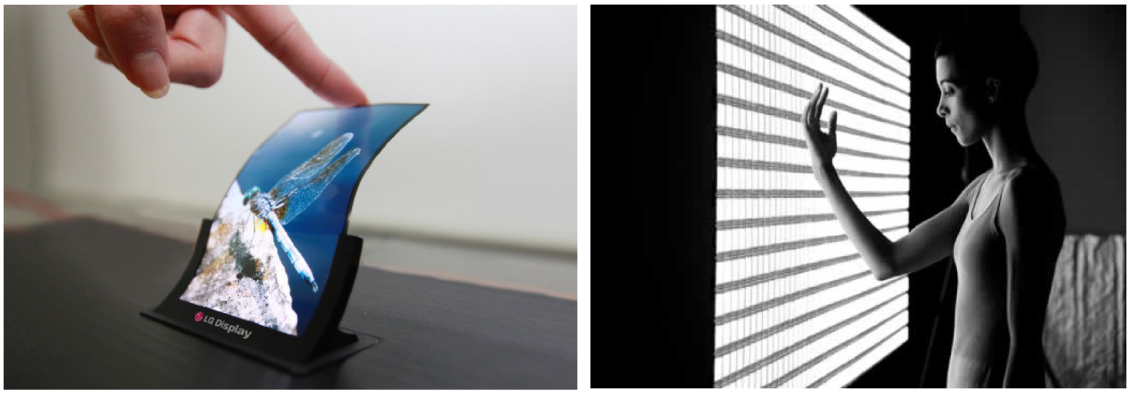

Figure 3-1. Examples of commercially available OLED products. (left) LG's 5-inch OLED panel created for mobile devices, constructed of plastic, making it both flexible and unbreakable. (right) The Philips Lumiblade large area OLED lighting panel for interactive illumination. (Images from inhabitat.com)

The fabrication of next generation organic optoelectronic devices, e.g. displays, lighting based on OLEDs, [1-3] often requires both the ability to form well-defined organic multi-layers that maximize charge injection and recombination efficiencies, and the ability to achieve high resolution patterns of the active organic materials. Much research has been devoted to achieving these goals, with considerable challenges recognized for the processing to occur at ambient conditions.

In high performance, small molecular-based OLEDs, the organic layers are most commonly deposited by vacuum thermal evaporation (VTE). [4, 5] More recently, device processing by flash evaporation [6] and OVPD [7-9] have been shown, as described in **Chapter 1**. These methods require moderate to low vacuum conditions, and the use of shadow masks to pattern the organic emissive layers. The latter wastes the majority of the active organic material delivered to the substrate, reducing manufacturing throughput and increasing process complexity and cost. Several techniques have been developed to achieve organic thin-film patterning without shadow masks: laser induced thermal patterning (LITI) [10], contact printing [11], cold welding [12], ink-jet [13, 14], MoJet [15], and OVJP [16 - 18], among others. While conventional ink-jet printing can be carried out in the ambient, it uses a liquid solvent carrier that often leads to residual solvent and impurities in the deposited films, and requires solvent orthogonality to achieve high performance multi-layer device structures [19]. Substantial interest thus persists in developing new techniques for optoelectronic device deposition and patterning in the ambient, in part due to the potential for cost reduction and environmental benefits when compared to conventional vacuum or solvent-based processing. The demonstration a working OLED with its emissive layer deposited in air by GF-OVJP is the highlight of this chapter, and has been previously reported by Biswas *et al*. (2010) [20].

3.2. GF-OVJP process

Organic vapor jet printing (OVJP) proceeds by evaporation of a crystalline organic powder source material into a hot, inert carrier gas, which is directed through a collimating nozzle at high velocity onto a nearby substrate, as described in **Chapter 1**. A stagnation zone develops above the surface [17], dispersing the jet. For sufficiently large pressure drops and long nozzles, however, the relatively heavier organic molecules are accelerated to the velocity of the carrier jet, attaining greater momentum than the carrier gas molecules. As a result, the organic molecules penetrate the stagnation zone and adsorb on the substrate in well defined patterns, [16] in contrast to transport by purely diffusive processes.[5] A schematic of the process is shown in **Fig. 3-2**.

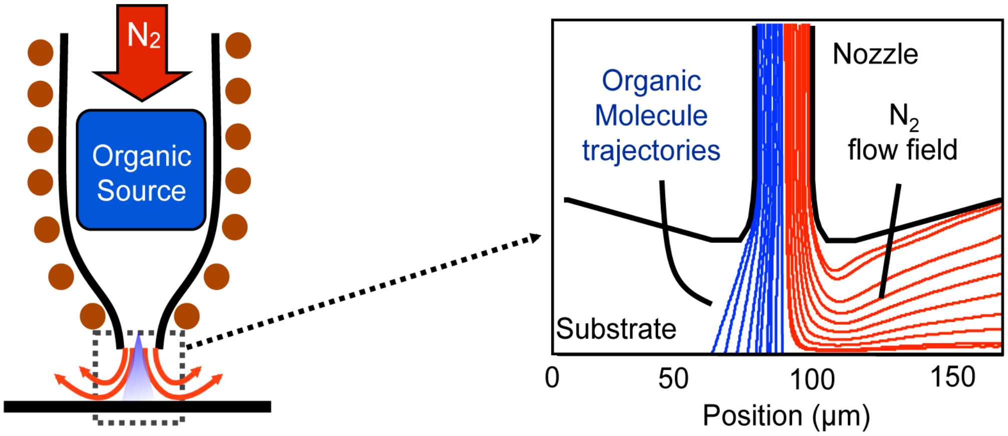

Figure 3-2. Illustration of the working principle of OVJP: Organic material and an inert carrier gas vapor is jetted out of a microscopic nozzle onto a cooled substrate. The heavier organic molecules, having more momentum, are collimated and condense upon contact with the substrate. The lighter carrier gas flows away. [16]

Pattern resolution as high as 1000 dots per inch has been shown while depositing at reduced pressures, [21] high local deposition rates have been achieved, [16] and device efficiency approaching vacuum thermally-deposited devices has been demonstrated. [17,18] However, when the downstream pressure, P_L, is increased to atmospheric levels, pattern resolution suffers. Due to the circular geometry of the nozzle and the flow fields of the organic-carrier gas vapor jet, the deposited pixel is always domed. Resolution of the deposited pixel is defined as FWHM/Base ratio, or from the 'useful volume ratio', as shown in **Fig. 3-3**.

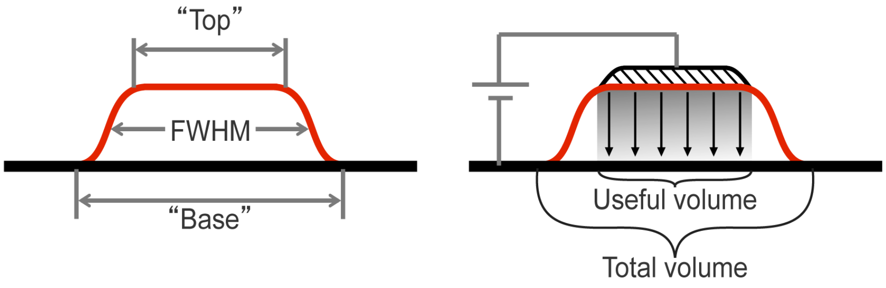

Figure 3-3. Metrics of deposited pixel resolution is defined as the ratio of the full width at half the maximum height (FWHM) to width at the 'base' of the deposit cross-section (left). Alternatively, for OLED applications, resolution could be defined as the Useful volume ratio, where the 'useful volume' is the volume of material over which an electrode can be evaporated with minimal current shunting (right).

As P_L is increased in the OVJP chamber, the deposited pixel broadens, as shown in **Fig. 3-4**. The pixel broadening causes a 'domed' cross-section profile, and can lead to current shunting in OLEDs fabricated using such deposits, resulting in decrease device efficiency. Furthermore, when carrying out this process in ambient air, the hot organic vapor can come in contact with the surrounding oxygen and moisture en route to the substrate. Because the highly conjugated organic semiconductor compounds are susceptible to oxidative damage at elevated temperatures, their device-relevant properties (e.g. luminescence efficiency) usually degrade in air. [22, 23]

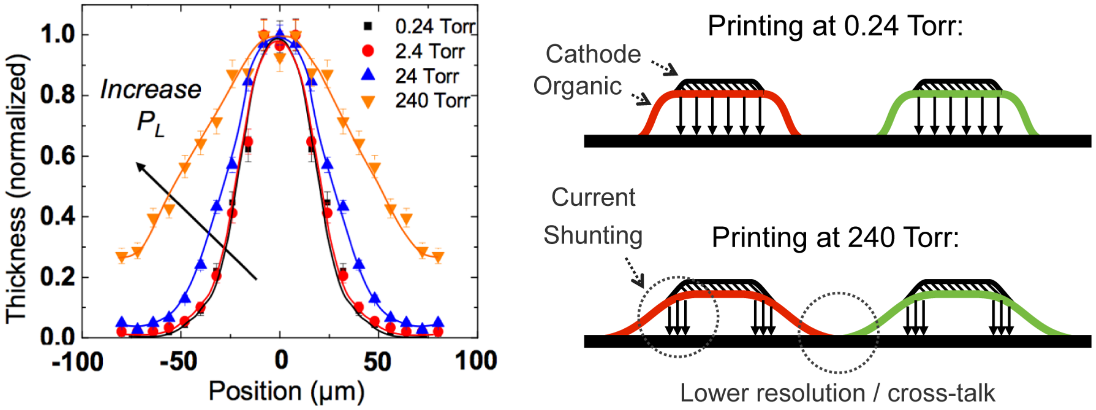

Figure 3-4. Pixel broadening from increase in OVJP downstream chamber pressure results in loss of resolution, OLED current shunting, and potential pixel color cross-talk, which are detrimental to the performance of the devices. [16]

Hence, a secondary 'guard' jet is introduced to coaxially surrounds the primary jet of hot organic – carrier gas vapor mixture. The guard jet hydro-dynamically focuses the primary jet, thereby improving the pixel resolution even at atmospheric pressure, and shields the organic vapor from the air, preventing oxidative degradation of the sensitive semiconductor materials. The external quantum efficiency of OLEDs with the emissive layer jet-printed in air by GF-OVJP scales with guard flow rate, attaining parity with devices deposited entirely in vacuum by both OVJP and VTE processes.

3.3. Green OLED active materials deposition

The guard flow-enhanced vapor jet printing concept is validated using experiments and simulations. The experimental apparatus [**Fig. 3-5**] consisted of a 220 μm diameter inner nozzle with a 240 μm thick wall, surrounded by a coaxial nozzle with an annular gap of 100 μm. The annular channel was angled at 15° from the nozzle axis. A 0.5” glass tube pulled to form a nozzle tip of 220 μm internal diameter was fused to a concentric glass tube of 0.75” outer diameter with a nozzle tip of 450 μm internal diameter to make the GF-OVJP nozzle. The nozzle was cleaned with acetone and 2-propanol, dried and wrapped with 24-gauge nickel-chrome resistance wire (Omega Engineering, Inc.) with a total resistance of 11 Ω. The heating coil was connected to a temperature controller (Digi-Sense Benchtop temperature controller, Cole-Palmer Instruments Co.) and a 1/8” K-type thermocouple was used to maintain the temperature of the source.

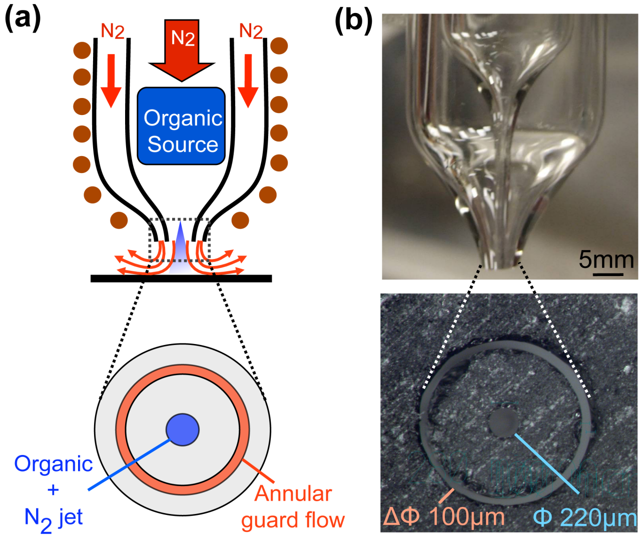

Figure 3-5. Schematic and photograph of nozzle used in GF-OVJP OLED experiments. [20]

Tris-(8-hydroxyquinoline) aluminum (Alq_3), an archetypal electron transporting material that is sensitive to oxygen and moisture exposure, was used in patterning and device deposition experiments. The source consisted of 0.18g of Alq_3 sandwiched between quartz wool and placed in the heated source section of the inner tube. Crystalline Alq_3 powder was heated to 280°C at 1.15 bar pressure (P_0), while the nozzle wall was maintained at 300°C downstream of the source to prevent parasitic vapor condensation. Mass flow controllers (FR500, Key Instruments) were connected to the inner and outer nozzles to vary the flow from 0.1 to 500 sccm. Glass and silicon 2.5 x 2.5 cm^2 substrates were mounted on a computer-controlled X-Y positioning stage (T25-XY motorized translation stage, Thorlabs) and aligned perpendicular to the nozzle axis for patterning. Substrate temperature was controlled via a Peltier cooler between the substrate and stage. The cooler was connected to a power meter, and a thermocouple was placed on the cooler surface 25 mm from the substrate center to measure the cooler's surface temperature. The nozzle-substrate separation (s) was fixed at 0.7 mm, while the substrate was mounted on a Peltier cooler to maintain its temperature below 40°C in the ambient.

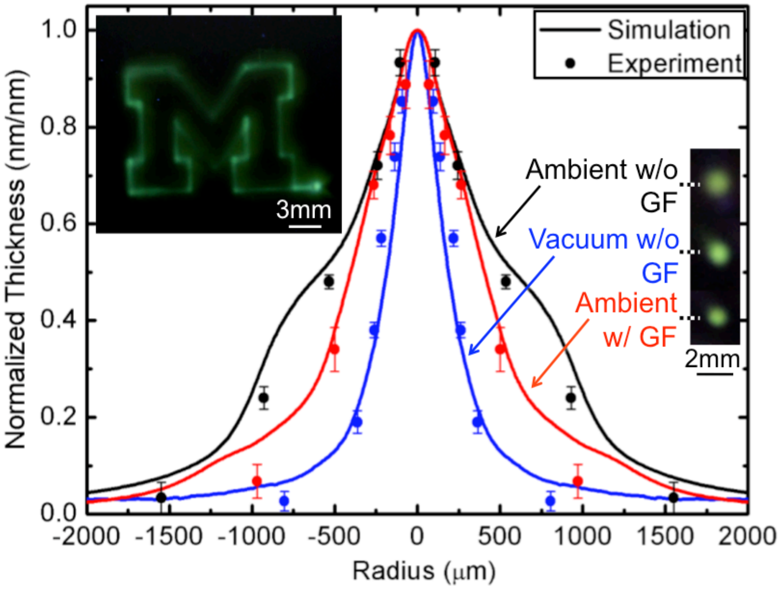

Figure 3-6. Patterns realized by GF-OVJP at 48.6 nm/s local deposition rate, under UV illumination. Cross-section profiles show the effectiveness of guard flow to collimate the deposited pixel.

Because the mole fraction of organic molecules entrained in the jet was less than 10^{-3} in all of the experiments, the thermal conductivity (κ) and viscosity (μ) for both the primary and guard jet could be well approximated by those of the carrier gas. A constant carrier gas flow rate (Q_{CG}) of 100 sccm was used for the main jet, while the guard jet mass flow rate (Q_{GF}) was varied from 0 sccm to 400 sccm. Several representative, experimentally deposited Alq_3 patterns were photographed under ultraviolet illumination [**Fig. 3-6**].

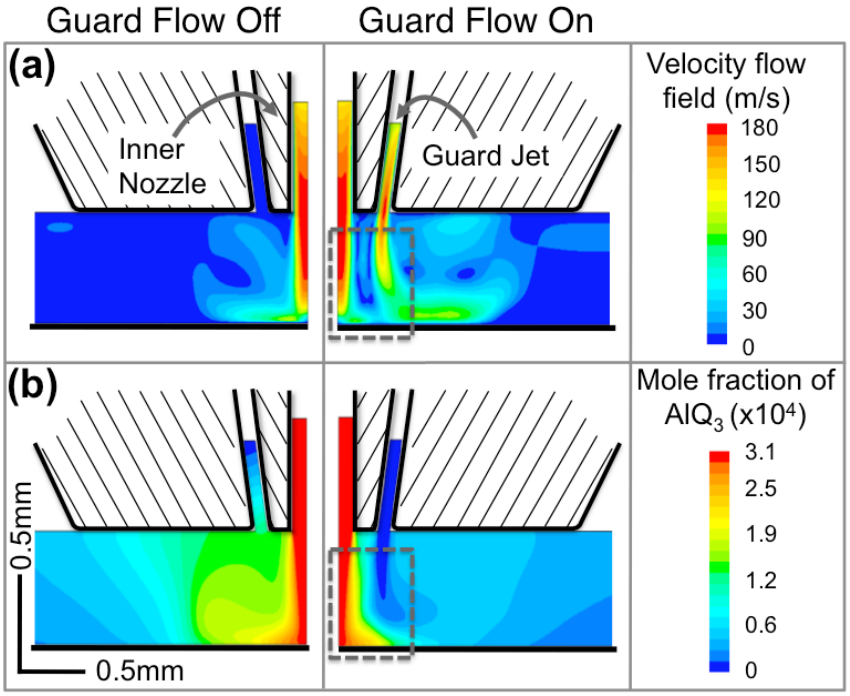

Figure 3-7. Simulated velocity and concentration contours for *GF* off and on scenarios showing shielding and hydrodynamic focusing of the primary jet from the ambient by the guard jet, respectively. [20]

For the experimental parameters described above, the molecular mean free path is substantially smaller than the critical apparatus dimensions, and gas transport takes place in the continuum flow regime ($Kn = \lambda/s$ <<1, where λ is the mean free path of the species, s is the nozzle substrate spacing). Consequently, full hydrodynamic modeling can be used to better interpret experimental results and further inform apparatus design. Using the *k-ε* turbulence model in FLUENT 6.3.26, multi-component diffusion and species transport describing organic vapor diffusion and physisorption [24] were coupled with Navier-Stokes equations to produce a full map of flow velocity, pressure distribution, temperature and species concentration. It is clear from the velocity and species distribution, shown in **Figure 3-7**, that the outer annular jet effectively focuses the inner jet and shields it from interaction with the ambient, strongly suggesting that the degradation of the hot organic vapor contained within the primary jet is suppressed with increasing efficacy for higher outer jet flow rates.

To validate this hypothesis, we fabricated archetypal organic light-emitting devices in which the electron-transporting compound (Alq_3) was deposited by guard flow organic vapor jet printing (GF-OVJP). To isolate the influence of the shielding flow, Alq_3 was jet-printed onto *N,N′*-di-[(1-naphthyl)-*N,N′*-diphenyl]-1,1′-biphenyl)-4,4′-diamine (α-NPD) layers that were pre-deposited onto Indium Tin Oxide (ITO) glass; the substrates were scanned in front of the jet to generate a rectangular, 60 nm thick deposit. Control devices were also made by vacuum depositing 60 nm Alq_3 layers. All samples were then masked and coated simultaneously with lithium fluoride and aluminum (LiF/Al), forming the cathodes. Devices were grown on glass substrates precoated with a 150 nm-thick layer of ITO with a sheet resistance of 20 Ω/sq (Delta Technologies, Ltd.). Substrates were ultrasonically cleaned in detergent solution for ~ 5 minutes, followed by a thorough rinse in deionized water and ultrasonication in heated acetone, trichloroethylene, and isopropanol for 10 minutes each. Substrates were then boiled in isopropanol for 5 minutes, dried in pure nitrogen gas, and exposed to ultraviolet-ozone ambient (Model # 342, Jelight company, Inc.) for 5 minutes immediately prior to film deposition. Approximately 50 nm of α-NPD was deposited using a VTE chamber (Angstrom Engineering Inc.), followed by Alq_3 layer deposition using GF-OVJP in ambient. An array of 0.5 mm and 1 mm diameter cathodes consisting of 0.3 nm of LiF followed by 120 nm of Al were deposited through shadow masks using VTE. The OLEDs were tested in ambient, in the dark, using an Agilent 4156B semiconductor parameter analyzer and a 1931-C Newport power meter. Note that the deposition of the cathode in vacuum through a shadow-mask is a common, convenient laboratory procedure; cathode deposition methods that do not involve VTE have been demonstrated by others. [12, 25, 26]

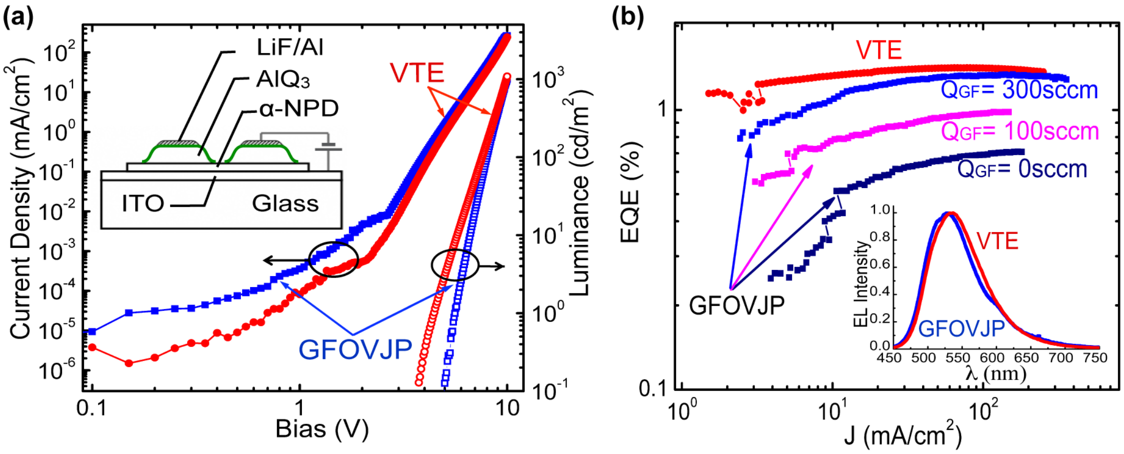

Figure 3-8. Electrical and optical properties of OLEDs with active layer deposited in air by GF-OVJP: (*a*) J-V-L characteristics of vacuum- and GF-OVJP- deposited with (Q_{GF} / Q_{CG} = 3) OLEDs. The GF-OVJP deposited OLED structure is shown in the inset. (*b*) EQE vs current density of vacuum- and GF-OVJP-deposited OLEDs, clearly showing the efficiency of printed devices approaching that of vacuum-deposited devices. (*b*) Inset: EL spectra of the two devices in (*a*). [20]

The resulting device structure (inset in **Figure 3-8 (a)**) and performance characteristics, shown in **Fig. 3-8**, allow comparison of OLEDs printed at 5 different guard flow rates with vacuum-deposited devices having the same structure. The electroluminescence (EL) spectra of both GF-OVJP (Q_{GF} = 300 sccm) and VTE devices peak at λ ~ 530 nm, with a full width at half-maximum (FWHM) height of Δλ ~ 80 nm, consistent with expectations for Alq_3 emission. Jet-printed devices exhibit slightly higher leakage current than VTE devices, due to higher surface roughness of the Alq3 layer deposited in ambient. The RMS roughness of the thermally evaporated Alq3 layer is 2.25 nm, while it increases for the GF-OVJP deposited layer from 2.03 nm to 3.07 nm as the guard flow rate is increased from 0 sccm to 300 sccm, in part due to greater graininess of films deposited by OVJP relative to vacuum deposition at similar rates. [16, 21] In addition the peak to valley roughness [27] also increases from 7.4 nm to 16.8 nm atmospheric deposited layers with increase in guard flow, resulting in higher leakage current in the corresponding OLEDs. This comparison is shown in **Figure 3-9**.

The control devices, in which all of the organic and metal layers were deposited by vacuum thermal evaporation, have an external quantum efficiency (EQE) of 1.36 ± 0.1 % in the trapped charge-limited regime (at 100 mA/cm^2). [28] **Figure 3-10** plots the EQE at 100 mA/cm^2 of devices jet-printed in atmosphere, showing an increase with guard flow rate. For a guard jet flow rate of 300 ± 2 sccm, EQE = 1.32 ± 0.1 %.

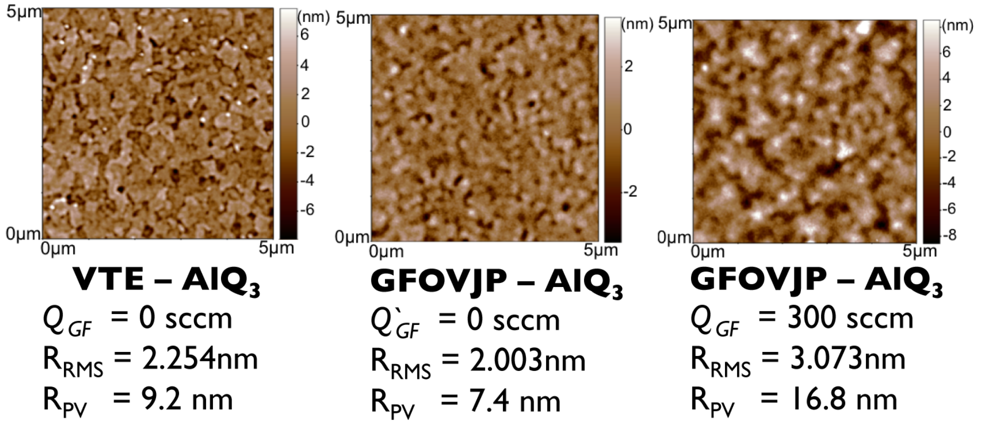

Figure 3-9. AFM images of vacuum- and GF-OVJP-deposited Alq3 layers are included below with their RMS and peak to valley roughness.

A slight drop in EQE is observed when the Q_{GF}/Q_{CG} ratio is raised to 4, possibly due to the doming of the deposit leading to current shunting through the thinner section of the deposit. The ability to attain EQE values comparable to those of vacuum-deposited films by increasing the guard jet flow rate suggests that the guard flow effectively shields the oxygen-sensitive organic vapor, enabling the deposition of high quality films in atmosphere. The inset in **Figure 3-10** shows a green OLED with active layer deposited in air with $Q_{GF}/Q_{CG} = 3$.

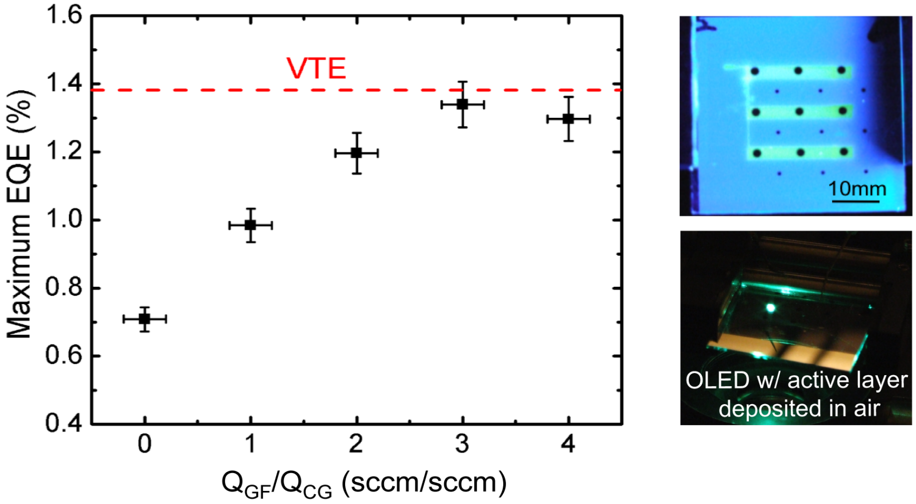

Figure 3-10. Effects of guard flow rate on OLED device performance: EQE at 100 mA/cm^2 vs ratio of guard flow to primary jet flow rates, clearly showing the beneficial effects of the guard jet. Photographs of air deposited OLED using GF-OVJP; strips of Alq$_3$ patterned by rastering the substrate under the nozzle, illuminated by UV light (right top) and biased green OLED lighting up (right bottom). [20]

Note that the device dimensions are mainly limited by the practicality of manual alignment and the size of the shadow mask used to pattern the cathode. Printing resolutions required for display fabrication, for example, have been reported previously using the OVJP technique in vacuum [16] and can likely be achieved by nozzle scaling with the guard flow-enhanced technique.

3.4. Summary

Additive patterning of an archetypal molecular organic electron transporting material (Alq_3) in air using GF-OVJP is successfully demonstrated to create an OLED, the EQE and luminescent efficiency of which are comparable to a device with all layers deposited in VTE. This was achieved by using a highly collimated primary jet of carrier gas to transport the organic vapor to the substrate and a secondary gas jet to shield the organic vapor from degradation. The combination of patterning capability and the ability to deposit device quality films in the ambient environment suggests cost-effective, highly scalable application to the fabrication of OLED-based displays, solid state lighting, and a variety of other organic optoelectronic devices.

3.5. References

[1] C. W. Tang, and S. A. VanSlyke, “Organic electroluminescent diodes”, *Appl. Phys. Lett.* **1987**, *51*, 913.

[2] H. Y. Chen, W. Y. Lam, J. D. Luo, Y. L. Ho, B. Z. Tang, D. B. Zhu, M. Wong, and H. S. Kwok, “Highly efficient organic light-emitting diodes with a silole-based compound”, *Appl. Phys. Lett.*, **2002**, *81*, 574.

[3] M. A. Baldo, S. Lemansky, P. E. Burrows, M. E. Thompson, and S. R. Forrest, “Very high-efficiency green organic light-emitting devices based on electrophos-

phorescence", *Appl. Phys. Lett.*, **1999**, *76*, 4.

[4] S. M. Sze, *Semiconductor Devices: Physics and Technology,* (1st Edition, John Wiley & Sons Inc, New York) **1985**.

[5] M. Shtein, P. Peumans, J. B. Benziger, and S. R. Forrest, "Micropatterning of small molecular weight organic semiconductor thin films using organic vapor phase deposition", *J. Appl. Phys.*, **2003**, *93*, 4005.

[6] C. Cali, V. Daneu, A. Orioli, and S. Riva-Sanseverino, "Flash evaporation of compounds with a pulsed-discharge CO2 laser", *Appl. Optics*, **1976**, *15*, 1327.

[7] M. Baldo, M. Deutsch, P. Burrows, H. Gossenberger, M. Gerstenberg, V. Ban, S. R. Forrest, "Organic vapor phase deposition", *Adv. Mater.*, **1998**, *10*, 1505.

[8] M. Shtein, H. F. Gossenberger, J. B. Benzinger, and S. R. Forrest, "Material transport regimes and mechanisms for growth of molecular organic thin films using low-pressure organic vapor phase deposition", *J. Appl. Phys.*, **2001**, *89*, 1470.

[9] T. X. Zhou, T. Ngo, J. J. Brown, M. Shtein, and S. R. Forrest, "Stable and efficient electrophosphorescent organic light-emitting devices grown by organic vapor phase deposition", *Appl. Phys. Lett.*, **2005**, *86*, 021107.

[10] S. Lamansky, T. R. Hoffend Jr., H. Le, V. Jones, M. B. Wolk, W. A. Tolbert, "Laser induced thermal imaging of vacuum-coated OLED materials", *Proceedings of the SPIE, Organic Light-Emitting Materials and Devices IX*, **2005**, *5937*, 593702.

[11] A. Kumar, H. A. Biebuyck, and G. M. Whitesides, "Patterning Self-Assembled Monolayers: Applications in Materials Science", *Langmuir*, **1994**, *10*, 1498-1511.

[12] C. Kim, P. E. Burrows, and S. R. Forrest, "Micropatterning of organic electronic devices by cold-welding" *Science*, **2000**, *288*, 831.

[13] H. Sirringhaus, T. Kawase, R. H. Friend, T. Shimoda, M. Inbasekaran, W. Wu, E. P. Woo, *Science*, "High-resolution inkjet printing of all-polymer transistor circuits" **2000**, *290*, 2123.

[14] T. R. Hebner, C. Wu, D. Marcy, M. H. Lu, and J. C. Sturm, "Ink-jet printing of doped polymers for organic light emitting devices", *Appl. Phys. Lett.*, **1998**, *72*, 519.

[15] J. L. Chen, V. Leblanc, S. H. Kang, P. J. Benning, D. Schut, M. A. Baldo, M. A. Schmidt, V. Bulovic, "High definition digital fabrication of active organic devices by molecular jet printing", *Adv. Funct. Mater.*, **2007**, *17*, 2722.

[16] M. Shtein, P. Peumans, J. B. Benziger, and S. R. Forrest, "Direct mask-free patterning of molecular organic semiconductors using organic vapor jet printing", *J. Appl. Phys.*, **2004**, *96*, 4500.

[17] Y. R. Sun, M. Shtein, and S. R. Forrest, "Direct patterning of organic light-emitting devices by organic-vapor jet printing", *Appl. Phys. Lett.*, **2005**, *86*, 113504.

[18] M. S. Arnold, G. J. McGraw, S. R. Forrest, R. R. Lunt, "Direct vapor jet printing of three color segment organic light emitting devices for white light illumination", *Appl. Phys. Lett.*, **2008**, *92*, 053301.

[19] Y. Y. Noh, and H. Sirringhaus, "Ultra-thin polymer gate dielectrics for top-gate polymer field-effect transistors", *Org. Elec.*, **2009**, *10*, 174.

[20] S. Biswas, K. P. Pipe, M. Shtein, "Solvent-free, direct printing of organic semiconductors in atmosphere", *Appl. Phys. Lett.* **2010**, *96*, 263301.

[21] M. Shtein, P. Peumans, J. B. Benziger, and S. R. Forrest, "Direct, mask- and solvent-free printing of molecular organic semiconductors", *Adv. Mater.*, **2004**, *16*,

1615.

[22] Z. D. Popovic, H. Aziz, A. Ioannidis, N. X. Hu, P. N. M. Anjos, “Long-term degradation mechanism of tris(8-hydroxyquinoline) aluminum-based organic light-emitting devices”, *Synth. Metals* **2000**, *111*, 229.

[23] J. McElvain, H. Antoniadis, M. R. Hueschen, J. N. Miller, D. M. Roitman, J. R. Sheats, R. L. Moon, “Formation and growth of black spots in organic light-emitting diodes”, *J. Appl. Phys.*, **1996**, *80*, 6002.

[24] S. V. Patankar, *Numerical heat transfer and fluid flow* (Hemisphere Publications, New York), **1980**.

[25] M. C. Green and G. V. Miram, “Method for making a cathader with integral shadow grid”, *U.S. Patent 4994709*, **1991**.

[26] J. A. Rogers, Z. Bao, A. Makhija, and P. Braun, “Printing process suitable for reel-to-reel production of high-performance organic transistors and circuits”, *Adv. Mater.*, **1999**, *11*, 741.

[27] K-B. Kim, Y-H. Tak, Y-S Han, K-H Baik, M-H. Yoon and M-H. Lee, “Relationship between Surface Roughness of Indium Tin Oxide and Leakage Current of Organic Light-Emitting Diode”, *Jpn. J. Appl. Phys.*, **2003**, *42*, 438 (2003).

[28] P. E Burrows. Z. Chen, V. Bulovic, M. McCarty, S. R. Forrest, J. A. Cronin and M. E. Thompson, “Relationship between electroluminescence and current transport in organic heterojunction light-emitting devices”, *J. Appl. Phys.*, **1996**, *79*, 7991.

CHAPTER 4

Fabrication of OPVs by GF-OVJP

4.1. Requirements for OPV active materials deposition

One of the most attractive routes to clean solar energy generated electricity is the development of large-scale, efficient, flexible, small molecular organic photovoltaic (OPV) cells. [1] To realize this goal requires a low-cost, scalable, rapid device processing technique with potentially high materials utilization efficiency. [2] In the extreme, it may be desirable to achieve direct deposition of OPVs on surfaces of interest (e.g. rooftops of cars, surfaces of buildings, textiles, etc.) with high efficiency and speed. With rapidly increasing record efficiencies (e.g. > 10%) for vacuum-deposited small molecular organic photovoltaic (OPV) cells, [3] interest is building in developing potentially more cost-effective means of depositing small-molecular organic semiconductor materials which define the active layers of these devices. One of the potential manufacturing cost reduction avenues is developing new techniques for optoelectronic device deposition in the ambient without the use of vacuum or solvent-based processing. While this may appear to be an industrial challenge, virtually none of the current methods of organic photovoltaic material growth [4-9] can be carried out in the ambient environment. In addition, a better understanding of the dependence of morphology (roughness and crystallinity) of the organic thin films in alternate OPV structures is essential for the development of flexible and non-planar OPV geometries.

As demonstrated in **Chapter 3**, GF-OVJP is a viable technique for depositing organic semiconductor materials in air for device applications. [10] The technique can be extended to the growth of small molecular organic photovoltaic films in air; both the electron donor and acceptor layers of an organic solar cell. The effects of guard flow rate on the deposited active layer film morphology and on the resulting device characteristics are elucidated in this Chapter, with the section on standard OPV structures extracted from previously published work by Biswas *et al.* (2012). [11] Interestingly, the use of high velocity gas flow allows for the crystallinity to be increased while reducing film roughness, in contrast to typical growth or annealing approaches that increase roughness. [12, 13] Enhanced crystallization while depositing on nearly room-temperature substrate is observed, adding a new dimension to the body of knowledge in the OPV and film growth research domains. [12, 14] Further, inverted OPV structures are fabricated with all the active layers (acceptor and donor) deposited in air with measured power conversion efficiency of up to 1.4%. The relation of morphology and standard- and inverted-OPV device performance with the processing parameters of GF-OVJP is investigated here systematically.

4.2. Standard OPV fabrication

A standard single, planar heterojunction OPV structure with archetypal charge / exciton transport layers is chosen for this study. **Figure 4-1** shows the standard structure with energy levels and the active semiconductor materials used. A schematic J-V curves is also provided in order to define the OPV cell performance characteristics.

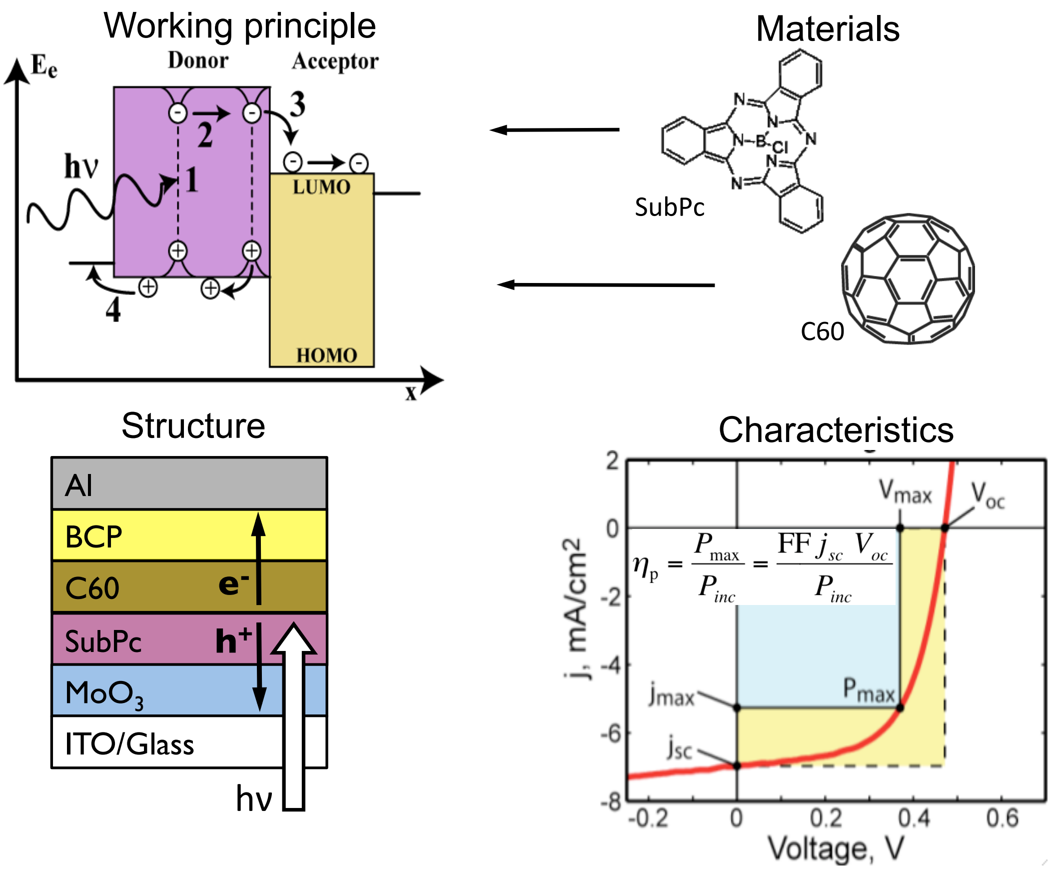

Figure 4-1. Standard OPV structure, materials and device characteristics. Images from [15]

Organic photovoltaic cells convert energy from light into electrical current with an electronic potential that can drive an external load. The details of this conversion process for a standard OPV cell are illustrated in **Fig. 4-1**. The four step process start with photon absorption (Step 1) resulting in an excited state relaxation of the electron-hole pair forming an exciton. The generated exciton is a neutral quasi-particle that exhibits lifetimes ranging from nanoseconds to micro- and milliseconds [16]. As the generated exciton diffuses, it can recombine (i.e. decay) through photon or phonon emission (Step 2). If the exciton diffuses to the interface between the donor and acceptor layer, it will dissociate into free charges (Step 3), provided there exists a net thermodynamic driving force for forming the charge-separated state, and provided the transition to free charges overcomes the Coulombic binding energy of the exciton, which can range between 0.1 and 2 eV [17]. Finally, the free charges diffuse to the electrodes where they are collected (Step 4). The free charges may also recombine before being extracted from the device due to several possible mechanisms including impurity trap states. The solar power conversion efficiency (η_P) is the ratio of the electrical power produced by the cell to the incident power of the solar irradiation (P_i). The power conversion efficiency is the product of the short circuit current (J_{SC}), open circuit voltage (V_{OC}), and the fill factor (FF), given by $\eta_P = J_{\mathrm{SC}} V_{OC} \mathrm{FF}/P_i$.

The generalized Shockley equation [18] describes the J-V characteristics of a solar cell. The Giebink model is a further improvement of this relationship for bilayered organic photovoltaic devices. [19] From these models it is known that morphology of the active layers plays an integral role in determining the J_{SC}, V_{OC} and FF of the OPV. [20] In this section the donor, and later, the acceptor semiconductors are deposited by GF-OVJP in air, and the correspondence between processing parameters and film morphology is identified. The effects of particular film morphologies on device performance are also explored.

4.2.1. Donor layer deposition

To isolate the effects of process parameter variation in GF-OVJP, this section focuses on the vapor jet deposition of the just the donor (SubPc) layer, comparing the performance of vapor jet printed films to those deposited in vacuum using otherwise identical device structures. [11]

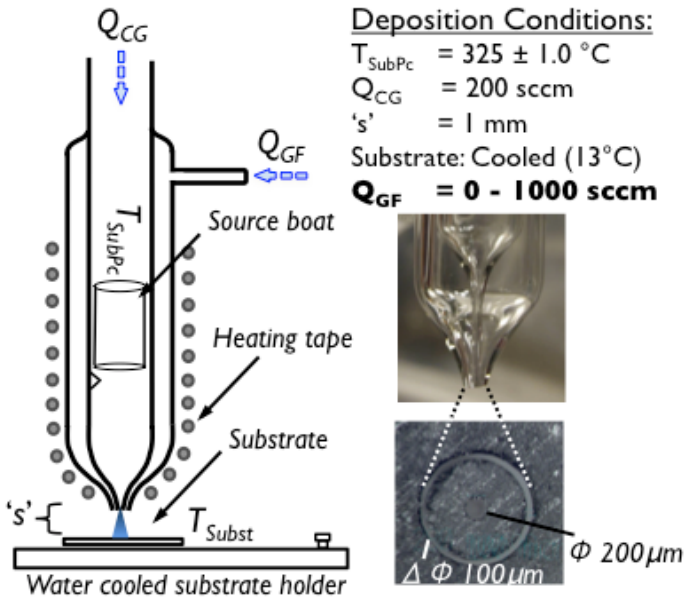

Figure 4-2. Schematic of the GF-OVJP set up for SubPc deposition, along with the deposition conditions. The nozzle provides for an inert guard jet to isolate and hydrodynamically focus the organic vapor-containing primary jet when printing in atmosphere. [11]

The test devices were deposited onto glass substrates pre-coated with 150 nm of indium tin oxide (ITO) with a sheet resistance of 20 Ω/sq (Delta Technologies, Ltd.). Substrates were cleaned by ultrasonication in detergent solution and deionized water followed by heated acetone, trichloroethylene, and isopropanol for 10 minutes each. Substrates were then placed in boiling isopropanol for 5 minutes, dried in pure nitrogen gas, and exposed to ultraviolet-ozone ambient for 10 minutes immediately prior to film deposition. 5 nm of MoO_3 (deposition rate - 0.5 Å/s) was deposited to modify the work function of ITO [21] using a VTE chamber (Angstrom Engineering Inc.). This layer was then exposed to air. 13 nm thick SubPc layer was then deposited in the VTE chamber (deposition rate - 0.5 Å/s) or by GF-OVJP in ambient. Onto these substrates 33.5 nm of the acceptor, C_{60} (deposition rate - 1 Å/s) and 10 nm of buffer layer BCP (deposition rate - 0.5 Å/s) were deposited by VTE. An array of 1 mm diameter cathodes consisting of 100 nm of Al (deposition rate - 1 - 5 Å/s) were deposited through shadow masks using VTE. [22, 23] The OPVs were tested in ambient, and under 1.5 AM illumination (1 Sun) using a Oriel 91192 Newport solar simulator and an Agilent 4156B semiconductor parameter analyzer. Transfer matrix simulations were employed to determine the layer thicknesses, such that the optical field intensity was maximum at the OPV cell heterojunction. [24]

The deposition apparatus (**Fig. 4-2**) was configured as follows. A 19 mm diameter outer glass tube was fused to 12 mm diameter inner glass tube. The two concentric tubes were pulled to form a dual nozzle tip, having a 450 μm first internal diameter, and a 200 μm second internal diameter. The annular gap between the two nozzles at the working end of the apparatus was 100 μm. The nozzle was cleaned with acetone, isopropanol and trichloroethylene solvents, dried with nitrogen and wrapped on the outside with 0.5” wide, 24” long tape heater having a total electrical resistance of 133 Ω. The heating coil was connected to a PID temperature controller and a 1/16” K-type thermocouple was used to maintain the temperature of the source. The source consisted of 0.18 g of prepurified SubPc powder, contained by pieces of quartz wool inside of the inner glass tube, upstream of the nozzle in the heated section. Mass flow controllers (Sierra Instruments, Inc.) were connected to the inner and outer nozzles to vary the flow from 0 to 1000 sccm. Silicon substrates (2.5 x 2.5 cm^2) were mounted on a computer-controlled X-Y positioning stage (Thorlabs) and aligned perpendicular to the nozzle axis for patterning and the film thickness is controlled by the raster rate of the substrate. The annular channel was angled at 15° from the nozzle axis. The process parameters, as shown in **Fig. 4-2**, include nozzle-substrate separation, *s*, sublimation zone temperature, T_{Ev}, substrate temperature, T_S, carrier gas flow rate, Q_{CG} and guard flow rate, Q_{GF}. (The effects of varying Q_{GF} on SubPc film morphology and OPV cell performance are reported here.) The sublimation zone was held at T_{Ev} = 325.0 ± 0.5 °C, while *s* was maintained at 1 mm for all experiments. The flow rate of nitrogen through the inner nozzle, Q_{CG}, was held constant at 200 sccm. The substrate was fixed on a water-cooled holder and maintained at a temperature of 13.0 °C. The guard flow rate was varied from 0 to 1000 sccm.

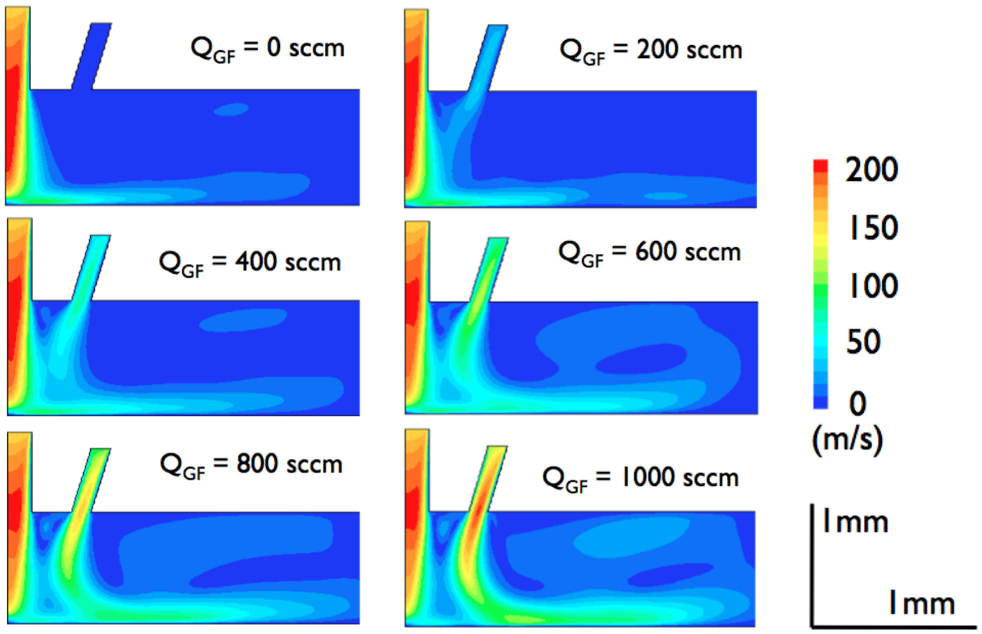

Figure 4-3. Simulated velocity contours indicate improved shielding of the primary jet from ambient air with increase in guard flow rate. [20]

The hydrodynamics of guard flow-enhanced film growth were studied using FLUENT 6.3.26 software (details in **Chapter 3**). As **Fig. 4-3** shows, the velocity contours increase shielding of the primary jet with increasing guard flow. The increase in guard flow is also seen to narrow the deposition region, partly by focusing the inner jet, partly by rapidly convecting outward molecules diffusing to the extreme periphery of the inner jet, as evident in the concentration profiles in **Fig. 4-4**. (An exhaust manifold can be used to capture and potentially recycle this material. [25]) Note that to coat the entire substrate evenly with SubPc, the narrow nozzle was rastered across the substrate. [26] The deposition rate directly underneath the nozzle remained the same for the range of Q_{GF} tested, but the “wing” region of the deposit experienced a slower growth rate at higher Q_{GF} (**Fig. 4-5**), requiring a slower rastering speed to produce a film of a given thickness over the entire area of interest at higher guard flow rates.

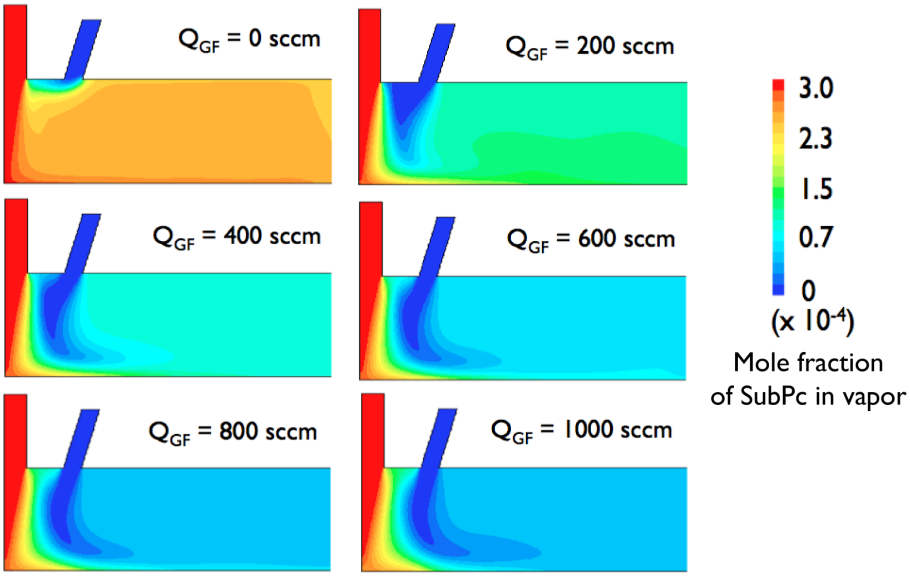

Figure 4-4. Simulated SubPc concentration contours shows that the organic vapor is confined and collimated during deposition at guard flow rates. [20]

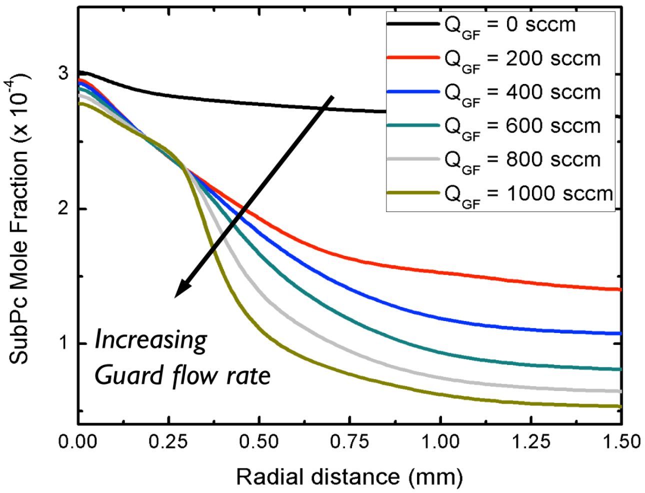

Figure 4-5. Simulated SubPc molecular flux above the substrate indicates that the deposits become more defined with increase in Q_{GF} as some of the organic molecules in the 'wing' region are carried away by the guard jet.

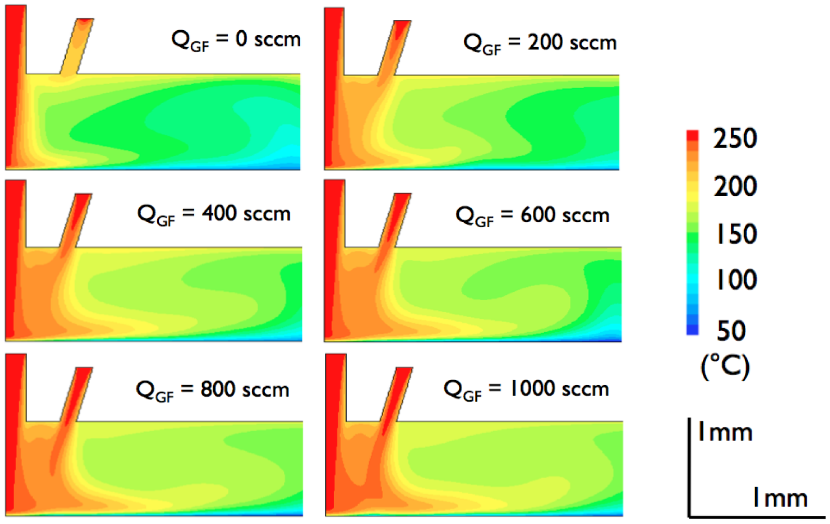

Figure 4-6. Temperature of the jet above the substrate increases with guard flow rate. The thermal energy of the organic molecules is thus higher resulting in increased crystallinity of the deposited film. [20]

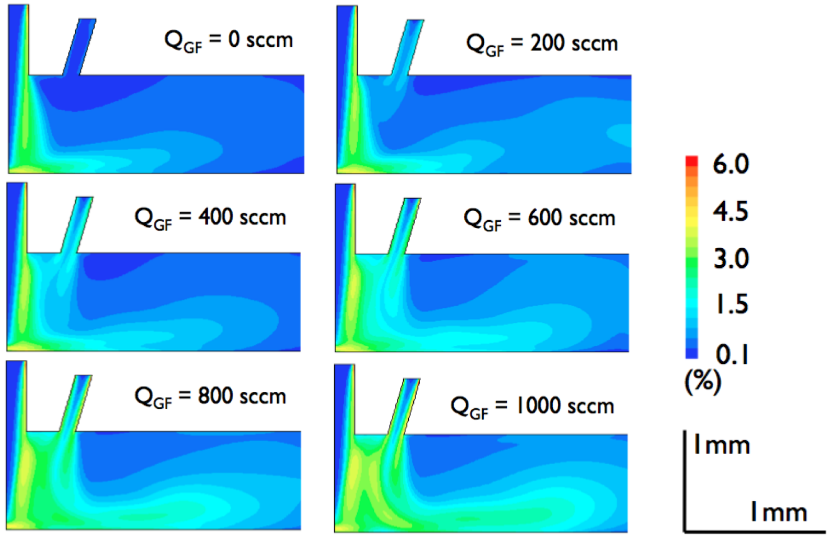

Figure 4-7. The turbulence intensity of the jet above the surface increases with guard flow rate. As a result the boundary layer gets thinner and te SubPc molecules have higher kinetic energy during and after deposition.

The temperature contours in **Fig. 4-6** show that higher guard flow imparts more heat to the top of the substrate (and film) during deposition, potentially useful in increasing the molecular ordering within the stratum of film being deposited, particularly at higher guard flows. Such a “top-down” ordering process is distinct from bulk or “bottom-up” annealing that takes place when a pre-deposited film is annealed on a hot plate or in a furnace. Furthermore, at higher guard flows, the turbulence intensity, defined as the ratio of mean turbulent velocity fluctuation to the mean velocity of flow, increases, as shown in **Fig. 4-7**. With greater turbulence, the boundary layer at the substrate becomes thinner, and the admolecules are expected to maintain more of their initial kinetic energy as they condense on the surface, potentially enhancing their surface diffusion, leading to greater structural order. Indeed, the effect of hydrodynamics of increasing guard flow rate on the deposited film morphology appear to be supported by ϴ-2ϴ X-ray diffraction patterns in

Fig. 4-8, where the SubPc film becomes more crystalline at higher guard flow rates. These XRD data were obtained for 13 nm of SubPc films deposited by GF-OVJP, as were utilized in the photovoltaic devices discussed below.

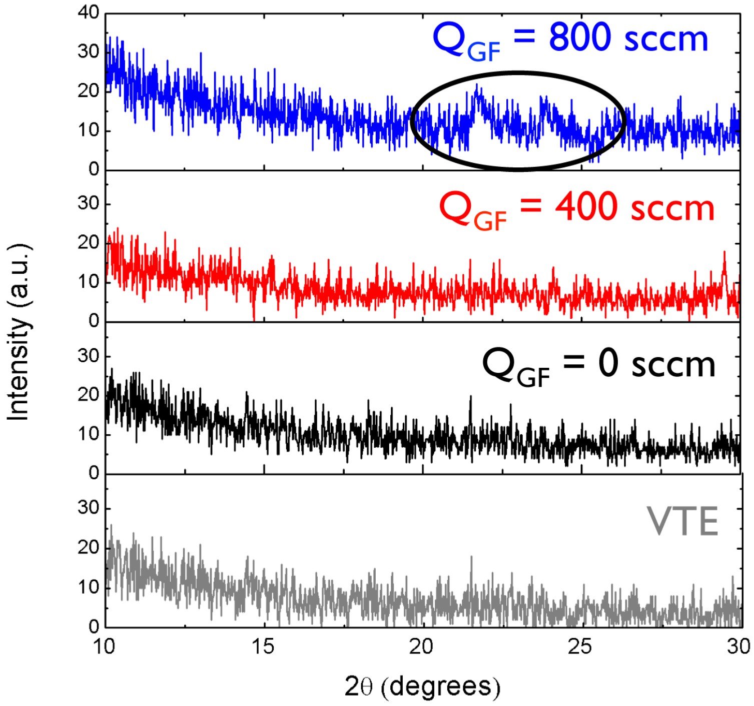

Figure 4-8. The SubPc films deposited by GF-OVJP in air show inception of crystallinity at high guard flow rates. SubPc films deposited by VTE is completely amorphous. [20]

To isolate and study the structure-property relationship resulting from the above process-structure relationship, SubPc films grown by GF-OVJP were used in OPV cells, the remainder of which was deposited using conventional vacuum thermal evaporation (VTE). Organic photovoltaic devices are typically characterized by four main parameters, open circuit voltage (V_{OC}), short-circuit current density (J_{SC}), fill factor (*FF*) and power conversion efficiency (η_P). The J_{SC} is expected to concomitantly increase with SubPc crystallinity, due to improved hole transport through the more ordered donor layer. [13, 27-29] Indeed, **Figure 4-9** shows increased J_{SC} up to Q_{GF} = 800 sccm without significant changes in V_{OC}, with the average η_P increasing up to 1.99±0.07%, with a best case of 2.08 % of the 16 devices measured. The S-kink observed in the J-V characteristics of the GF-OVJP devices is indicative of sub-optimal charge injection at the anode, which also is seen to reduce *FF*, potentially due to the printing process modifying the sub-stoichiometric MoO_{3-x} layer. Nevertheless, the influence of morphology on OPV cell properties is clear, with J_{SC} and the efficiency of OPV cells with SubPc printed at increasing guard flow rates nearly doubled compared to layers printed without the guard flow.

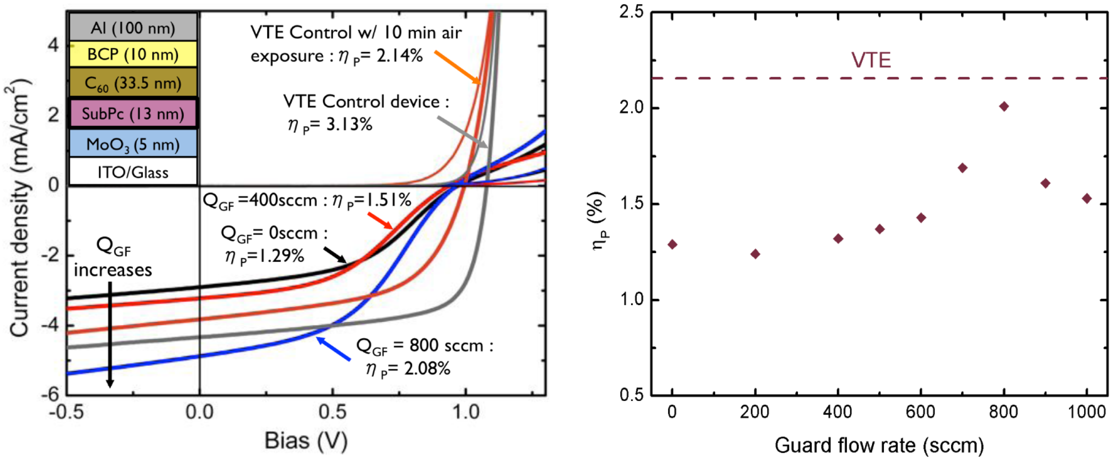

Figure 4-9. J-V characteristics of OPV with donor layer deposited using GF-OVJP in air. J_{SC} increases for high guard flows corresponding to increase in film crystallinity. These are compared to control devices fabricated by VTE. The power efficiency of the OPVs with SubPc deposited in air increases with Q_{GF}, up to 800 sccm. [20]

While the efficiency of OPV cells with SubPc deposited in air by GF-OVJP increases monotonically with guard flow (attributed to a combination of increasing film crystallinity (**Fig. 4-8**) and improved shielding (**Fig. 4-3**)), a sharp drop in efficiency occurs at guard flow rates exceeding 800 sccm. To understand this further, the contributing factors to efficiency are individually plotted in **Fig. 4-10**.

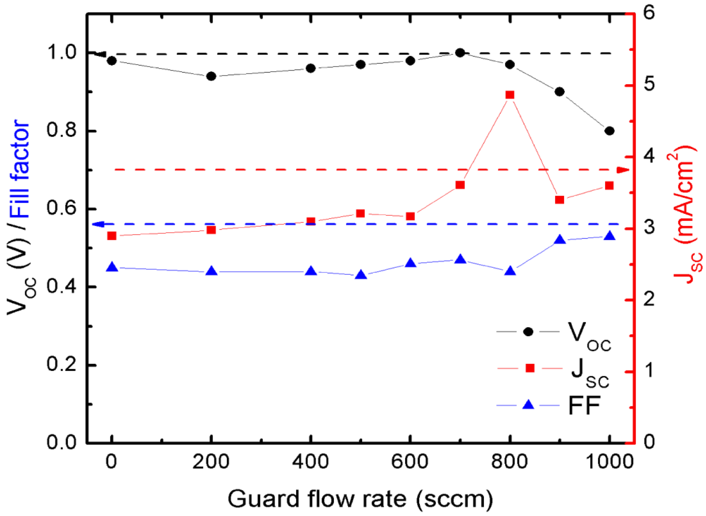

Figure 4-10. Plot of individual contributing factors of OPV characteristics with guard flow rate. [20]

We attribute the drop off in V_{OC} and J_{SC} at $Q_{GF} \geq 900$ sccm to two main factors. First, we hypothesize that the higher degree of ordering of the SubPc molecules deposited at higher guard flow rates persists to the donor-acceptor interface, which has been shown previously [19] to lower V_{OC}. Second, we note that the trend in the atomic force microscopy derived RMS roughness of the SubPc films in **Fig. 4-11** deposited at various guard flows is directly correlated to the trends observed in the device performance. The smoothest films are measured for 800 sccm guard flow after which large surface irregularities emerge, similar to morphologies resulting from post-deposition thermal annealing. [30] Thus, we conclude that the ability to obtain smooth films with enhanced crystallinity requires a specific process window and may be a unique attribute of the GF-OVJP film growth technique. The trends observed in the J_{SC} and η_P could be seen as a result of thickness variation for various deposition conditions, since SubPc/C_{60} OPVs are highly sensitive to active layer thickness [13]. However, we have calibrated the GF-OVJP setup to consistently deposit 13 nm SubPc films at all the guard flow reported above with less than 1 nm thickness variation. More work is needed to further understand the interplay of material properties, process parameters, and surface morphology that give rise to the unique processing-structure relationships of the GF-OVJP technique.

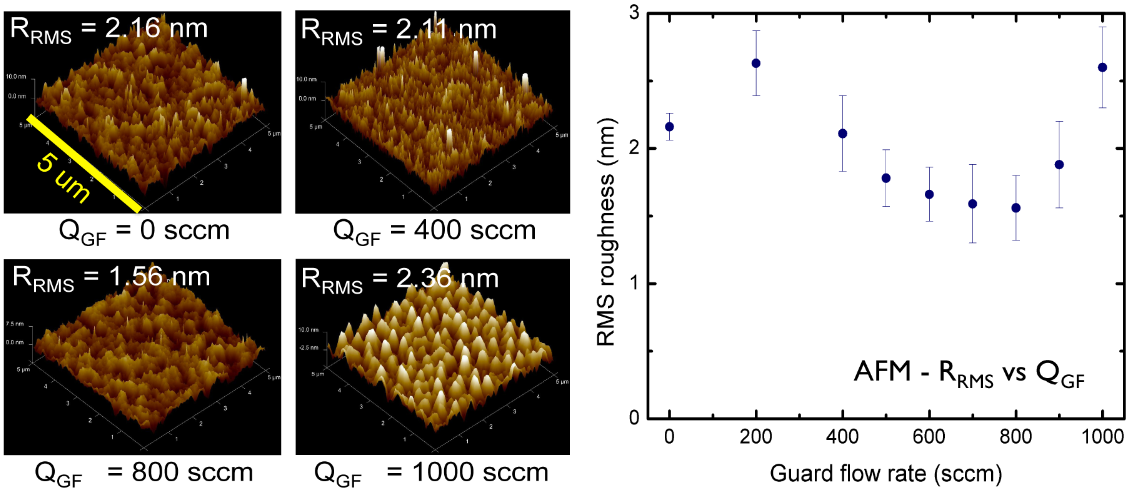

Figure 4-11. RMS roughness of deposited films with guard flow. The lowest roughness is observed around 800 sccm. Lower roughness and higher crystallinity of the deposited films is unique to growth by GF-OVJP. [20]

4.2.2. Control devices (Standard structure)

For the GF-OVJP apparatus configuration used in the experiments, the printed donor film must be transferred through air prior to the deposition of the acceptor, buffer and cathode. Thus, a comparison to additional control devices deposited by VTE (J-V plots in **Fig. 4-12**) can be illuminating. The control devices also enables the reader to understand the effects of post-deposition exposure on the SubPc donor layers. For example, all-VTE grown control device had none of the layers exposed to air and exhibited η_P = 3.04 ± 0.08 % measured under AM 1.5 solar illumination.

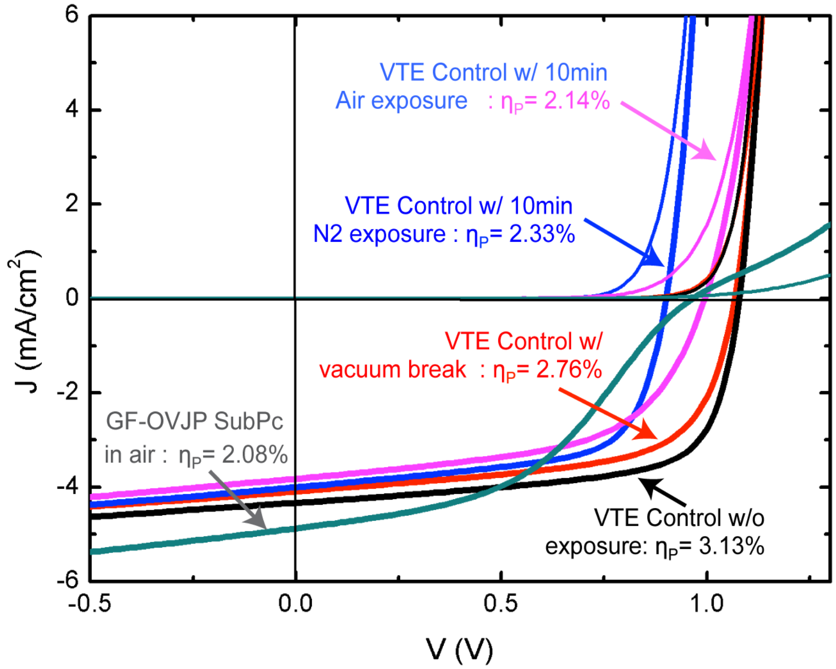

Figure 4-12. Plot of J-V characteristics of control OPV devices with different degrees of exposure post-deposition of the SubPc donor layer.

OPVs with vacuum-deposited SubPc films, when subjected to a vacuum break (1minute exposure to N_2) exhibits a drop in both J_{SC} and V_{OC}, with an average power efficiency of $\eta_P = 2.71 \pm 0.05$ % and best device $\eta_P = 2.76$ %. The trend continues when the deposited SubPc layer is left in a N_2 glovebox for 10 minutes (duration of time comparable to a typical printing and transfer from the GF-OVJP apparatus to the vacuum deposition system), showing an average $\eta_P = 2.30 \pm 0.03$ %. This indicates to the dopping of N_2 in the deposited SubPc layer, probably resulting in trap states, and therefore, decreasing η_P. VTE-deposited SubPc films that are exposed to air for 10 minutes yield the same efficiency and V_{OC} as SubPc films printed at the optimal guard flow rate (here, 800 sccm). The V_{OC}, FF and J_{SC} of the air exposed control device dropped resulting in an average $\eta_P = 2.09 \pm 0.04$ % and best device $\eta_P = 2.14$ % – comparable to $\eta_P = 2.08$ % obtained for the device printed by GF-OVJP, suggesting that, indeed jet-printing alone does not degrade the SubPc layer's performance in the 4th quadrant, provided sufficiently high guard flow rates are used, as seen in the J–V characteristics in **Fig. 4-12**. In fact, slightly higher J_{SC} is observed for $Q_{GF} = 800$ sccm than the control, attributed to enhanced film crystallinity. Note, however, that the emergence of an S-shaped J–V curve of the printed device lowers *FF,* resulting in a slightly lower power efficiency than the vacuum-grown control devices. The use of alternate work-function modifying and blocking layers or inverting the device stack can be explored to ensure better charge injection at the anode to mitigate this effect in GF-OVJP deposited OPVs.

Local deposition rates of organic thin films by GF-OVJP in air can exceed 1,000 Å/s, orders of magnitude faster than conventional growth in vacuum, while enhanced molecular ordering can be obtained even on uncooled substrates at the very high deposition rates. Increasing the guard flow rate up to a particular value during donor layer deposition improves photocurrent.

The use of N_2 as the carrier gas and guard flow probably has detrimental effects on the donor layer electronic properties. Helium or Argon would be better choices of gases for future work related to GF-OVJP. Modifications to the apparatus to enable the deposition of acceptor materials by adjacent nozzles allows for the deposition of all the active organic layers in a single step. Hence, C_{60} (acceptor semiconductor) deposition by GF-OVJP in air is investigated next.

4.2.3 Acceptor layer deposition (*Standard structure*)

The experimental apparatus for deposition of fullerene (C_{60}) are almost identical to the SubPc GF-OVJP nozzle, described in the previous section. The apparatus and deposition conditions are shown in **Figure 4-13**. Powdered C_{60} is loaded in the sublimation zone and heated to $T_{Ev} = 520.0 \pm 0.5$ °C. s is maintained at 1 mm while the Q_{CG} held constant at 200 sccm. The substrate is fixed on a water-cooled holder and maintained at a temperature of 13.0 °C. The guard flow rate is varied from 0 to 1000 sccm. Guard flow rate is the only parameter varied for two reasons: it is expected to improve the shielding of the organics from air and add kinetic and thermal energy to the molecules which potentially increases the crystallinity of the film – both these should improve device performance.

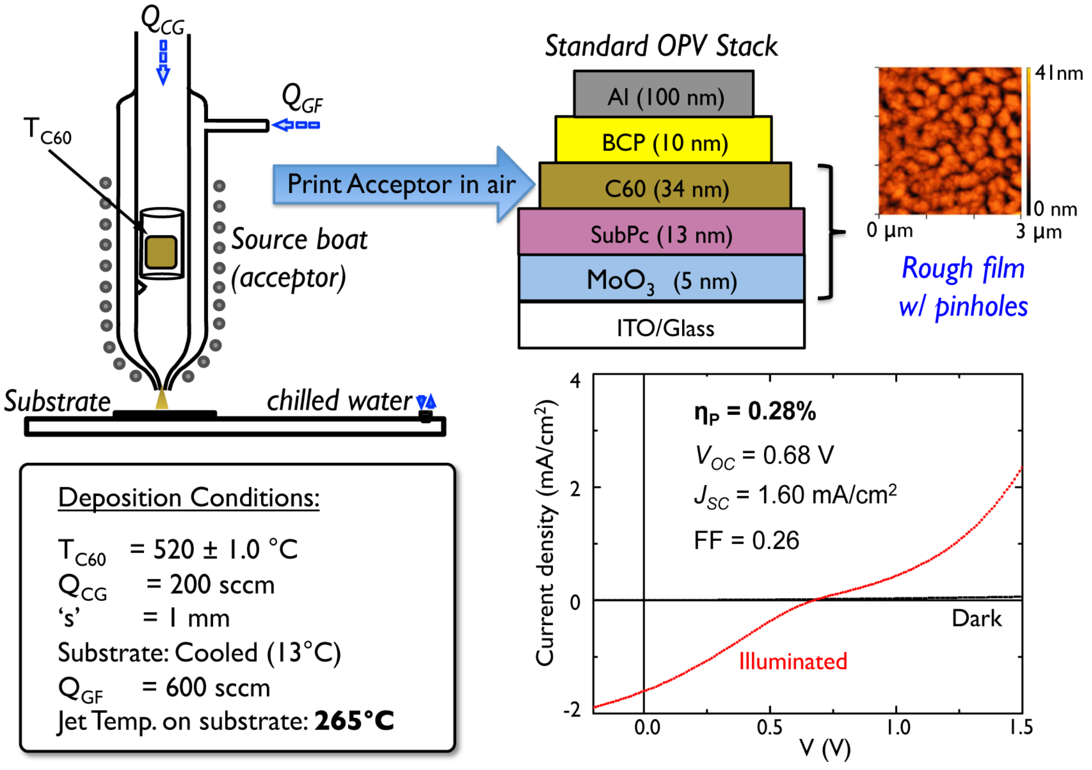

Figure 4-13. GF-OVJP deposition of acceptor layer in air: Experimental set up of the nozzle for C_{60} film growth with the deposition conditions used is shown. When C_{60} is deposited in air using GF-OVJP in a standard OPV stack, η_P = 0.28 %. Poor device performance is due to local evaporation of the underlying SubPc layer at extremely high jet temperature on the substrate. [31]

After establishing that C_{60} thin film can be grown on glass and silicon substrates at the above mentioned processing conditions, fabrication of a standard structure OPV was attempted with only the C_{60} layer grown in air by GF-OVJP. 5 nm molybdenum oxide (MoO_3) followed by 13 nm of SubPc were deposited by VTE on ITO coated glass substrates. C_{60} was then jet printed on this SubPc layer at the condition mentioned above and in **Fig. 4-13**. The rest of the layers were completed in vacuum. Figure 1c shows the standard stack (with just C_{60} deposited by GF-OVJP) and resulting device performs poorly with an efficiency of less than 0.5%. C_{60}, unlike most other organic semiconductors, has a really high evaporation temperature at atmospheric pressure of ≥ 500 °C. The jet temperature measured on the substrate was about 265 °C, which is quite close to the sublimation temperature of SubPc. Hence, the underlying film directly under the jet desorbs and redeposits elsewhere, leaving holes, as seen from the AFM micrograph in **Fig. 4-13**, with a peak to valley roughness of 41 nm in a 50 nm total film thickness. Thus, the standard stack cannot be used for jet printing C_{60} on other organic films.

To test this limitation of GF-OVJP further, a VTE deposited SubPc film is exposed to a hot N_2 jet, without C_{60}, as a control. The hot jet temperature on the substrate is measured to be 265 °C. After the SubPc layer's hot jet exposure, C_{60} is deposited by VTE and the standard OPV device is completed and tested. The performance characteristics of the control device, as shown in **Figure 4-14**, worse than when the C_{60} layer was deposited with GF-OVJP, with a maximum η_P = 0.09 %. As mentioned earlier in the chapter, organic molecules deposited by GF-OVJP have higher kinetic and thermal energies than when deposited by VTE. Hence the C60 molecules when deposited by GF-OVJP can fill the pinholes left in the underlying SubPc layer, unlike when deposited by VTE. This is schematically shown in **Fig. 4-14**.

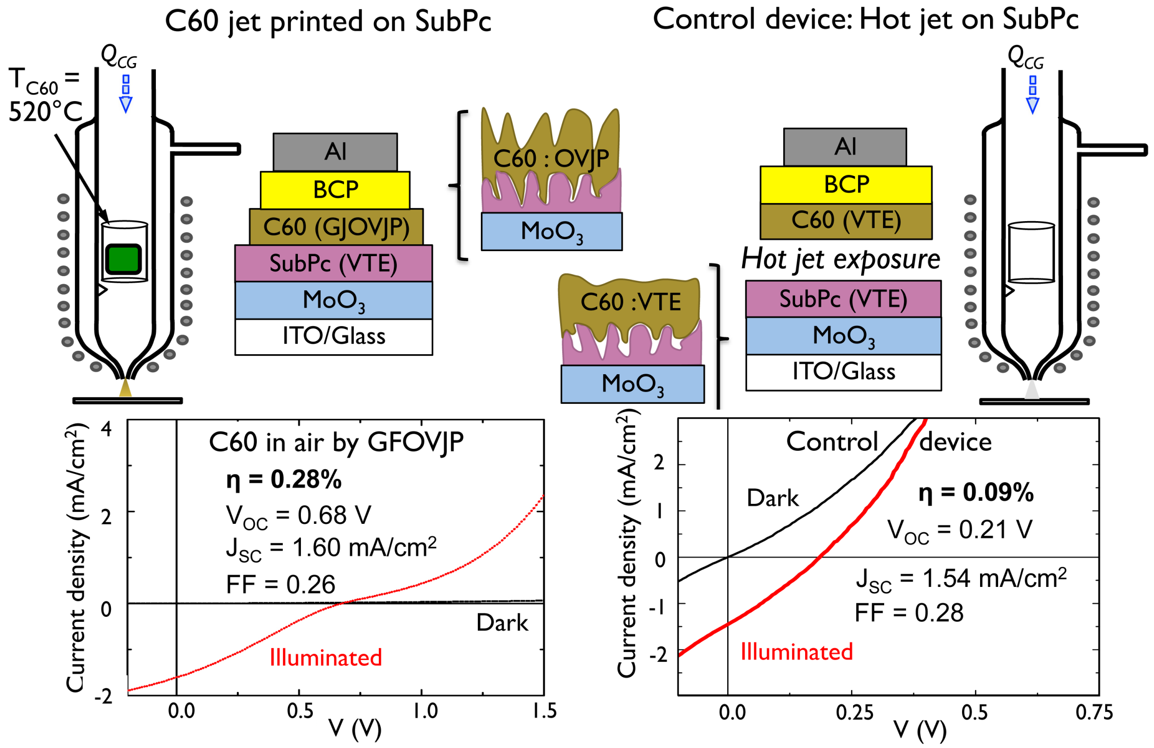

Figure 4-14. Effect of hot jet exposure to VTE- deposited SubPc layer causes pinholes to form in the film due to evaporation and re-condensation elsewhere of the material.

A limitation of GF-OVJP is that extremely high evaporation/sublimation temperature materials cannot be deposited on top of films of materials with low sublimation temperature, without significant modification the nozzle design.

4.3. Inverted OPV fabrication

To circumvent the GF-OVJP limitation mentioned above, 'inverted' OPV stack or i-OPV was investigated. The hot jet with C_{60} can then be deposited directly on top of the cathode/substrate, followed by SubPc film deposition. Recent research suggests inverted OPV structures are advantageous for use on non-transparent, non-planar substrates and for longer lifetime devices, [32] but here this option is explored primarily to overcome the degradation of film quality when a material with extremely high evaporation temperature is jet printed on a lower sublimation temperature material. This drawback of GF-OVJP was further realized when tried making a device with lithium fluoride (LiF) as the work function modifier of the cathode. As C_{60} was jet printing on 2 nm of vacuum deposited LiF, the underlying film was damaged and the resulting device showed a tenth of the efficiency recorded for a vacuum deposited control device. LiF has a low melting point of ~ 600 °C and was damaged in the jet printing process. Thus, a thin layer of thermally evaporated Mg to used to lower the work function of ITO, thereby making it the cathode while Al is used as the anode, [33] as seen from the band diagram in **Fig. 4-15**. C_{60} was jet printing while varying only the guard flow rate from 0 to 1000 sccm, while maintaining all other deposition conditions the same as **Fig. 4-13**.

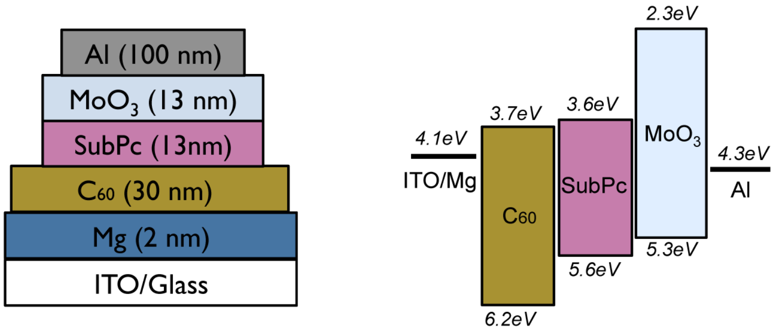

Figure 4-15. i-OPV stack with the energy band diagrams are reported by Hancox et al. (2010). [33]

4.3.1 Acceptor layer deposition (*Inverted structure*)

Similar to the deposition of the donor layer, the effects of guard flow rate variation in GF-OVJP deposition of the just the acceptor layer (C_{60}) layer is the focus of this section, comparing the performance of vapor jet printed films to those deposited in vacuum using otherwise identical i-OPV structures.

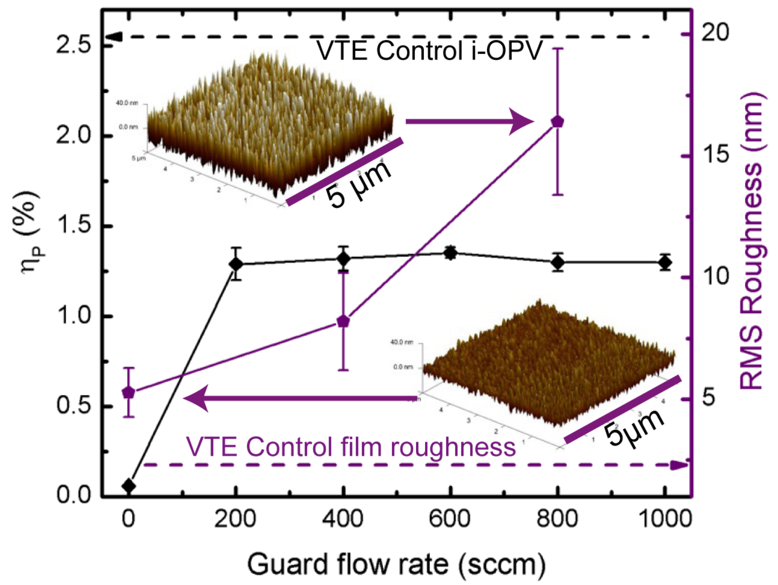

Figure 4-16. RMS roughness of 30 nm C_{60} films and the power efficiency of i-OPV devices using these films, deposited in air by GF-OVJP, indicate improved molecular ordering in the films. [33]

The average power efficiency of the i-OPV devices with C_{60} deposited in air by GF-OVJP with Q_{GF} = 0 sccm is measured to be η_P = 0.07 %. However, the η_P jumps to 1.24 ± 0.3 % with a guard flow rate as small as Q_{GF} = 200 sccm, as seen in **Fig. 4-16**. This is due to the shielding effect discussed earlier of the guard flow jet. Electronic / excitonic transport properties of C_{60} films is greatly susceptible to oxygen and moisture exposure. [34] Hence, the jump in the power efficiency of the i-OPV devices when the guard flow jet is turned on is expected. However, there is no noticeable peak in the power efficiency with guard flow rate, with the best η_P = 1.42 % for Q_{GF} = 600 sccm, as plotted in **Fig. 4-16**. With the *FF* remaining relatively constant with Q_{GF}, the decrease in the V_{OC} and increase in the J_{SC} (plotted in **Fig. 4-17**) cancel each other out. The V_{OC} is mainly dependent on the donor-acceptor interface, and hence a higher degree of molecular ordering in the C_{60} film deposited at higher guard flow rates persists to the donor-acceptor interface, which has been shown previously [19] to lower V_{OC}.

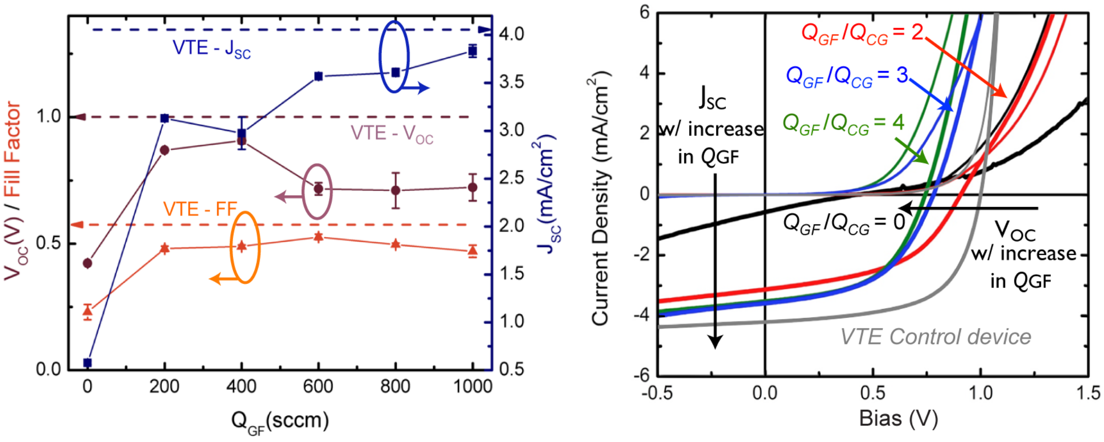

Figure 4-17. Trends in performance characteristics measured for i-OPV devices with 30 nm C_{60} films deposited in air by GF-OVJP.

Even though there is no obvious enhancement in the degree of crystallinity of the films deposited, computational fluid dynamics simulations show increased heat transfer and higher turbulent kinetic energy of the admolecules at higher guard flow rates. This presumably results in a higher molecular ordering in the C_{60} film. The 17% increase in the RMS roughness (**Fig. 4-16**) is also a direct result of the higher energy of C_{60} molecules reaching the substrate at high guard flow rates. The increase in crystalline domains in the film with guard flow rate results in an increase in J_{SC} of the i-OPV devices, as seen in **Fig. 4-17**. The GF-OVJP processing conditions tested for the present work is outside the window to enhance the device performance considerably. More work needs to be done at even higher guard flow rates in order to optimize the deposition condition to observe a significant enhancements in the device performance

Although, the efficiencies of the devices fabricated with GF-OVJP in air were lower than the control devices, morphological tunability was achieved to selectively increase the ordering in the film deposited by GF-OVJP by varying the guard flow rate. We analyze this further by fitting the dark and illuminated J-V curves to extract the recombination rate (resulting in lower V_{OC}) and the higher exciton flux and transport (resulting in higher J_{SC}) with increase in guard flow rate.

4.3.2. All active layers in air

The ability to directly deposit device quality films in ambient of active small molecular OPV materials on surfaces of interest (e.g. rooftops of cars, surfaces of buildings, textiles, etc.) is highly desirable in order to attain low cost manufacturing of OPVs which is vacuum-, solvent- and mask-free. This section focuses on the first reported attempt at achieving this goal.

The best power efficiency of the inverted organics photovoltaic cells (i-OPV) with the C_{60} layer deposited in air by GF-OVJP is measured to be 1.42%. However, the study is incomplete without a comparison of the device performance to the right control devices deposited by VTE and GF-OVJP. All the inverted devices, as shown in the **Fig. 4-18**, have 2 nm of Mg thermally evaporated on pre-cleaned ITO/Glass substrates without ozone exposure, unlike the standard OPV stacks discussed in **Section 4.2**. The first control device **A** had 30 nm of C_{60} followed by 13 nm of SubPc and MoO_3 each, all deposited by VTE. The samples were then masked and coated with 100 nm of Al. Next, control device **B** was deposited following the same procedure as above, expect for a hot jet exposure at 120 °C (measured jet temperature on substrate when SubPc is jet printed) on the VTE-deposited C_{60} layer. This was done to detect if the underlying layers would be damaged when SubPc was jet printed on top of the C_{60} layer. Control device **C**, was fabricated similar to control device **A**, with 30 nm of C_{60} deposited by VTE followed by 13 nm of SubPc jet printed in air using a guard flow rate of 800 sccm (best case deposition condition reported in **Section 4.2.1**), followed by 13 nm of MoO_3 deposited by VTE. Control device **D**, as described in the previous section, had C_{60} deposited in air by GF-OVJP with a guard flow rate of 600 sccm, followed by 13nm of SubPc and MoO_3 each deposited by VTE. Finally, device **E** was fabricated with both 30 nm of C_{60} and 13 nm of SubPc deposited in air by GF-OVJP. Device **E** had all the organic layers deposited in air, which is the final objective of this chapter.

4.3.3. Control devices (*Inverted structure*)

The control devices help to isolate the impact of each active layer deposited by VTE and GF-OVJP on the overall device performance. For example, all-VTE grown control device **A** had all organic layers deposited in VTE without any exposure to N_2 or air and exhibited $\eta_P = 2.33 \pm 0.11$ % measured under AM 1.5 solar illumination. The J-V characteristics of plotted in **Fig. 4-19** and the values are listed in **Table 4-1**.

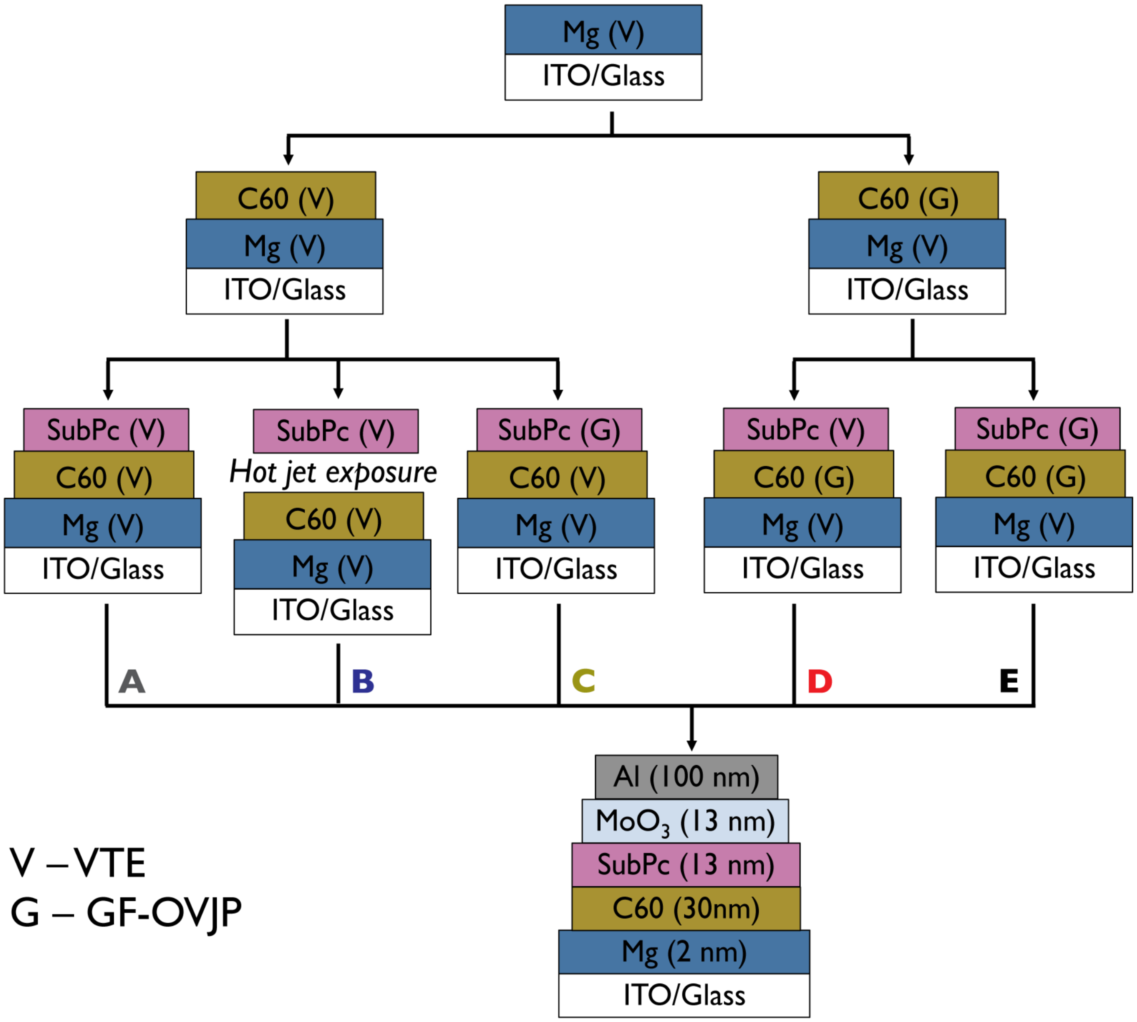

Figure 4-18. Chart of all control devices of i-OPV devices with the donor and acceptor layers deposited by VTE and GF-OVJP. [31]

In order to deposit multiply layered structure by GF-OVJP, the underlying organic layer is always exposed to a hot jet of overlying material. Control device **B** is interesting, since the VTE-deposited C_{60} film is exposed to a hot jet of N_2 at 120 °C in air for 10 minutes. The sublimation temperature of C_{60} at ambient pressure is 520 °C and hence it should not be affected by a 120 °C inert gas jet. However, device B shows a drop in both FF and J_{SC} compared to device **A**. This indicates an incorporation of impurities into the underlying C_{60} layer. Further investigation is warranted to fully understand the morphology and electronic characteristics of device **B**.

Control Device	V_{OC} (V)	J_{SC} (mA/cm^2)	FF	Avg. η_P (%)	Best η_P (%)
A	0.96	4.3	52.3	2.33 ± 0.11	2.46
B	0.93	3.07	41.2	1.18 ± 0.05	1.23
C	0.837	4.48	49.0	1.84 ± 0.03	1.88
D	0.781	3.75	47.2	1.38 ± 0.04	1.42
E	0.68	3.92	49.6	1.32 ± 0.03	1.35

Table 4-1. Device performance characteristics of all the i-OPV control devices, building up to all active layers deposited by GF-OVJP in air.

When only the SubPc layer of an i-OPV is deposited by GF-OVJP in air in Control device **C**, the donor layer is expected to have enhanced crystallinity, as discussed in **Section 4.2.1**. This results in a small drop in V_{OC} and an increase in J_{SC}, when compared to device **A**. The power conversion efficiency was, however, lower than was device **A** and measured to be $\eta_P = 1.84 \pm 0.03$ %. Crystalline SubPc at the interface lowers the V_{OC}. A stack can be designed to have a thin layer of amorphous SubPc at the heterojunction, deposited at a lower Q_{GF}, followed by a higher Q_{GF} crystalline SubPc, to make a significant improvement to the power conversion efficiency of the device. Control device **D** is the same as discussed in the **Section 4.3.1** with only 30 nm of C_{60} film deposited in air by GF-OVJP. Both the V_{OC} and J_{SC} show a large drop, in comparison to device A, and the measured $\eta_P = 1.38 \pm 0.04$ %. Air exposure and non-optimized GF-OVJP deposition conditions affect the C_{60} film more than SubPc or other small molecular semiconductors.

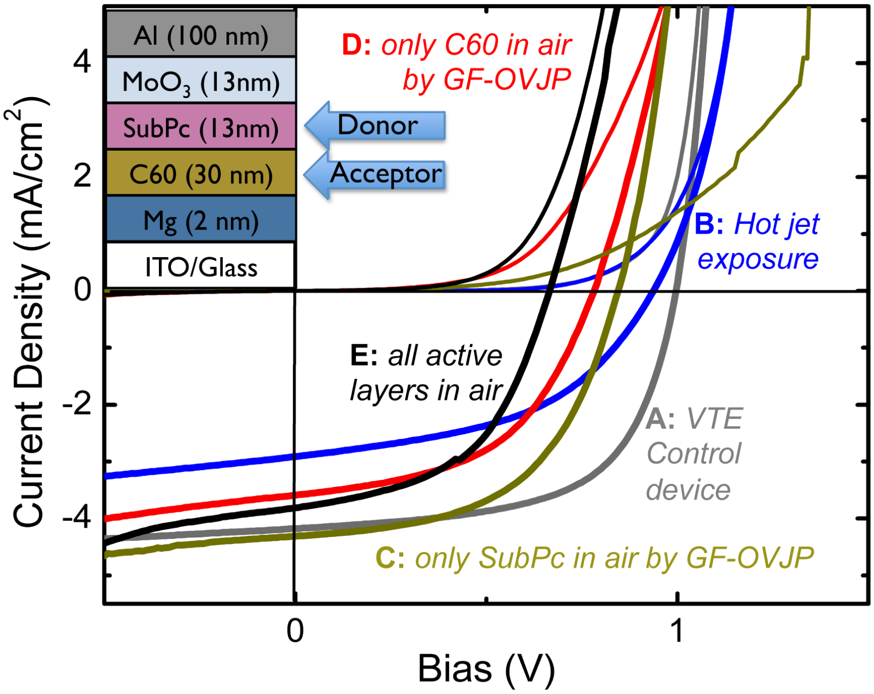

Figure 4-19. J-V curves of control i-OPV devices in order to understand the effects of depositing the active layers by GF-OVJP in air. [31]

Finally, device **E** has both active layers deposited by GF-OVJP in air and has an average η_P of 1.32 ± 0.03 %. Due to the crystalline SubPc deposited by GF-OVJP, the J_{SC} is marginally higher and V_{OC} is slightly lower than control device **D**.

This is the first demonstration of all active layers deposited in air. A power conversion efficiency of 1.3% is not very high and can be improved further exploration and optimization of deposition conditions and processing parameters of GF-OVJP.

4.4. Summary

This chapter layers the groundwork for fabrication of small molecular organic photovoltaic devices using GF-OVJP to enable deposition in air. The technique has various controllable processing parameters that can be utilized to modify the morphology of the deposited films. SubPc, a common OPV donor material, deposited by GF-OVJP in air and roughness and crystallinity of the films are controlled using the guard flow rate. The morphology of the films, in turn, affects the device performance characteristics, which is seen from the donor and acceptor deposition by GF-OVJP. A process – structure relationship has been established for technique and can be used to explore a wide range of OPV structures and designs in the future.

4.5. References

[1] P. Peumans, S. Uchida and S.R. Forrest, “Efficient bulk heterojunction photovoltaic cells using small-molecular-weight organic thin films”, *Nature*, **2003**, *425*, 158-162.

[2] S. Biswas, O. Shalev, M. Shtein, “Thin-Film Growth and Patterning Techniques

for Small Molecular Organic Compounds used in Optoelectronic Device Applications", *Annu. Rev. Chem. Biomol. Eng.* **2013**, *4*, 289.

[3] R.F. Service, "Outlook brightens for plastic solar cells", *Science*, **2011**, *332*, 293.

[4] F. C. Krebs, "All solution roll-to-roll processed polymer solar cells free from indium-tin-oxide and vacuum coating steps", *Organic Electronics*, **2009**, *10*, 761-768.

[5] M. Niggemann, B. Zimmermann, J. Haschke, M. Glatthaar and A. Gombert, "Organic solar cell modules for specific applications—From energy autonomous systems to large area photovoltaics", *Thin Solid Films*, **2008**, *516,* 7181-7187.

[6] M. Shtein, P. Peumans, J. B. Benziger, and S. R. Forrest, "Micropatterning of small molecular weight organic semiconductor thin films using organic vapor phase deposition", *J. Appl. Phys.*, **2003**, *93*, 4005-4016.

[7] M. Baldo, M. Deutsch, P. Burrows, H. Gossenberger, M. Gerstenberg, V. Ban, S. R. Forrest, "Organic vapor phase deposition", *Adv. Mater.*, **1998**, *10*, 1505-514.

[8] D. Vak, S. Kim, J. Jo, S-H Oh, S.-I. Na, J. Kim, and D.-Y. Kim, "Fabrication of organic bulk heterojunction solar cells by a spray deposition method for low-cost power generation", *Appl. Phys. Lett.* **2007**, *91*, 081102-1.

[9] M. Shtein, P. Peumans, J. B. Benziger, and S. R. Forrest, "Direct mask-free patterning of molecular organic semiconductors using organic vapor jet printing", *Adv. Mater.* **2004**, *16*, 1615-1620.

[10] S. Biswas, K. P. Pipe, and M. Shtein, "Solvent-free, direct printing of organic semiconductors in atmosphere", *Appl. Phys. Lett.*, **2010**, *96*, 263301-1-3.

[11] S. Biswas, K. A. Luck, M. Shtein, "Guard flow-enhanced organic vapor jet printing of photovoltaic donor materials in air", *Org. Electron.* **2012**, *13*, 2905.

[12] G. Li, V. Shrotriya, J. Huang, Y. Yao, T. Moriarty, K. Emery, and Y. Yang, *Nature Mater.* "High-efficiency solution processable polymer photovoltaic cells by self-organization of polymer blends", **2005**, *4*, 864-868.

[13] G. Wei, S. Wang, K. Sun, M. E. Thompson, and S.R. Forrest, "Solvent-Annealed Crystalline Squaraine: PC70BM (1:6) Solar Cells", *Adv. Energy Mater.*, **2011**, *1*, 184-187.

[14] R. Pandey, A. A. Gunawan, K. A. Mkhoyan, and R. J. Holmes, "Efficient organic photovoltaic cells based on nanocrystalline mixtures of boron subphthalocyanine chloride and C_{60}", *Adv. Funct. Mater.* **2012**, *22*, 617-624.

[15] B. O'Connor, "Organic Electronics on Fibers for Energy Conversion Applications", University of Michigan, Ann Arbor. *Thesis*, **2009.**

[16] Y. Shao, Y. Yang, "Efficient organic heterojunction photovoltaic cells based on triplet materials", *Advanced Materials*, **2005**, *17*(23), 2841.

[17] P. Peumans, S.R. Forrest, "Separation of geminate charge-pairs at donor- acceptor interfaces in disordered solids", *Chemical Physics Letters*, **2004**, *398*(1-3), 27- 31.

[18] A. L. Fahrenbruch, J. Aranovich, *Solar Energy Conversion*s - *Solid-State Physics Aspects*; Springer-Verlag: Berlin, Heidelberg, New York, **1979**; Vol. 31.

[19] N. C. Giebink, B. E. Lassiter, G. P. Wiederrecht, M. R. Wasielewski, and S. R. Forrest, "Ideal diode equation for organic heterojunctions. I. Derivation and application", *Phys. Rev. B*, **2010**, *82*, 155306.

[20] M. D. Perez, C. Borek, S. R. Forrest, and M. E. Thompson, "Molecular and Morphological Influences on the Open Circuit Voltages of Organic Photovoltaic Devices", *J. Am. Chem. Soc.* **2009**, *131*, 9281

[21] Y. Yi, P. E. Jeon, H. Lee, K.l Han, H. S. Kim, K. Jeong and S. W. Cho, "The interface state assisted charge transport at the MoO_3/metal interface", *J. Chem. Phys*. **2009**, *130*, 094704-1-3.

[22] K. L. Mutolo, E. I. Mayo, B. P. Rand, S. R. Forrest, and M. E. Thompson, "Enhanced Open-Circuit Voltage in Subphthalocyanine/C60 Organic Photovoltaic Cells", *J. Am. Chem. Soc.*, **2006**, *128*, 8108-8109.

[23] H. Gommans, D. Cheyns, T. Aernouts, C. Girotto, J. Poortmans, and P. Hermans, "Electro-Optical Study of Subphthalocyanine in a Bilayer Organic Solar Cell", *Adv. Funct. Mate*r. **2007**, *17*, 2653-2658.

[24] P. Peumans, A. Yakimov, and S. R. Forrest, "Small molecular weight organic thin-film photodetectors and solar cells", *J. Appl. Phys.*, **2003**, *93*, 3693-3723.

[25] D. H. Levy, S. F. Nelson, and D. Freeman, "Oxide Electronics by Spatial Atomic Layer Deposition", *J. Display. Technol.*, **2009**, *5*, 484-494.

[26] Y. Sun, M. Shtein, and S. R. Forrest, "Direct patterning of organic light-emitting devices by organic-vapor jet printing", *Appl. Phys. Lett.* **2005**, *89*, 113504-1-4

[27] G. Wei, R. R. Lunt, K. Sun, S. Wang, M. E. Thompson, and S. R. Forrest, "Efficient, Ordered Bulk Heterojunction Nanocrystalline Solar Cells by Annealing of Ultrathin Squaraine Thin Films", *Nano Lett*. **2010,** *10*, 3555-3559.

[28] S. Ryuzaki, T. Kai, Y. Toda, S. Adachi and J. Onoe, "Effects of inter-molecular charge-transfer excitons on the external quantum efficiency of zinc- porphyrin/C60 heterojunction photovoltaic cells", *J. Phys. D*: *Appl. Phys.* **2011**, *44*, 145103-1.

[29] C.-T. Chou, W.-L. Tang, Y. Tai, C.-H. Lin, C. J. Liu, L.-C. Chen, K.-H. Chen, "Effect of substrate temperature on orientation of subphthalocyanine molecule in

organic photovoltaic cells", *Thin Solid Films*, **2012**, *520*, 2289–2292.

[30] P. Fenter, F. Schreiber, L. Zhou, P. Eiseberger, and S. R. Forrest, "*In situ* studies of morphology, strain, and growth modes of a molecular organic thin film", *Phys. Rev. B*, **1997**, *56*, 3046-3053.

[31] S. Biswas, K.A. Luck, M. Shtein, "Morphology control of air-deposited inverted organic photovoltaic devices", **2014**, (*in preparation*).

[32] S.E. Morris, *et al*., **2014**, (*in preparation*).

[33] I. Hancox, P. Sullivan, K.V. Chauhan, N. Beaumont, L.A. Rochford, R.A. Hatton, T.S. Jones, "The effect of a MoO_x hole-extracting layer on the performance of organic photovoltaic cells based on small molecule planar heterojunctions", *Org. Elec*., **2010**, ***11*** 2019.

[34] N. Wang, J. Yu, Y. Zang, J. Huang, Y. Jiang, "Effect of buffer layers on the performance of organic photovoltaic cells based on copper phthalocyanine and C_{60}", *Solar Energy Materials & Solar Cells* **2010**, *94*, 263–266.

CHAPTER 5

Fabrication of OTFTs by GF-OVJP

5.1. Requirements for OTFT active materials deposition

Increasingly, the development and application of functional materials aims to predict the structure and properties of materials prior to synthesis or processing. [1] While well-developed in metallurgy, polymer synthesis and, to some extent, in silicon processing, relatively little predictive ability exists in the rapidly growing field of organic semiconductors, [2, 3] due to the relative novelty of the materials and corresponding processing methods. This chapter aims to address this knowledge gap.

Interest in organic-based electronic and optoelectronic devices continues to grow, accompanied by improvements in device performance, [4, 5] accompanied by commercialization efforts. In particular, organic field effect transistors using conjugated oligoacenes (e.g. pentacene) [6] have exhibited robust performance characteristics, while offering low material cost, low-temperature processing, and compatibility with flexible substrates as advantages for a variety of applications. [7 – 9]

The properties of one archetypal oligoacene–pentacene–have been studied extensively. [6, 9 – 18] The electronic characteristics of pentacene films depend on purity, molecular ordering and film morphology, [6-10] which are in turn affected by process conditions. Pentacene films exhibit polymorphism, which has been extensively studied with respect to their structure, structure-process and structure-property relationships. [11, 12] The films are typically polycrystalline, and it is generally believed that carrier transport improves in films exhibiting well-ordered domains, and in channels with fewest grain boundaries. [13, 14] Many attempts have been made to improve carrier transport in the films by increasing grain size [15] or reducing the channel length to approach the size of individual grains. [16] Additionally, improvements in electronic performance characteristics have been realized *via* material purification, [6] and substrate modification at the interface between the organic semiconductor and the gate dielectric, [14, 17, 18] and/or between the organic semiconductor and the source / drain contacts. [19]

Concomitant with the development of materials and device architectures, there has been considerable effort underway to develop better processing methods. Specifically, there is interest in realizing solvent-free deposition and patterning, to minimize unintentional doping of the organic semiconductor by residual solvent, and to reduce process complexity, while minimizing environmental impact. Ideally, the desired semiconductor channel pattern could be generated rapidly in a single step, at ambient conditions, directly on the substrate of interest, with minimal material waste. None of the solvent-free deposition methods reported to date (including VTE, [20] OVPD, [21] flash evaporation, [22] LITI, [23] early variants of molecular jet printing, [24] and organic vapor jet printing [25,26]) satisfy fully these desired criteria. Molecular jet printing and OVJP enable additive patterning without the use of shadow masks. Guard flow-enhanced OVJP enables further control over the deposited film crystallinity, [27] and can be modified to enable deposition in air. This work tightly links process conditions with film morhpology measured by *in situ* and *ex situ* synchrotron x-ray diffraction, and quantitatively links process conditions and morphology to the film's performance in a TFT, which are the focus of this chapter and has been published by Biswas *et al*., (2014). [28]

5.2. Growth of pentacene by GF-OVJP

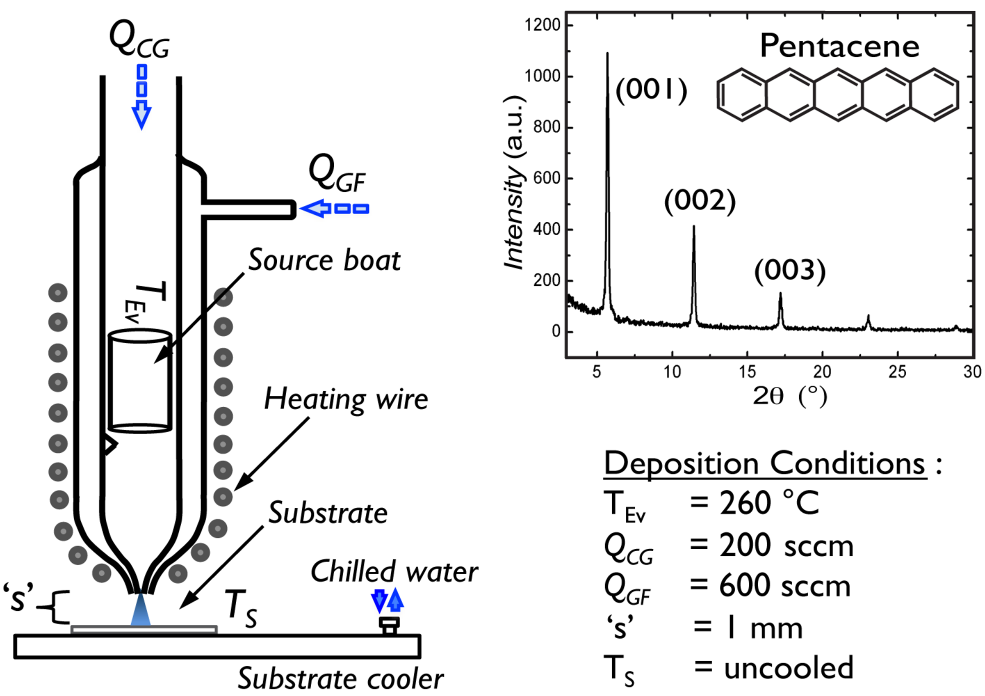

Figure 5-1. Schematic of the GF-OVJP apparatus, indicating the independently variable processing parameters, along with the particular values of these parameters used for pentacene deposition. Bragg peaks of a 60 nm thick pentacene film deposited in air by GF-OVJP. The 001 peak measured at 2θ = 5.7° using a Cu-Kα source indicated the deposit is in thin film phase with a lattice spacing of 1.54 nm. [28]

In OVJP, the organic semiconductor is evaporated into a stream of inert carrier gas, jetted from a nozzle at high velocity onto a cold substrate, where the organic material selectively condenses. Flow and material parameters, apparatus dimensions, and carrier gas determine the resolution of the deposited pattern. When depositing in air, oxygen and moisture from the ambient can be expected to diffuse into the periphery of the vapor jet and potentially modify the properties of the deposited film. In Alq_3 deposition, for example, the effects of oxidation have been well studied. [29] To minimize oxidation, the organic-containing jet can be surrounded by a guard jet of inert gas. The shielding and hydrodynamic focusing effects of the latter in guard flow-enhanced OVJP (GF-OVJP) growth of Alq_3 have been studied, [30] but no report was given with respect to morphological changes with guard flow rate. A subsequent study on the GF-OVJP growth of subphthalocyanine chloride (SubPc) for organic photovoltaic device applications revealed that film morphology can be affected greatly by the guard flow, potentially enhancing cross-plane carrier transport / exciton and photovoltaic device performance, [27] although no report was given regarding effects on in-plane transport.

On the one hand, in the above-mentioned initial studies of GF-OVJP intriguing processing advantages were introduced, including solvent free, rapid, direct, additive, single-step active layer patterning, scalability to large area substrates, no need for drying/annealing steps to obtain desired morphology, ability to deposit multilayered and mixed layers structures, high material utilization efficiency, and ability to grow device-quality films in air. On the other hand, to realize these possibilities, several important questions should be addressed, including: when depositing in air, how much oxygen and moisture is incorporated into the film? What effect/interplay exists between the degree of air exposure, molecular flux, flow conditions, morphology of the deposited film and the resulting device performance? Answering these questions is the basis for studying the deposition technique in detail and doing morphology and structure characterization coupled with flow dynamics simulation and TFT measurements.

In this study, pentacene thin films are grown by GF-OVJP, while studying the morphology based on location within the deposit using *ex situ* synchrotron x-ray diffraction (XRD); subsequently the electronic properties of the films are characterized and correlated with the deposition conditions and film morphology. As a result of these detailed studies, an analytical expression is proposed for the expected in-plane charge mobility in an organic semiconductor film deposited in air by GF-OVJP when rastering the jet over the substrate for large area applications.

5.2.1. Processing parameters and GF-OVJP capabilities

The deposition apparatus (**Figure 5-1**) consists of two cylindrical, concentric nozzles for the carrier gas and guard flow jets. The annular channel is angled at 15° from the nozzle axis, shielding and focusing the inner nozzle jet. The process parameters include: nozzle-substrate separation, s, evaporation (sublimation) zone temperature, T_{Ev}, substrate temperature, T_S, carrier gas flow rate, Q_{CG} and guard flow rate, Q_{GF}. Pentacene powder is loaded in the sublimation zone and heated to T_{Ev} while Q_{CG} and Q_{GF} are held constant. Processing conditions are detailed further in the experimental section. When all upstream conditions, including T_{Ev}, T_S, Q_{CG} and Q_{GF} are fixed, the organic vapor flux exiting the nozzle is constant, proportional to the vapor pressure [31] and has cylindrical symmetry. When the nozzle and substrate are stationary relative to each other, at a given value of s, a '*spot deposit*' is obtained which has a bell-shaped cross-sectional profile as shown in **Figure 5-2**, with the feature thickness of the spot being determined by the nozzle dwell time, as verified by optical interferometry [32] (**Appendix A**) and FLUENT 6.3.26 hydrodynamic simulations (details in **Ch. 3**). The profiles of deposits of different thickness (i.e. different nozzle dwell time) have the exact same shape, and all plots of the profiles are normalized to unity.

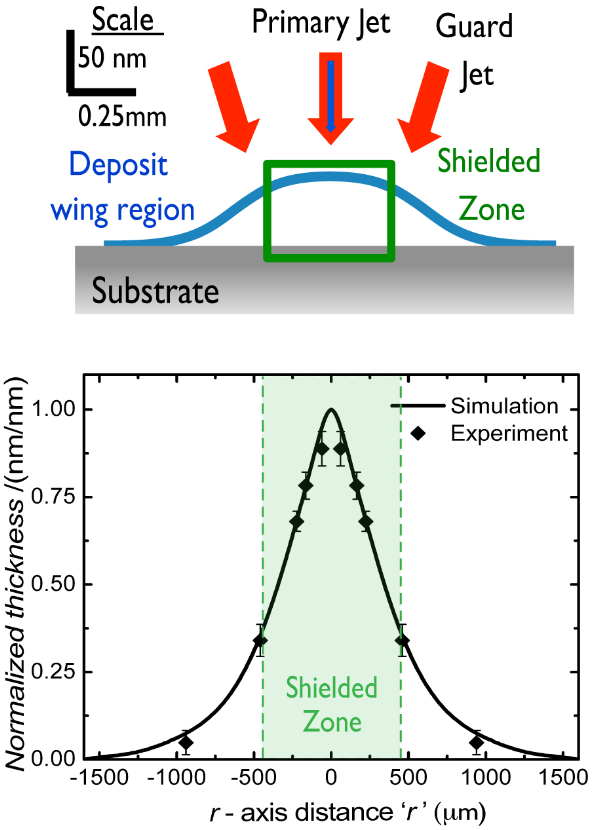

Figure 5-2. Qualitative cross-section (not to scale) of a typical deposition profile, with the central region of the deposit being shielded from ambient oxygen and moisture by the inert guard flow jet. (top) GF-OVJP deposits have the same general shape and can be normalized to the profile shown (bottom). This cross-sectional shape is validated by fluid dynamic simulations and by optical interferometric measurements on the deposits. [28]

Moving the nozzle relative to the substrate at a speed *v*, '*line deposits*' are obtained. Line thicknesses obtained by translating the nozzle are linearly proportional to 1/*v*. The thickness of the line deposit is uniform in the direction of motion, while the cross-section thickness profile in the direction perpendicular to motion remains that of a spot deposit. The radial axis in spot deposits and the direction perpendicular to the nozzle translation axis are collinear, denoted as the ***r***-axis throughout the text. Similarly, the direction of nozzle motion is denoted as the ***x***-axis. Moving the nozzle in multiple passes in a single line can increase the overall deposit thickness; for example, a 60 nm feature center thickness can be obtained by 4 passes of the nozzle, with each pass contributing 15 nm to the overall feature height. Note that these "stack" deposits are expected to exhibit different device properties from deposits of the same thickness grown in a single pass, because a "stack" deposit grown in multiple passes is exposed to air a number of times as the nozzle moves back and forth, resulting in a regrowth condition. Rastering the nozzle to draw multiple parallel, adjacent lines with sufficiently narrow line spacing (e.g. 0.1 mm) allow the deposit profiles to overlap and form one "large area deposit" with uniform thickness throughout. [33] **Figure 5-3** schematically depicts the types of deposits described above. In this work, all four types of deposits are used to fully characterize how processing affects the thin film morphology and associated device performance. To fabricate a top (source/drain) contact TFT on a spot deposit, gold source and drain electrodes can be prepared by VTE through a precisely placed shadow mask. For line deposits, gold contacts can be deposited with the channel width parallel to the direction of motion and hence measure electronic transport across a uniform thickness of film.

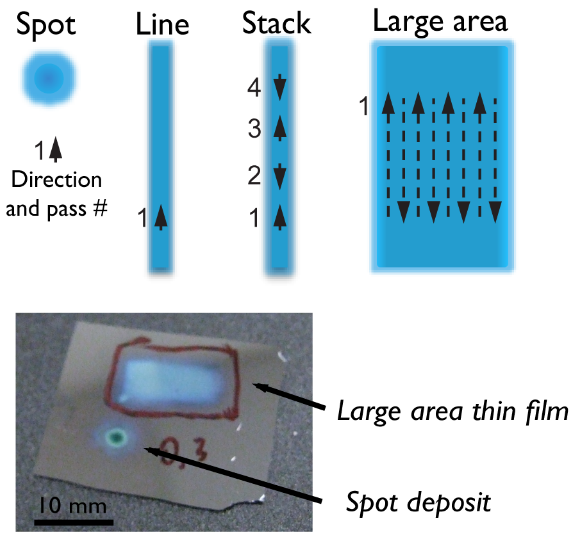

Figure 5-3. Top view of different deposit types obtainable by GF-OVJP by varying the nozzle's translational velocity, number of passes and direction of motion. Photograph of an actual sample with pentacene 'spot' and 'large area' deposits is also provided. [28]

The growth of pentacene in air by GF-OVJP is used to develop a structure – property – process relationship. A stepwise approach is adopted to establish this relationship of controlled air exposure on the film properties. First, the effect of deposition in air on the polycrystalline morphology of the grown films is analyzed. Then, the electronic properties of thin-film pentacene grown in air and in a nitrogen-purged glovebox by GF-OVJP is studied and compared to TFTs fabricated by VTE. Finally, the degradation of organic thin films due to oxygen and moisture exposure during deposition is isolated, and a simple analytical expression predicting the field-effect mobility of a large-area deposit formed in air by GF-OVJP is formulated.

5.3. Molecular ordering and air exposure

In GF-OVJP, the dependence of the deposited thickness on the local molecular flux at the substrate and nozzle translation velocity is non-trivial. In this experiment, the nozzle geometry is held constant and so is the net flux of molecules exiting the nozzle. As mentioned previously, for line deposits, the ***r***-axis is the direction perpendicular to nozzle translation direction, ***x***. **Figure 5-2** shows that the thickness and molecular flux cross-sectional profile vary in the ***r***-axis direction. For a given point along the ***r***-axis, the thickness of the material after a single pass of the nozzle (t_{pass}/nm) depends inversely on the nozzle translation velocity, v. The two parameters of interest are the molecular flux (varying along ***r***-axis) and the nozzle translational velocity, v (which can be varied along the translation direction); they need to be deconvoluted to examine their effects on the film crystallinity.

First, the effect of v on the crystallinity of the deposit at $r = 0$ mm (center of the shielded zone) are studied, where the molecular flux is constant. Here, the film crystallinity depends primarily on thickness, which in-turn is controlled by v. This is discussed in the next section and the synchrotron XRD apparatus details are provided the **Section 5.6.3.** Next, the effect of the positional change on the molecular flux, and the associated t_{pass}, along the ***r***-axis ($r >> 0$) for a single pass of the nozzle translated at a particular value of v is analyzed. In this case, the crystallinity is affected not only by the thickness but also by increasing exposure to air along the ***r***-axis. This effect is discussed in **Section 5.3.2**.

5.3.1. Effect of nozzle velocity on film crystallinity

Any desired deposited feature thickness can be attained either by growing the film at some value of v in one pass, i.e. continuous film growth, or at a higher v in multiple passes, i.e. intermittent film growth. An important question is: will the crystallinity of the deposited film be identical in the two approaches?

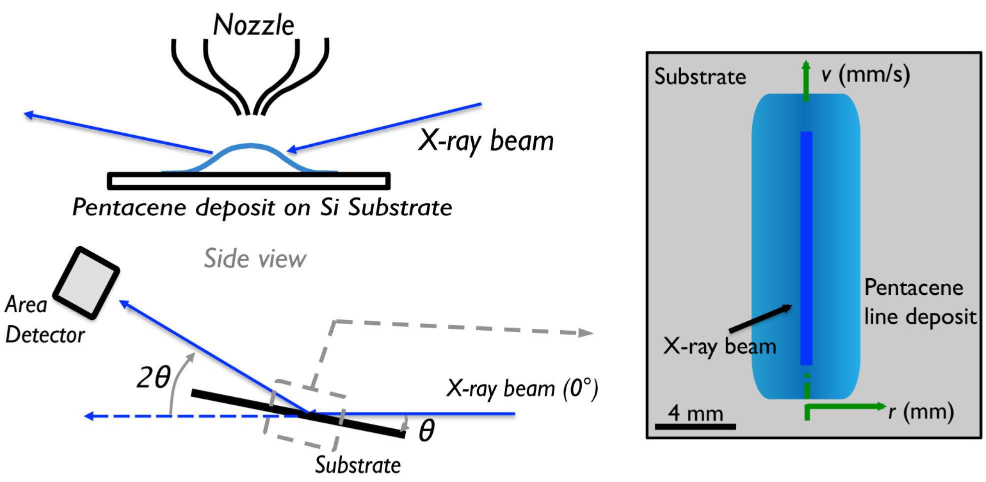

Figure 5-4. Schematic of the synchrotron based XRD experimental set up for *ex situ* θ-2θ measurements. (left) GF-OVJP line deposits with X-ray beam incident at the center of the line profile ($r = 0$ mm) (right).

To address this question, *ex situ* synchrotron x-ray diffraction experiments were performed on the films grown with various numbers of passes for several nozzle velocities (v), while looking at film only at $r = 0$ mm of the line deposit. A schematic of the synchrotron based XRD experimental set up is shown in **Fig. 5-4.** Structural studies of organic thin films deposited in air using x-ray diffraction were carried out at the National Synchrotron Light Source, Brookhaven National Laboratory. The diffraction signal shapes were recorded by a Pilatus 100K area detector. **Figure 5-5** shows the intensity at the position of the 001 pentacene film Bragg peak ($I_{r=0}$). Four solid lines are shown, with each line representing a particular v. For each v, different film thicknesses along the corresponding line are obtained by varying the number of passes, with the first point representing a single pass.

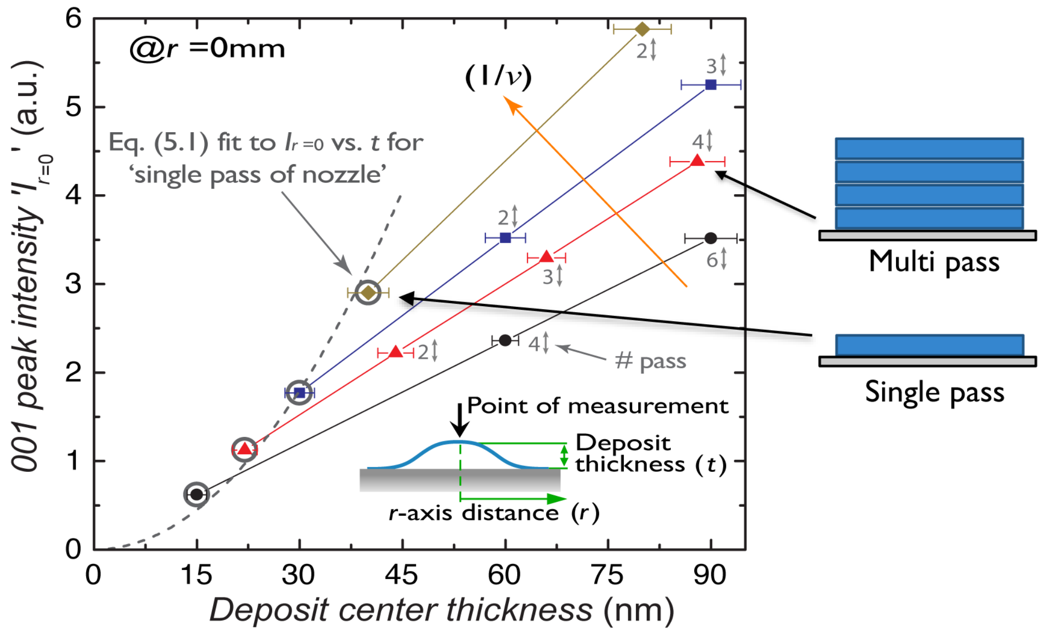

Figure 5-5. Diffraction intensity at the 001 Bragg peak position is plotted as a function of film thickness (at $r = 0$ mm). The dashed line is a quadratic fit of the intensity measured for films deposited by a single pass of the nozzle (marked with ○). Each solid line corresponds to a particular nozzle translation velocity, v, and different data points on each line are obtained by multiple passes (numerical indicates the number of passes) of the nozzle at each v. [28]

As typical for single crystal films, the diffraction intensity at the Bragg peak position increases as a quadratic function of thickness, because the diffracted waves add up coherently. This is derived from the Laue equation. [34] In **Figure 5-5**, the first data points on each solid line, with least thickness (marked with ○), represent the diffraction intensity from the films deposited with a single pass for each v. These data points fit well with the quadratic model (dashed curve). Since these films were grown continuously by a single pass of the nozzle, most of the film would crystallize simultaneously and form a continuous, stacked crystal (defined here as 'coherent' crystal), which explains the quadratic behavior, given by the equation

$$I_{r=0} = 0.0019 \bullet (t_{pass})^2 \tag{5.1}$$

Multiple pass deposition, however, shows a significantly different behavior. As the film thickness is increased by multiple passes of the nozzle at a particular value of *v*, the XRD peak intensity scales linearly with the thickness (solid lines, **Figure 5-5**). This indicates that the crystal layers grown by each pass are discontinuous in the out-of-plane direction forming multiple stacked layers of identical 'coherent' crystal structures with domain boundaries between the layers. From the standpoint of interaction with the x-rays, these layers diffract as separate crystallites, and the maximum intensities at the Bragg peak position add up linearly. Smaller values of *v* result in a thicker 'coherent' layer for each pass of the nozzle and thus yield a larger slope of the solid line in **Fig. 5-5**. This suggests that the films having identical thickness can have significantly different crystallinity, depending on the relative nozzle-substrate motion speed: low *v* in one pass, or at relatively higher *v* in multiple passes. This feature is potentially useful, such as when attempting to deposit amorphous films (e.g. emission layers in OLEDs) or crystalline films (e.g. transport layers in OLEDs), depending on the desired functionality.

*5.3.2. Effect of location along **r**-axis on film crystallinity*

The design of the nozzle, or the required precision of pattern alignment, is informed by the potential variation of properties across the area of a deposit. When depositing films for TFT or OPV applications, greater crystallinity and purity are generally desirable. For a single pass of the nozzle at a given translation velocity (at any point along ***r***-

axis) the 001 Bragg peak intensity would scale only with thickness in the absence of ambient air, with the same quadratic relationship (**Equation 5.1** and **Figure 5-5**). However, this is not the observed behavior, potentially due to manner in which the guard-flow behaves near the jet's periphery, explored further below.

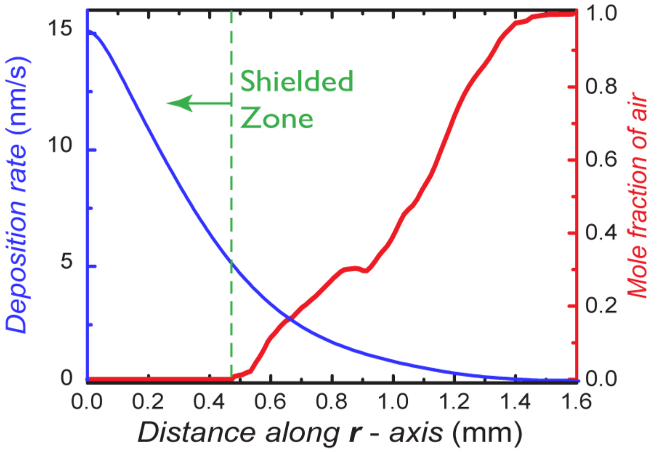

Figure 5-6. Plot of the simulated mole fraction of air interacting with the hot pentacene molecules during deposition as a function of ***r***. [28]

The jet velocity contours, temperature and pressure distribution, extent of air incorporation (**Fig. 5-6**), and other parameters can be quantified and understood using the fluid dynamics simulation of the GF-OVJP process. As shown in **Fig. 5-6** for the apparatus geometry used here, the shielded zone provided by the guard flow jet extends to $r = 0.45$ mm out for the deposition conditions mentioned above. The "wing" of the deposit lies beyond the shielded zone ($0.45 < r < 1.8$ mm) and is essentially unprotected by the guard flow. Hence, some degradation in this "wing" is expected, since incorporation of oxygen and moisture into the film during deposition results in more defects, both chemical and crystallographic.

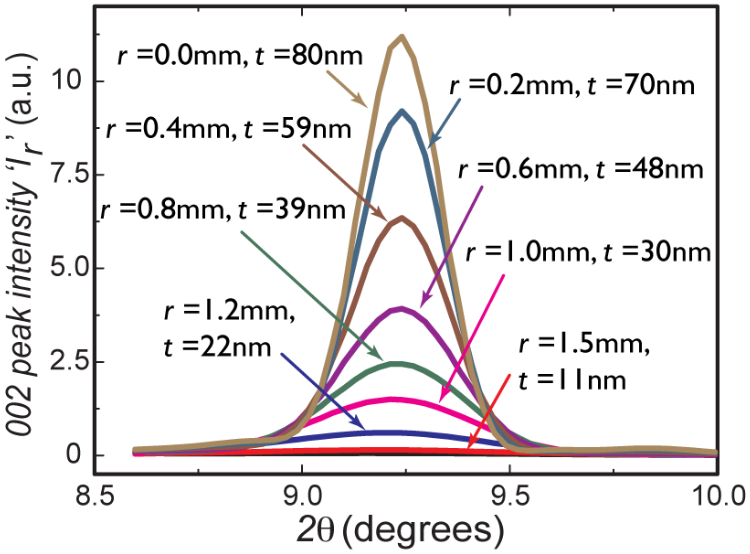

Figure 5-7. θ-2θ diffraction intensity, I_r, measurements around 002 peak for a line deposit, with feature center thickness of 80 nm, at different ***r***-axis locations (*r*) where the thickness is *t*. [28]

Here, the question is: how large of an effect will *greater air exposure* in the wings of the deposit have on the resulting film structure and properties, compared to when the film has minimal air exposure? This question is studied by looking at the diffraction intensity at different points along the ***r***-axis (**Fig. 5-7**). The intensities, however, cannot be directly compared to each other because both film thickness and air exposure change as a function of ***r*** and both can affect the peak intensity. To properly normalize the results, the diffraction data described in **Section 5.3.1** is employed as a reference. From **Eq. 5.1**, the Bragg peak intensity (denoted as $I_{r=0}$) of films deposited in a single pass with least air exposure (i.e. at $r = 0$ mm) can be calculated for any thickness. This provides a deterministic link between the process conditions and the film structure.

The Bragg intensity of the pentacene peak is measured along the ***r***-axis of a line deposit, denoted as I_r and plotted in **Fig. 5-7**. I_r was measured along the ***r***-axis during the synchrotron experiments. The thickness values at each of the locations are known (**Fig. 5-2**) and are labeled individually in **Fig. 5-7**. Based on this information, the measured film crystallinity via XRD in the "wing" region (**Fig. 5-7**), where moisture and oxygen in air can affect the crystallinity, can be quantitatively compared to the expected values for the shielded region ($r = 0$ mm) where the guard flow suppresses ambient exposure. (Note that the leading and trailing edges of the deposit at $r = 0$ mm along the translation axis experience some degree of air exposure, albeit, less than the wing region at large values of r.) This is important in properly deconvoluting the simultaneous contributions of growth rate dependent structural disorder and oxidation in the wings of the deposit to understand the practical limits of the patterning technique with regard to the desired film (and device) electronic properties. As can be observed from **Fig. 5-8**, the crystallinity of the film beyond the shielded zone ($r > 0.45$ mm) is reduced. An empirical curve is fit to the data and has a functional form of:

$$I_r / I_{r=0} = \mathrm{A}_1 + (\mathrm{A}_2 - \mathrm{A}_1)/(1+(r/r_a)^p) \qquad (5.2)$$

where A_1, A_2 and p are fitting constants, r_a is the point of inflection. r_a is affected by the nozzle geometry and the molecular flux distribution, while p is mostly affected by the turbulent diffusion of air molecules (due to turbulent mixing of guard flow jet and ambient air) and the propensity of the semiconductor material to oxidize, [39] although more detailed studies are needed to quantify these relationships. For the fit shown in **Figure 5-**

8, $r_a = 0.71 \pm 0.04$ mm and $p = 3.73 \pm 0.39$. This process-morphology relationship along the ***r***-axis can be further extended to include electronic properties of the films, as discussed in **Section 5.4.2**.

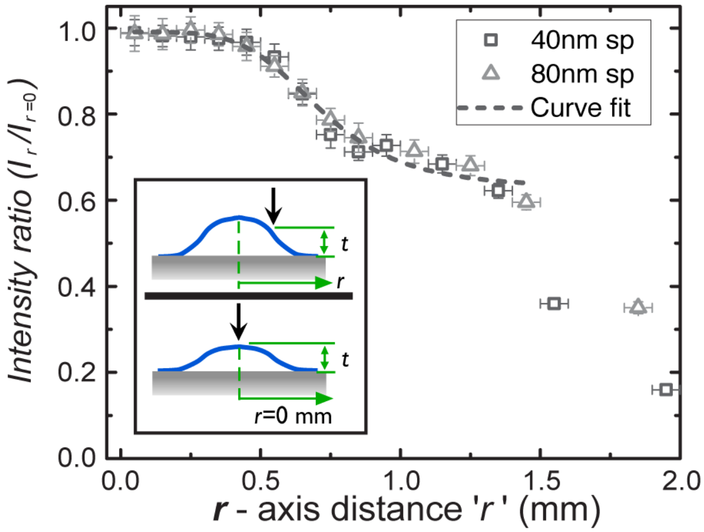

Figure 5-8. Ratio of I_r to $I_{r=0}$: I_r [measured intensities at 002 peak position: peak intensities given in **(Fig. 5-7)**] and $I_{r=0}$, [calculated for corresponding thickness from **Eq. 5.1**] are plotted for 40 nm and 80 nm feature center thickness. Dashed line is a curve fit to the data with **Eq. 5.2**. [28]

Note that for $r > 1.5$ mm, where films are less than 12 nm thick, **Equation 5.2** is invalid, due to a significant proportion of the very thin film having molecules with pentacene backbone axis parallel to the substrate, and the out of plane tilt angle being 28°, corresponding to a smaller lattice spacing than observed for thin-film phase. [35,36]

5.4. OTFTs performance and air exposure

Thin film transistors are fabricated with pentacene deposited in air by GF-OVJP at settings detailed in the Experimental section. The channel thickness is denoted by t, and its length (L) and width (W) are 50 µm and 1 mm, respectively. The device cross-section is shown schematically in **Figure 5-9a**.

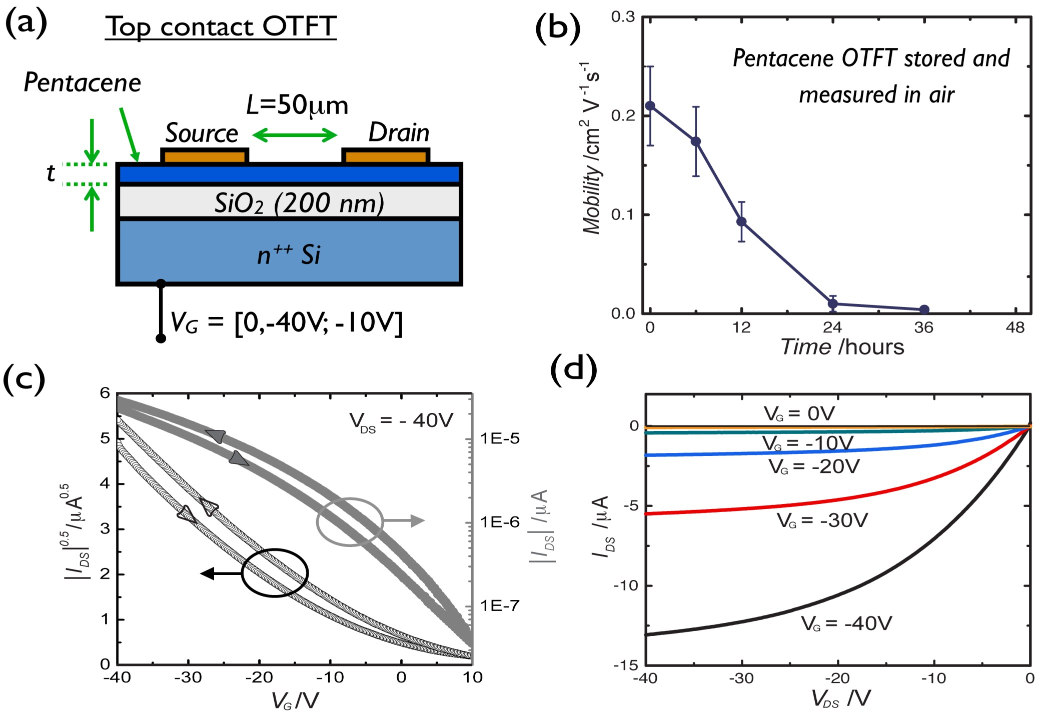

Figure 5-9. OTFT device structure and characteristics: **(a)** Schematic of a top contact pentacene TFT, fabricated on an n-type silicon wafer with a pre-deposited 200 nm SiO$_2$ gate dielectric. Pentacene film is deposited by GF-OVJP and source and drain electrodes are evaporated on top of the film using a shadow mask. **(b)** Post deposition air exposure due to storage in ambient leads to degradation of pentacene films. The lifetime of the devices fabricated is less than 48 hours after oxygen and moisture exposure. **(c, d)** show standard current-voltage characteristics of GF-OVJP transistors, with $t = 50$ nm. [28]

Control devices were deposited by VTE, as well as by GF-OVJP in a nitrogen-purged glovebox. Films of thickness between 15 nm and 80 nm were deposited in VTE at a deposition rate of 0.05 nm/s. The in-plane, field-effect hole mobility was found to be highest between 25 and 35 nm film thickness. [37,38] The post-deposition degradation (**Figure**

5-9b) due to ambient exposure is gradual and minimal in comparison to the drop in TFT characteristics due to exposure during deposition. When stored in air, the films degrade in time, as plotted for *t* = 40 nm deposited by VTE in **Fig. 5-9b**. This is suspected to be due to reaction of pentacene with ambient oxygen and moisture resulting in the formation of endoperoxide, giving rise to trap states in the electronic gap and hydroxyl impurities, [39] which distort the crystallinity of the thin-film. **Figure 5-10** shows some probable products resulting from the reaction of pentacene with ambient oxygen and moisture.

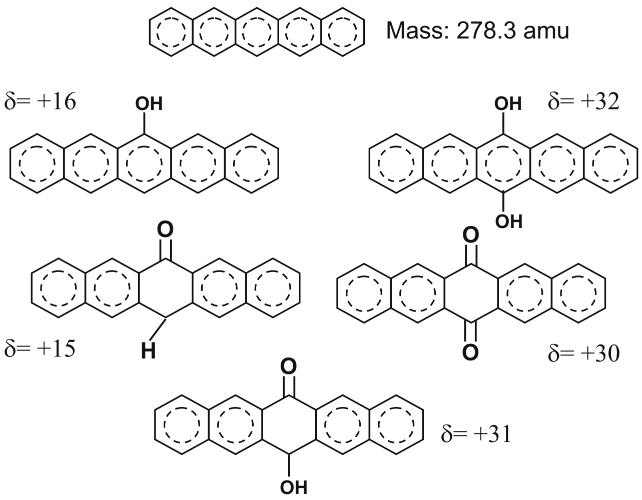

Figure 5-10. Probable molecules with multiple hydroxyl and carbonyl groups resulting from the reaction of pentacene with ambient oxygen and moisture. [39]

5.4.1. Effect of growth conditions on OTFTs characteristics

Pentacene channels grown by GF-OVJP in air exhibit the current-voltage characteristics shown in **Figure 5-9 c, d**; hole field-effect mobility (μ_{sat}), threshold voltage (V_T), sub-threshold slope (S) and On/Off ratio of current (On/Off) are all plotted in **Figure 5-11(a-d)** to show the comparison between air-deposited and glovebox-deposited pentacene films. It is expected that oxygen incorporation will be lowest in VTE-grown channels, while GF-OVJP of pentacene channels in the glovebox should result in comparable amount of oxidation to the VTE samples, but with enhanced molecular ordering and thus higher mobility.

Indeed, these trends are seen in in **Figure 5-11**. The μ_{sat} of the glovebox deposited channels is almost double that of the air-deposited devices and follows the same trend at the VTE deposited controls, with the highest $\mu_{sat} = 0.38$ cm^2 V^{-1} s^{-1} recorded at 40 nm maximum feature thickness. V_T also follows a similar trend, with the glovebox deposited films having a lower V_T than their air deposited counterparts. μ_{sat} and V_T are worse for the air deposited films due to the reaction of the hot organic vapor with oxygen in the periphery of the jet during deposition.

It is worth noting that μ_{sat} is 30% lower for in-air deposited than in-glovebox deposited TFTs due to ambient oxygen and moisture exposure of the pentancene molecules of the former *during deposition*. From **Figure 5-9b** at 30% drop in mobility is observed after drop is observed after 10 hours of storage in ambient of VTE films due to *post-deposition* air exposure. Exposure to ambient oxygen and moisture has a far greater effect on vapor phase pentacene molecules at elevated temperatures during deposition, than on post-deposited pentancene solid thin films. The On/Off current ratio of the glovebox deposited films is higher than that of the air deposited films due to a lower leakage current in the Off state. These results are consistent with the prevailing understanding of pentacene TFTs, where oxidation results in bulk traps that reduce μ_{sat}, while doping the film and elevating the Off current (more specifically, the formation of endoperoxides and hydroxyl variants of pentacene which disrupt the π-π cloud of pentacene and distort the crystallinity of the film, respectively) [39]. In the next section, the effect of pentacene degradation by these two mechanisms due to air exposure during deposition is analyzed.

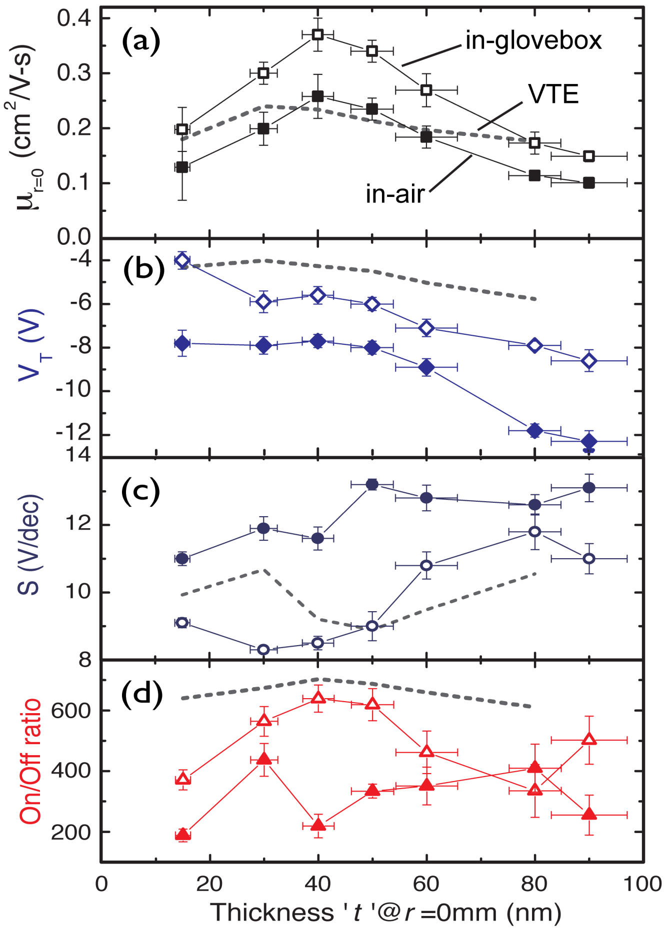

Figure 5-11. GF-OVJP deposited film characteristics: Filled symbols – In-air deposition; Open symbols – In-glovebox deposition; dashed grey line represents the TFT characteristics of VTE deposited films. Mobility, threshold voltage, sub-threshold slope and On/Off current ratio are measured at $r = 0$ mm. $\mu_{r=0}$, V_T peak around $t = 40$ nm. In-glovebox to in-air difference in TFT characteristics indicates structural and electronic defects in air-exposed pentacene thin films. [28]

*5.4.2. Effect of location along **r**-axis on electronic properties*

The local deposition rate of a line deposited by GF-OVJP varies with ***r***. **Figure 5-12** is a schematic of a line deposition process, showing the circular field of deposition area, along with the shielded zone and direction of deposition. From fluid dynamics simulation, the mole fraction of air at the boundary layer above the film as a function of ***r*** is found, shown in **Fig. 5-6**, allowing for a calculation of the net air exposure of the pentacene film as a function of *r*.

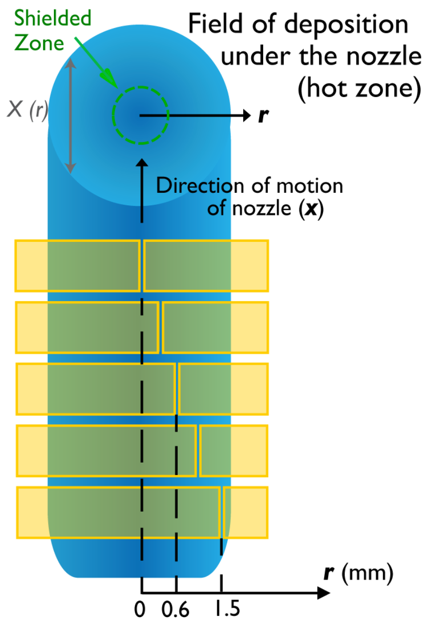

Figure 5-12. Top-view schematic of the transistor channel (source/drain gold contacts deposited by thermal evaporation through shadow masks, carefully aligned to center the channel along *r*); the channel thus contains material from both the shielded and the "wing" regions. [28]

When fabricating TFTs, 1 mm wide gold contacts are deposited on top of the film, with the 50 μm channel parallel to the ***x***-axis and centered at different values of ***r***. Creating channels in this fashion allows us to correlate TFT performance with known amounts of oxygen and moisture exposure. In the 'hot zone', at each value of ***r***, the total length of deposited pentacene molecules is X_r, as shown in **Fig. 5-12**. **Figure 5-13** shows the average fraction of oxygen and moisture molecules (denoted as $\bar{N}_r^{O_2\&H_2O}$) that interact with pentacene during deposition at each value of ***r***. This is obtained from the averaged weighted summation of the mole fraction of air along ***x***-axis in the 'hot zone' at each value of ***r*** (denoted as $n_r^{Air}(x)$) shown in **Fig. 5-6**, given by the equation:

$$\bar{N}_r^{O_2\&H_2O} = \frac{\int_{X_r} n_r^{Air}(x)\cdot\partial x}{\int_{X_r}\partial x}\cdot(0.21) \tag{5.3}$$

From **Equation 5.3**, it is calculated that at the center, $r = 0$ mm, 50% of the pentacene molecules are exposed to air in comparison to the regions of the substrate that lay outside the field of deposition, while at $r = 1$ mm the average air exposure increases to 65%. Since even the centrally-located material in a line deposit contains elements of the wing region from the leading and trailing edges of the jet, the total air exposure fraction of 50% is not surprising. Quantitatively, about 11% of all molecules (including N_2 from carrier gas, N_2 from air, O_2, H_2O, CO_2, etc.) colliding with the pentacene molecules during deposition in the hot zone, at $r = 0$ mm, are oxygen and moisture. Not all the oxygen and moisture interacting with pentacene molecules is incorporated into the deposited layer or reacts with hot organic vapor molecules to form chemical derivatives of pentacene. The values presented in **Fig. 5-13** (top) provide the absolute upper limit of defects/impurities in the deposited layer for the specific nozzle geometry and flow conditions used here.

To isolate the effect of ambient oxygen and moisture interaction with pentacene in the vapor and in the solid film during deposition, thin film transistors at r = 0, 0.4, 0.6, 1.0 and 1.5 mm from the center of the pentacene line deposits are fabricated, both in air and in the glovebox. The source and drain contacts are deposited through a shadow mask such that the channel width is aligned to the direction of nozzle motion, r away from the center, as shown in the **Figure 5-13** (bottom, inset). The only difference between μ_r and μ^G_r stems from the exposure of the air deposited samples to the ambient during deposition. The ratio of field-effect hole mobility values, measured in the saturation regime, for air deposited and glovebox deposited films, μ_r/μ^G_r, at the ***r***-axis distances mentioned above for peak line thickness of 15 nm to 90 nm is plotted in **Figure 5-13**.

$$\mu_r/\mu^G_r = A_4 + (A_4 - A_3)/(1+(r/r_a)^p) \qquad (5.4)$$

The dashed line fitted to the experimental data follows **Equation 5.4**, with $r_a = 0.76 \pm 0.05$ mm and $p = 3.45 \pm 0.51$. The trend seen in this plot of μ_r/μ^G_r *vs*. r is consistent with the results obtained for the ratio of diffraction intensity of crystallinity along r, plotted in **Fig. 5-8** and fit to **Equation 5.2**. This result is nearly identical to that in **Section 5.3.2** for fitting x-ray diffraction peaks along r, and implies that the predominant influence on pentacene *morphology* degradation in the wing region, as observed in **Figure 5-8**, comes from air exposure during deposition. The trend is also inversely proportional to the net air exposure of the film recorded in **Figure 5-13** (top). Hence, the degree of air exposure during deposition can be related to the film's morphology and electronic properties, recording a drop of 40 % for both the crystallinity and charge mobility with position away from the center of the deposit along the ***r**-axis*.

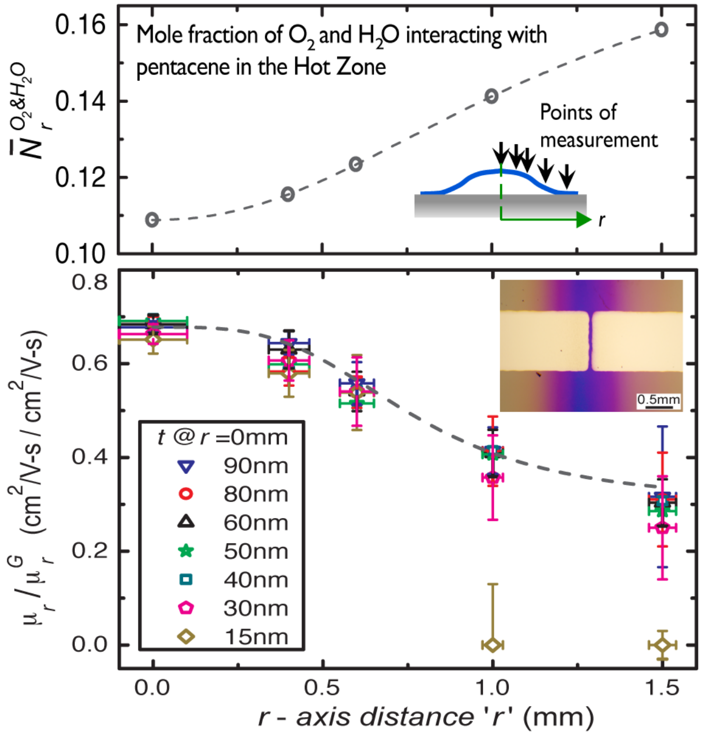

Figure 5-13. Mobility related to air exposure: The average mole fraction of oxygen and moisture that pentacene molecules interact with during deposition in the hot zone at each value of *r* is plotted. (top). The dashed line is a curve fit to the data. Plot of the ratio of mobility of the films deposited in air to those deposited in the glovebox. (bottom) The inset shows a micrograph of the TFT channel aligned on a line deposit. [28]

In principle, any pattern can be generated by translating the nozzle over the substrate along a predefined path. The process-structure-property relationship obtained from the above study can be extended to predict the performance of these complex patterns in devices, since this relationship is independent of the nozzle - substrate relative motion which is the primary parameter used for drawing patterns. For example, rastering the nozzle over the substrates enables us to grow large area deposits of uniform thickness, as shown in **Figure 5-2**. However, since the large area deposit thickness profile is an accumulation of thicknesses of line deposits uniformly spaced by 0.1 mm, the total thickness of the deposit is given by $T = t_{r=0} + 2\sum t_r$. For total thickness in the thin film regime, $T <$ 100 nm, the influence of air exposure on the electronic properties can be averaged for the large area deposit from the known dependence of μ_r vs. r of the line deposit. Thus the average mobility of a large area deposited in air by GF-OVJP can be estimated by:

$$\mu_T = \frac{\mu_{t,r=0} + 2\sum(\mu_r \cdot t)}{t_{r=0} + 2\sum t} \tag{5.5}$$

Using **Equation 5.5** and extracting $\mu_{r=0}$ and μ_r from **Figure 5-13**, μ_T (for T = 50 nm) is found to have a value of 0.21 cm^2/V-s. Remarkably, the field-effect mobility for a separately printed, large-area deposit of total thickness of 50 nm is measured to be 0.21 ± 0.06 cm^2/V-s, and falls within the confidence interval of the predicted value. Thus, the process-structure-property relationship shown herein can be extended to accurately predict the performance of pentacene thin films in any pattern deposited in air using GF-OVJP.

5.5. *In situ* characterization of GF-OVJP films

Molecular order resulting from a given set of processing conditions influences device performance, motivating *in situ* monitoring of growth processes. For example, Rolin *et al*. [40] used laser-induced fluorescence for accurate, real-time, *in situ* monitoring of the concentration of organic molecules in an OVPD chamber. The study showed how OVPD system design and operating conditions can be optimized to limit the duration of transport transients, which ultimately leads to precise control over the growth of complex, multi-layer thin-film structures. The GF-OVJP apparatus is compact and enables deposition of device-quality films in air, factors that potentially enable an even broader range of *in situ* characterization techniques that can be used to study the growth process. Recently, Biswas et al., and Shalev et al. [41, 42] studied thin-film growth mechanisms via *in situ* X-ray diffraction using a synchrotron source while growing pentacene and SubPc films in air using GF-OVJP. In this section, pentacene thin films are grown by GF-OVJP, while monitoring morphology evolution using *in situ* synchrotron x-ray diffraction is studied.

Pentacene is a highly desirable organic semiconductor for its application in low cost, flexible, lightweight, high mobility transistors, as a replacement for amorphous silicon. Pentacene thin films are known to have a thin film phase and bulk phase. [44] The thin film phase polymorph of pentacene is most commonly used in OTFTs, since it exhibits higher field-effect mobility than the bulk phase polymorph. However, the exact mechanism involved in the thin film polymorphic transformations in polycrystalline organic films is unclear. [45] It is important, therefore, to understand and characterize the morphology of pentacene during film growth.

Structural studies of organic thin films deposited in air using *in-situ* x-ray diffraction were carried out at the National Synchrotron Light Source, Brookhaven National Laboratory. Because the angular range of the diffractometer was highly limited by the *in-situ* growth setup, only a small part of the reciprocal space was accessible. Therefore, the x-ray measurement was focused only on the 001 peak of the pentacene film. The evolution of the film's crystallinity during film growth observed from the time-dependence of the diffraction signal shapes is detailed below (**Fig. 5-14**).

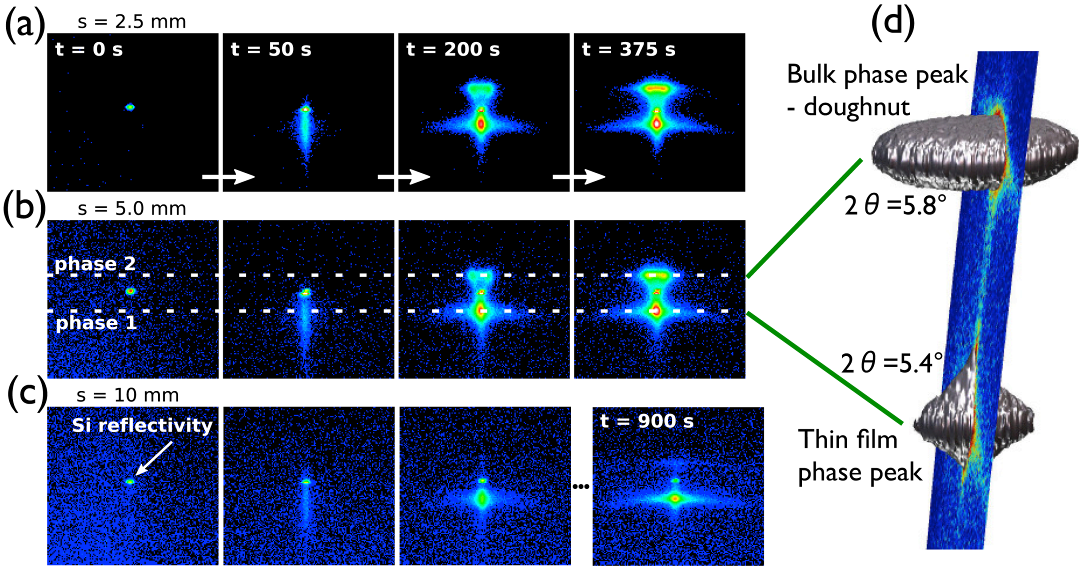

Figure 5-14. X-ray diffraction images of pentacene 001 thin-film and bulk phase peaks during the *in situ* growth, with the nozzle-substrate separation '*s*' distance **(a)** 2.5 mm **(b)** 5.0 mm **(c)** 10.0 mm. **(d)** 3D reconstructed reciprocal space intensity contour is presented showing both the thin-film and bulk phase peaks. [41]

Vapor deposited thin films of pentacene generally exhibit two polymorphs, a thin-film phase [43] and a bulk phase. [44] Although the bulk phase was observed to be a stable phase at around room temperature and starts to nucleate in the early stage of deposition, [45] most of the film initially grows in the thin film phase using GF-OVJP.

At the beginning of film growth, only the thin film phase peak [45, 46] appears (see **Fig. 5-14**, τ = 50 s). The peak is very elongated in the out-of-plane direction due to the limited thickness of the film. As the film grows thicker, the out-of-plane peak width becomes narrower, while the peak broadens in the in-plane direction. This broadening continues throughout the growth, eventually developing into a diffuse arc (**Fig. 5-14, Fig. 5-15a)**. The thin film phase peak is on the same vertical line as the Si reflection signal, indicating that the thin-film phase mainly grows with its crystallographic planes perpendicular to the substrate normal direction (**Fig. 5-15 c, d)**. This thin-film phase dominates for the first 80 nm of film thickness.

As the film deposition continues, the bulk phase peak appears (**Fig. 5-14**, $\tau = 200$ s, thickness = 80 nm). It initially splits into 2 sub-peaks, which do not lie on the vertical line containing the Si reflection and thin film phase peak, but are slightly offset to the left and right. This indicates that most of the bulk-phase film grows with its crystallographic planes slightly tilted away from the substrate normal direction (**Fig. 5-15a)**. With increasing film thickness, the split peaks become stronger and eventually coalesce into a single broad peak. In a 3-dimensional reciprocal space map (RSM) compiled at the end of the film growth (RSM: **Fig. 5-14d**), the bulk phase peak appears as an oblate spheroid. The detector images shown in **Fig. 5-14a-c** represent a single slice through this 3-dimensional volume, as indicated in **Fig. 5-14d**. The fact that the 3-dimensional RSM is symmetric around the out-of-plane direction indicates that there is no preferred in-plane orientation, but rather that within the illuminated spot size (~ 0.4 mm x 9 mm) of the x-ray beam, all tilt orientations are equally likely. This shows that the bulk phase portion of the pentacene film grown by GF-OVJP does not have any preferred in-plane orientation, and the diffraction signal is generated from a large number of crystallites with random in-plane orientations.

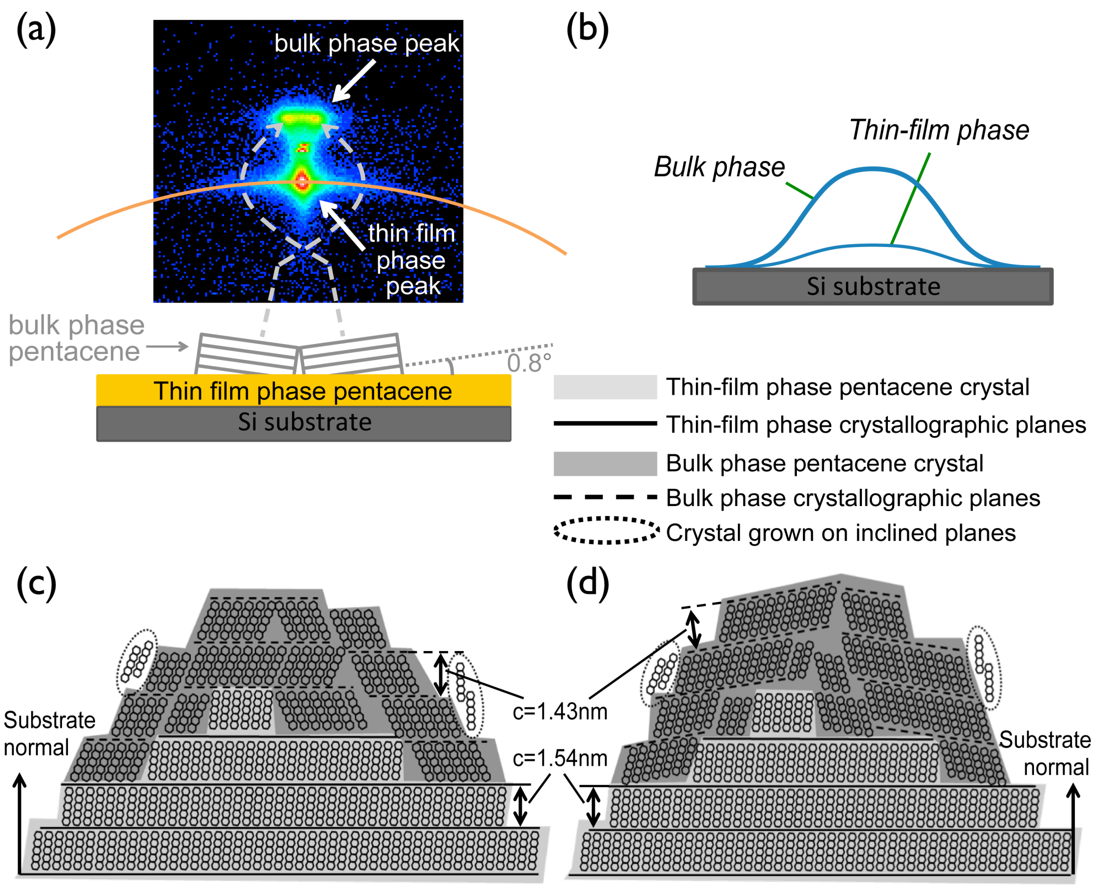

Figure 5-15. GF-OVJP grown pentacene shows bulk phase tilting: **(a)** From the spacing between the twin split bulk phase peaks, the tilt angle of bulk phase crystallographic plane is calculated to be 0.8°. Yellow curve is a guide to the eye for the diffuse arc-shape. **(b)** Schematic of bell-shaped film deposit. **(c)** A schematic of bulk phase crystal being grown with its crystallographic plane perpendicular to the substrate normal. **(d)** A schematic of bulk phase crystal being grown with its crystallographic plane tilted to the substrate normal. [41]

From the distance between the twofold split bulk phase peaks, the growth tilt angle is calculated to be approximately 0.8°. In many cases, this type of tilting can be explained by twinning effects, which are observed for some organic crystals, [47, 48] for example when there is a cleavage plane parallel to the substrate plane. However, due to the limited diffractometer movement for the *in situ* setup, the in-plane peaks were not accessible, hindering the indexing of the surface-parallel planes.

Most of the previous studies [49, 50] describe the pentacene film grown on SiO_2 with the model presented in **Fig. 5-15c**, in which both the thin-film-phase and the bulk-phase grow with their crystallographic planes parallel to those of the substrate. In this case, the bulk-phase peak would show up as a single peak on the same vertical line with the thin-film phase peak, and should not show any signs of splitting. However, a clear splitting in the initial growth stage is observed in the *in situ* XRD measurements, and therefore the crystallographic planes must be tilted with respect to the substrate, which is similar to the result reported by Moser *et al.* [51] and Watanabe *et al.* [52] for pentacene films grown on organic dielectric buffer layers. The model shown in **Fig. 5-15d** outlines the structural features of this phase, which appears to be unique to growth by a collimated jet in GF-OVJP. Two hypotheses are postulated here to explain the bulk phase tilt. One was suggested by Budai *et al.* for inorganic oxides growth on miscut steps of metal substrates, [53] and may apply to pentacene bulk phase growth on the sloping sides of bell-shaped deposits containing the thin film phase. Another hypothesis is that the out-of-plane tilt giving rise to the XRD pattern is due to a misalignment between a "herring-bone" molecular stacking motif of each layer that naturally leads to twinning. As the film growth proceeds, the accumulation of stacking faults will smear the definition of the orientation of tilt, giving the observed arc of scattering in **Fig. 5-15 a**,**b**. The tendency to fault is consistent with the fast deposition rate at high temperature, although further study to understand the phase behavior in detail exceeds the scope of this paper.

Figures 5-14(a-c) show that the peaks for both phases are very intense in the center, but are accompanied by very weak and diffuse rings around them that lie on an arc with a constant 2-theta angle. This proves that most of the film is very well ordered with the crystallographic planes (nearly) parallel to the substrate, but that a small fraction of slightly misoriented crystallites are present, giving rise to the faint arc. As shown by Cheng *et al.*, [54] crystallites grown on inclined planes are tilted relative to films grown on a flat surface. Following that study, it can be speculated that, because films grown with GF-OVJP spot deposition have bell-shaped cross-section (**Fig. 5-15b** schematic), the tilted crystallites may grow on the varying slope of the growth surface, and, as a result, the arc becomes continuous rather than being discrete. This would also explain why the initially two-fold split bulk phase peaks become broader and eventually connected to each other as the growth continues, also accompanied by the appearance of a diffuse arc.

5.6. Experimental details

5.6.1. GF-OVJP apparatus and deposition conditions

The GF-OVJP nozzle used in this study was constructed from two coaxial glass tubes of 0.5” and 0.75” outer diameters, fused at one end and pulled at the other to form concentric nozzle tips of 200 μm and 700 μm internal diameters. The inert carrier gas and evaporated organic vapor is transported through the inner tube. The annular channel for the guard jet was found to be 100 μm wide and angled at $\alpha \sim 15$ ° from the nozzle axis. The nozzle was cleaned with solvents, [30] dried and wrapped with 36-gauge heavy insulated tape heater (Omega Engineering, Inc.) with a power density of 8.6 W/in^2. The heating tape leads were connected to a temperature controller (Digi-Sense Benchtop temperature controller, Cole-Palmer Instruments Co.) and a 1/16" K-type thermocouple was used to maintain the temperature of the source. The source consisted of 0.15 g of pentacene powder (99% purity, Luminescence Technology Corp.) sandwiched between quartz wool and placed in the heated source section of the inner tube. The carrier gas and guard jet flow rates were maintained using mass flow controllers (C100 MFC, Sierra Instruments). The nozzle axis is held perpendicular to the substrate, and its motion is achieved by a computer-controlled X-Y-Z positioning stage (PT3-Z8 motorized translation stage, Thorlabs).

The process parameters, as shown in **Figure 5-1**, are nozzle-substrate separation, s, evaporation/sublimation zone temperature, T_{Ev}, substrate temperature, T_S, carrier gas flow rate, Q_{CG} and guard flow rate, Q_{GF}. Powdered pentacene is loaded in the sublimation zone and heated to $T_{Ev} = 260.0 \pm 0.5$ °C. T_S is maintained at room temperature while the Q_{CG}, Q_{GF} and s held constant at 200 sccm, 600 sccm and 1 mm respectively.

Note that '***r***' is defined as the distance from the center of the deposit in a radial direction. The relationship in Eq. **5.**2 and **Eq.** 4 are specific to the deposition profile shown in Figs. **5-2** and **5-6**. This profile is obtained for specific deposition parameter values. The deposition profile and '***r***' are a function of carrier gas nozzle radius (a_{CG}), guard flow nozzle radius (a_{GF}), angle of guard flow nozzle with respect to the axis (α) and the nozzle substrate spacing (s). '$r/\{a_{CG} + a_{GF} - s \cot(\alpha)\}$' would be good choice for non-dimensionalizing the radial distance parameter, in order to relate all the variable geometry parameters. Unfortunately, even these parameters remain inadequate for a full description, since Q_{CG} and Q_{GF} can also affect the deposition profile. Hence, at this stage, relating the Bragg peak intensity and mobility to '***r***' is sufficient for the discussion here.

5.6.2. Computational fluid dynamics modeling

To fully understand the hydrodynamic interaction of guard flow jet and the primary jet carrying organic vapor, and the subsequent film growth and incorporation of ambient air into film, a complete computational fluid-dynamic modeling by FLUENT 6.3.26 software is utilized. Using Navier–Stokes equations with a standard *k*-*ε* turbulence model in the software coupled with estimated fitting parameters, multicomponent diffusion and species transport describing organic vapor transport and adsorption, a full map of flow and species distribution characteristics were obtained. [27]

5.6.3. Synchrotron x-ray diffraction measurement set up

In situ and *ex situ* X-ray diffraction experiments were conducted at the beamline X21 (wiggler source) of the National Synchrotron Light Source (NSLS) at Brookhaven National Laboratory, and at the beamline 33-IDD (undulator source) of the Advanced Photon Source (APS) at Argonne National Laboratory. The data given in **Figures 5-5, 5-14, 5-15** were measured with 10.0 keV monochromatic x-ray beam at beamline X21 of NSLS. For the data given in **Fig. 5-7**, highly focused undulator beam (beam size~ 60μm × 60μm, 10 keV x-ray energy) at the beamline 33-IDD of APS was employed. For all measurements, standard θ-2θ scans were taken in the vertical scattering plane with a PILATUS 100K pixel detector. Pentacene films were grown using GF-OVJP in air on 5x5 cm^2 bare silicon substrates, which were cleaned as described below.

5.6.4. Pentacene thin film transistor fabrication and testing

Substrates used in this study were 2.5x2.5 cm^2 doped silicon wafers with a 200 nm thick oxide layer. These were cleaned by ultrasonication in detergent solution and deionized water followed by heated acetone, trichloroethylene, and isopropanol for 10 min each. Substrates were then placed in boiling isopropanol for 5 min, dried in pure nitrogen gas prior to pentacene film deposition. Control devices were fabricated with films deposited by thermal evaporation in a 10^{-6} torr vacuum chamber (Angstrom Engineering Inc.). Pentacene patterned by GF-OVJP was done in air and in an LC Technology Solutions Inc. glovebox purged with 99.99 % pure N_2. The gold source-drain electrodes were deposited on the patterned pentacene film surface by shadow mask evaporation. The channel had a thickness, t, with L = 50 μm and W = 1 mm. The channel was carefully aligned at the exact location along the ***r***-axis of the deposit using a Zeiss Axio Scope.A1 upright microscope. Five (5) transistors were fabricated on each pentacene line in order to obtain the error bars recorded in this work. The organic TFT electrical properties were tested in ambient using an Agilent 4156B semiconductor parameter analyzer.

5.7. Summary

To address a growing need to link process, structure, and properties in a predictive manner in the rapidly evolving area of organic semiconductors, pentacene thin-film deposition by GF-OVJP is examined in detail, which enables additive patterning at high throughput of electronic device-quality organic semiconductor thin films in air. The guard flow shields the organic vapor-rich jet from exposure to ambient oxygen and moisture up to a certain distance along the ***r***-axis. Outside this shielded zone, ambient air penetrates the boundary layer and interacts with the molecular film, disrupting its crystallinity and introducing trap states in the electronic band of the material. Rigorous gas dynamics simulation are used to calculate the mole fraction of air molecules in the region outside the shielded zone, and relate that to the degree of disruption to molecular order in the film obtained by synchrotron-based *in situ* and *ex situ* XRD and by analyzing field-effect mobility measurements. From these correlations, it is inferred that some incorporation of air occurs in the deposited film during growth, resulting in a 40 % drop in the crystallinity and field-effect mobility, which follow an identical trend across the radial axis. The interplay between defect incorporation, crystallinity and mobility is critical when printing complex patterns, as the effects of air exposure in the wings of the deposit profile have a cumulative effect on overall performance. This study conclusively shows that such effects can be accurately modeled for large area deposits, with the predicted field-effect mobility matching the measured values. These findings elucidate the relationship between deposition conditions, pattern dimensions, film morphology, and resulting device properties. They form a solid foundation for subsequent simulation-driven design of film deposition apparatus and process, in order to improve pattern resolution and device performance in organic electronics.

5.8. References

[1] National Science and Technology Council, Office of Science and Technology Policy, *Materials Genome Initiative for Global Competitiveness*, June **2011**

[2] S. R. Forrest, "The path to ubiquitous and low-cost organic electronic appliances on plastic", *Nature* **2004**, *428*, 911.

[3] S. Biswas, O. Shalev, M. Shtein, "Thin-Film Growth and Patterning Techniques for Small Molecular Organic Compounds Used in Optoelectronic Device Applications", *Annu. Rev. Chem. Biomol. Eng.* **2013**, *4*, 289.

[4] Y. S. Tyan, "Organic light-emitting-diode lighting overview", *J. Photonics Energy* **2011**, *1*, 011009.

[5] B.P. Rand, J. Genoe, P. Heremans, J. Poortmans, “Solar cells utilizing small molecular weight organic semiconductors”, *Prog. Photovolt.: Res. Appl.* **2007**, *15*, 659.

[6] M. Kitamura, Y. Arakawa, “Pentacene-based organic field-effect transistors”, *J. Phys.*: *Condens. Matter* **2008**, *20*, 184011.

[7] G. Horowitz, “Organic thin film transistors: from theory to real devices”, *J. Mater. Res.* **2004**, *19*, 1946.

[8] J. Smith, W. Zhang, R. Sougrat, K. Zhao, R. Li, D. Cha, A. Amassian, M. Heeney, I. McCulloch, T. D. Anthopoulos, “Solution-processed small molecule-polymer blend organic thin-film transistors with hole mobility greater than 5 cm^2/V-s”, *Adv. Mater.* **2012**, *24*, 2441.

[9] H. E. Katz, “Recent advances in semiconductor performance and printing processes for organic transistor-based electronics”, *Chem. Mater.* **2004**, *16*, 4748.

[10] D. J. Gundlach, Y. Y. Lin, T. N. Jackson, S. F. Nelson, D. G. Schlom, “Pentacene Organic Thin-Film Transistors - Molecular Ordering and Mobility”, *IEEE Electron Device Letters* **1997**, *18*, 87.

[11] C. C. Mattheus, G. A. de Wijs, R. A. de Groot, T. T. M. Palstra, “Modeling the Polymorphism of Pentacene”, *J. Am. Chem. Soc.*, **2003**, *125*, 6323.

[12] C. D. Dimitrakopoulos, P. R. L. Malenfant, “Organic thin film transistors for large area electronics”, *Adv. Mater.*, **2002**, *14*, 99.

[13] W.-Y. Chou, H.-L. Cheng, “An Orientation-Controlled Pentacene Film Aligned

by Photoaligned Polyimide for Organic Thin-Film Transistor Applications", *Adv. Funct. Mater.* **2004**, *14*, 811.

[14] M. Shtein, J. Mapel, J. B. Benzinger, S. R. Forrest, "Effects of film morphology and gate dielectric surface preparation on the electrical characteristics of organic-vapor-phase- deposited pentacene thin-film transistors", *Appl. Phys. Lett.* **2002**, *81*, 268.

[15] F. J. Meyer zu Heringdorf, M. C. Reuter, R. M. Tromp, "Growth dynamics of pentacene thin films",*Nature* **2001**, *412*, 517.

[16] B. Chwang, C. D. Frisbie, *J. Phys. Chem. B* **2000,** *104*, 12202.

[17] Y.-Y. Lin, D. J. Gundlach, S. F. Nelson, T. N. Jackson, "Pentacene-Based Organic Thin-film Transistors", *IEEE Trans. Electron Devices.* **1997**, *44*, 1325.

[18] S. Kobayashi, T. Nishikawa, T. Takenobu, S. Mori, T. Shimoda, T. Mitani, H. Shimotani, N. Yoshimoto, S. Ogawa, Y. Iwasa, "Control of carrier density by self-assembled monolayers in organic field-effect transistors", *Nat. Mater.* **2004**, *3*, 317.

[19] C.W. Chu, S.H. Li, C.W. Chen, V. Shrotriya, Y. Yang, "High-performance organic thin-film transistors with metal oxide/metal bilayer electrode", *Appl. Phys. Lett.* **2005**, *87*, 193508.

[20] J. Puigdollers, C. Voz, A. Orpella, I. Martin, M. Vetter, R. Alcubilla, "Pentacene thin-films obtained by thermal evaporation in high vacuum", *Thin Solid Films* **2003**, *427*, 367.

[21] M. Shtein, H. F. Gossenberger, J. B. Benzinger, S. R. Forrest, "Material transport

regimes and mechanisms for growth of molecular organic thin films using low-pressure organic vapor phase deposition", *J. Appl. Phys.* **2001**, *89*, 1470.

[22] C. Cali, V. Daneu, A. Orioli, S. Riva-Sanseverino, "Flash evaporation of compounds with a pulsed-discharge CO_2 laser" *Appl. Opt.* **1976**, *15*, 1327.

[23] J. Y. Lee, S. T. Lee, "Laser-Induced Thermal Imaging of Polymer Light-Emitting Materials on Poly(3,4-ethylenedioxythiophene): Silane Hole-TransportLayer", *Adv. Mater.* **2004**, *16*, 51.

[24] J. Chen, V. Leblanc, S. H. Kang, P. J. Benning, D. Schut, M. A. Baldo, M. A. Schmidt, V. Bulovic, "High Definition Digital Fabrication of Active Organic Devices by Molecular Jet Printing", *Adv. Funct. Mater.* **2007**, *17*, 2722.

[25] M. Shtein, P. Peumans, J. B. Benziger, S. R. Forrest, "Direct mask-free patterning of molecular organic semiconductors using organic vapor jet printing" *J. Appl. Phys.* **2004**, *96*, 4500.

[26] C. Yun, J. Choi, H. W. Kang, M. Kim, H. Moon, H. J. Sung, S. Yoo, "Digital-Mode Organic Vapor-Jet Printing (D-OVJP): Advanced Jet-on-Demand Control of Organic Thin-Film Deposition", *Adv. Mater*. **2012**, *24*, 2857.

[27] S. Biswas, K. A. Luck, M. Shtein, "Guard flow-enhanced organic vapor jet printing of photovoltaic donor materials in air", *Org. Electron.* **2012**, *13*, 2905.

[28] S. Biswas, Y. Yang, C. M. Schlepütz, N. Geva, R. L. Headrick, R. Pindak, R. Clarke and M. Shtein, "Spatial mapping of morphology and electronic properties of air-printed pentacene thin films", *Adv. Funct. Mater.*, **2014** (*accepted, in print*)

[29] H. Aziz, Z. Popovic, S. Xie, A.-M. Hor, N.-X. Hu, C. Tripp, G. Xu, "Humidity-

induced crystallization of tris (8-hydroxyquinoline) aluminum layers in organic light-emitting devices", *Appl. Phys. Lett.* **1998**, *72*, 756.

[30] S. Biswas, K. P. Pipe, M. Shtein, "Solvent-free, direct printing of organic semiconductors in atmosphere", *Appl. Phys. Lett.* **2010**, *96*, 263301.

[31] O. Shalev, M. Shtein, "Effect of crystal density on sublimation properties of molecular organic semiconductors", *Org. Electron.* **2013**, *14*, 94.

[32] M. Shtein, P. Peumans, J. B. Benziger, S. R. Forrest, "Micropatterning of small molecular weight organic semiconductor thin films using organic vapor phase deposition", *J. Appl. Phys.* **2003**, *93*, 4005.

[33] Y. R. Sun, M. Shtein, S. R. Forrest, "Direct patterning of organic light-emitting devices by organic-vapor jet printing", *Appl. Phys. Lett.* **2005**, *86*, 113504.

[34] B. E. Warren, *X-Ray Diffraction*, Dover Publications, Inc., New York, NY, USA, **1990**, Ch. 3.

[35] S. Söhnchen, S. Lukas, and G. Witte, "Epitaxial growth of pentacene films on Cu(110)", *J. Chem. Phys.* **2004**, *121*, 525.

[36] F. Zheng, B.-N. Park, S. Seo, P. G. Evans, F. J. Himpsel, "Orientation of pentacene molecules on SiO2: From a monolayer to the bulk", *J. Chem. Phys.* **2007**, *126*, 154702.

[37] R. Ruiz, A. Papadimitratos, A. C. Mayer, G. G. Malliaras, "Thickness dependence of mobility in pentacene thin-film transistors", *Adv. Mater*. **2005**, *17*, 1795.

[38] J. E. Northrup, M. L. Chabinyc, "Gap states in organic semiconductors: Hydrogen- and oxygen-induced states in pentacene", *Phys. Rev. B* **2003**, *68*, 041202.

[39] F. De Angelis, M. Gaspari, A. Procopio, G. Cuda, E. Di Fabrizio, "Direct mass

spectrometry investigation on Pentacene thin film oxidation upon exposure to air", *Chem. Phys. Lett.* **2009**, *468*, 193.

[40] T.C. Rolin, G. Vartanian, S. R. Forrest, "Laser induced fluorescence monitoring of the transport of small organic molecules in an organic vapor phase deposition system", *J. Appl. Phys.* **2012**, *112*, 113502.

[41] S. Biswas, Y. Yang, C. M. Schlepütz, R. L. Headrick, R. Pindak, R. Clarke and M. Shtein, "*In situ* characterization of pentacene films grown in air ", **2014** (*in preparation*)

[42] O. Shalev, S. Biswas, T. Eddir, Y. Yang, R. Clarke, M. Shtei. "In-situ study of growth behavior of boron subphthalocyanine chloride (SubPc) using guard flow-enhanced organic vapor jet printing" Presented at *Mater. Res. Soc. Conf.*, Nov. **2012**, Boston, MA.

[43] R. B. Campbell, J. M. Robertson, and J. Trotter, "The crystal structure of hexacene, and a revision of the crystallographic data for tetracene and pentacene", *Acta Crystallogr*. **1962**, *15*, 289.

[44] T. Kakudate, N. Yoshimoto, Y. Saito, "Polymorphism in pentacene thin films on SiO_2 substrate", *Appl. Phys. Lett.* **2007**, *90*, 081903.

[45] A. C. Mayer, A. Kazimirov, and G. G. Malliaras, "Dynamics of bimodal growth in pentacene thin films", *Phys. Rev. Lett*, **2006**, *97*, 105503.

[46] C. D. Dimitrakopoulos, A. R. Brown, A. Pomp, "Molecular beam deposited thin films of pentacene for organic field effect transistor applications", *J. Appl. Phys.* **1996**, *80*(4), 2501.

[47] M. Moret, M. Campione, A. Borghesi, L. Miozzo, A. Sassella, S. Trabattoni, B. Lotz, A. Thierry, "Structural characterization of single crystals and thin films of

α,ω-dihexylquaterthiophene", *J. Mater. Chem.* **2005**, *15*, 2444.

[48] R. Resel, H. Plank, A. Pogantsch, G. Leising, J. Keckes, "Twinning effects in polycrystalline hexaphenyl thin films", *Synth. Met.* **2001**, *121*, 1361.

[49] H. Yoshida, N. Sato, "Grazing-incidence x-ray diffraction study of pentacene thin films with the bulk phase structure", *Appl. Phys. Lett.* **2006**, *89*, 101919.

[50] D. Guo, S. Ikeda, K. Saiki, "Modified bimodal growth mechanism of pentacene thin films at elevated substrate temperatures", *J. Phys.: Condens. Matter* **2010**, *22*, 262001.

[51] A. Moser, H.G. Flesch, A. Neuhold, M. Marchl, S.J. Ausserlechner, M. Edler, T. Griesser, A. Haase, D.-M. Smilgies, J. Jakabovi, R. Resel, "Crystallization of pentacene thin films on polymeric dielectrics", *Synth. Met.* **2012**, *161*, 2598.

[52] T. Watanabe, T. Hosokai, T. Koganezawa, N. Yoshimoto, "*In situ* real-time x-ray diffraction during thin film growth of pentacene", *Mol. Cryst. Liq. Cryst.* **2012**, *566*, 18.

[53] J. D. Budai, W. Yang, N. Tamura, J. S. Chung, J. Z. Tischler, B.C. Larson, G. E. Ice, C. Park, D. P. Norton, "x-ray microdiffraction study of growth modes and crystallographic tilts in oxide films on metal substrates", *Nat. Mater.* **2003**, *2*, 487.

[54] H.-L. Cheng, Y.-S. Mai, W.-Y. Chou, L.-R. Chang, X.-W. Liang, "Thickness-dependent structural evolutions and growth models in relation to carrier transport properties in polycrystalline pentacene thin films", *Adv. Funct. Mater.* **2007**, *17*, 3639.

CHAPTER 6

Chemical Vapor Jet Deposition of Parylene

6.1. Parylene thin films – transparent, flexible encapsulation

Parylene and its functional derivatives have a variety of different applications, including surface passivation of biomedical and implantable devices, surface functionalization for biosensors, generation of micro-scale patterns for neural probes, [1,2] as a dielectric in organic thin-film transistors (OTFTs), [3] a selectively permeable membrane for OTFT-based chemical sensors, [4] and an encapsulant for OTFTs, organic LEDs (OLEDs) and organic solar cells. [5,6]

Parylene is transparent and blocks moisture diffusion, enabling its use to encapsulate air-sensitive devices, such as OLEDs. While more permeable than inorganic films such as SiO_xN_y or Al_2O_3, [7] parylene can be vapor deposited as a conformal and flexible coating at very low substrate temperatures. There have been various methods of deposition of parylene polymer films, [1, 8], of which the most popular is parylene chemical vapor deposition (CVD) by the Gorham method, where the dimer is first evaporated and diffuses through a pyrolysis zone, where it breaks up into monomers, which then diffuse to a cooled substrate where polymerization occurs. [9-11] Often three separate reactor stages or chambers are employed, with each independently pumped to enable pressure driven vapor transport and polymerization occurring in a large vacuum chamber. A carrier gas may be employed to assist vapor transport, enhancing control of the deposition rate. [12, 13] However, traditional parylene coating systems are often limited in many applications by relatively low materials utilization efficiency, the difficulty in localizing the deposition area, a large footprint and high cost. Film patterning in such traditional coating systems requires the use of a shadow-mask that contacts the substrate, presenting additional challenges for processing. Other methods that have been developed for creating parylene micropatterns involve lithography, [14, 15] or micromolding. [16] Haplern *et al.* [17] developed a method called 'H-atom assisted jet vapor deposition of parylene' (**Figure 6.1**) which successfully patterned/conformally coated parylene-C and –N films onto cooled substrates. This technique employed an inert carrier gas (He or Ar) to transport the Parylene precursor (di-para-xylylene) through a pyrolysis/cracking chamber, where reactive monomers are formed. The monomer jet, coupled with a hydrogen plasma jet then impinges on to a cooled substrate (maintained much below room temperature, in vacuum) at supersonic velocities where polymerization occurs in the film by a free radical mechanism, which has been much studied, but not fully understood. The chemical vapor jet deposition (CVJD) presented in this chapter is quite similar to the technique developed by Haplern *et al*., [17] which the exception of being able to deposit parylene films in air, therefore making it the first ambient parylene deposition technique developed.

Parylene (a trade name for poly (p-xylylene) based polymers) is available as parylene-N, -C, -D, -AF4, etc., where all but the first are functionalized, halogenated derivatives of poly (p-xylylene). Over the years, a lot of scientific research has been reported on paralyne including the morphology and crystal structure of poly (p-xylylene) deposited at various substrate temperatures, [18-21] thermal properties of Parylene films, [9,12,22] barrier properties of Parylene films to various vapors and gases, [5,6,23-25] mechanical and electrical properties of the films, [9,26,27] the mechanism of the polymerization process, [9,13,28,29] and various applications of the Parylene polymers. [1-6,30,31]

The work presented in this chapter focuses on the novel deposition technique and the quality of the films deposited by it. Application specific characterization of the films, as discussed above, has not been reported here. The CVJD technique and an ultra-compact apparatus for localized deposition of Parylene-N in air, is introduced here. The dimer precursor of Parylene-N, di-para-xylylene is first sublimated into a stream of carrier gas, N_2. The latter transports the vapor through a pyrolysis zone and through a collimating nozzle that directs the jet onto a substrate, where polymerization occurs. Like GF-OVJP, the primary jet carrying the reactive monomers is coaxially surrounded by an inert gas guard jet to shield the monomer molecules from chemically reacting ambient air. Importantly, the collimation of the jet enables additive patterning of parylene, as well as reduction of the apparatus dimensions by orders of magnitude relative to its conventional analogues. In this chapter, the polymer films deposited are characterized, the processing variables are related to the film deposition rate and film quality, and technique is employed to encapsulate and prolong the operational lifetime of an archetypal organic light emitting device (OLED) containing a moisture- and oxygen-sensitive light emissive material.

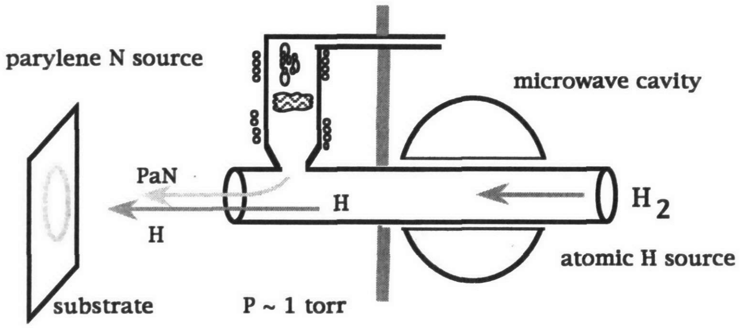

Figure 6-1. Schematic source for H-atom assisted JVD for Parylene-N deposition. [17]

6.2. CVJD technique

The traditional Gorham method [9,12] is combined with OVJP [32,33] and GF-OVJP, [34,35] to form the polymer chemical vapor jet deposition (CVJD). [36] The CVJD technique and ultra-compact apparatus is capable of depositing polymer films at any pressure, at increased materials utilization efficiency and enables direct additive patterning of parylene films on any surface of interest at near-room temperatures. The dependence of surface morphology and optical properties of the deposited films on process parameters such as carrier gas flow rate, sublimation and pyrolysis temperatures are discussed in detail.

A schematic of the parylene CVJD apparatus is shown in **Figure 6-2**, along with a typical temperature profile during deposition. The carrier gas (here, nitrogen) flows into a glass tube and picks up the sublimated parylene dimer molecules. The nitrogen–dimer mixture then flows through the heated pyrolysis section, where the dimers pyrolyse into monomers. These monomers then flow out of the nozzle and impinge as a high velocity jet on a cooled substrate, where they polymerize. The collimation enables localized parylene deposition.

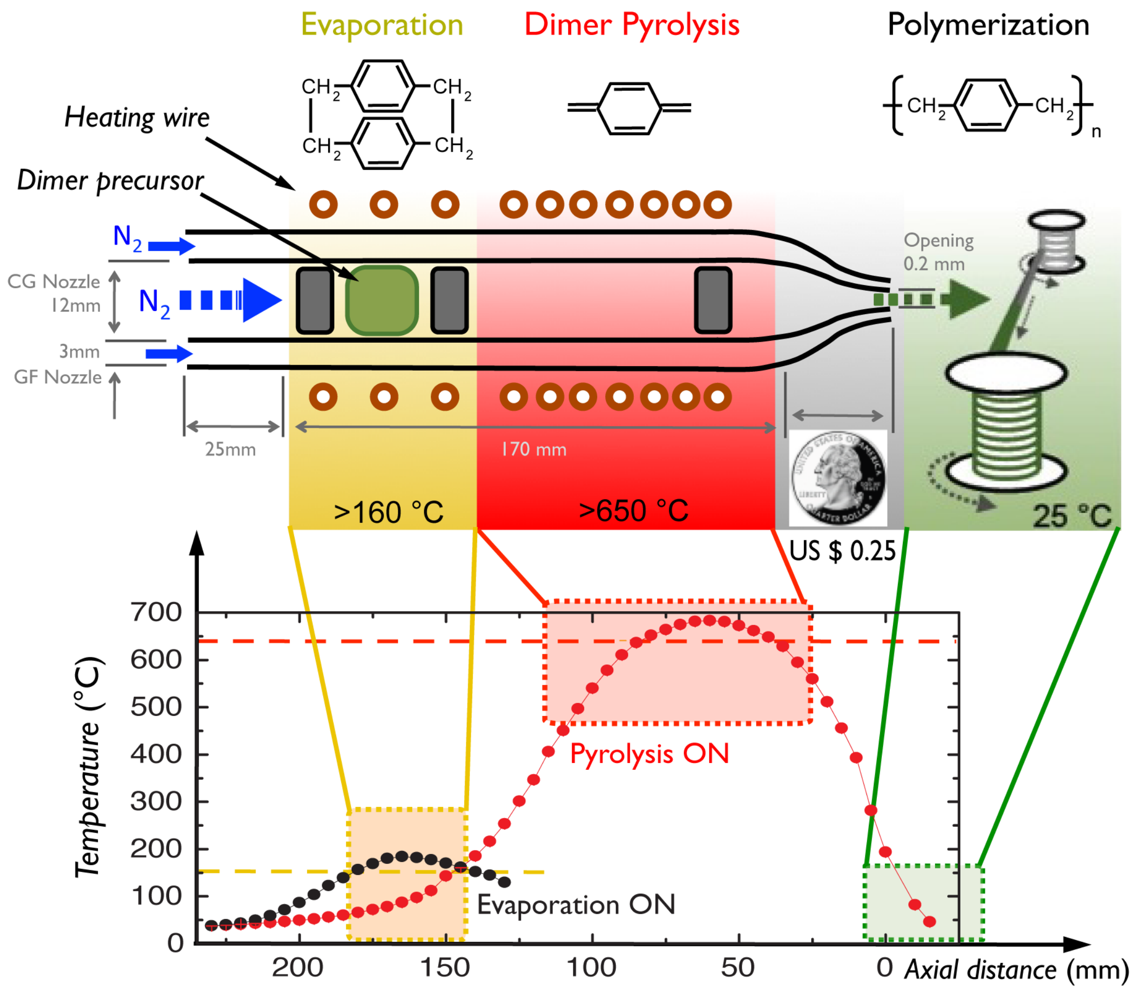

Figure 6-2. A schematic diagram of the ultra-compact parylene jet printing apparatus, which combines the conventional (Gorham) parylene deposition method with GF-OVJP. (top) Temperature profile along the axis of the nozzle specifying the spatial distribution of sublimation, pyrolysis and polymerization zones. (bottom) [36]

The rate of film growth and the film quality depend on several process parameters that can be individually controlled during the printing process. The main process parameters include: carrier gas flow rate (here varied between 20 and 200 sccm), guard flow rate

(500 sccm), sublimation zone temperature (e.g. 80-180^{o}C), substrate temperature (typically ~ 40°C), pyrolysis zone temperature (typically 680°C), residence time of the dimers in the pyrolysis zone ($\tau \geq 6$ s) and the deposition pressure (here 1 atm). Inside the source tube and in the region between the nozzle and the substrate, the Reynolds numbers are Re << 2300 and Re $\geq 5\times10^{4}$, respectively, signifying laminar flows. Note that since the substrate temperature, T_S, is near room temperature, CVJD can be applied to a wide range of substrates - flexible plastic films, fibers, or conventional planar substrates.

6.3. Polymerization as a function of processing parameters

The formation of parylene films on the surface occurs by direct physisorption, followed by surface diffusion and chemical bonding; the polymer growth depends on the rate of parylene monomer arrival to the surface, predicted by considering the evaporation, dimer transport, pyrolysis, and polymerization steps in sequence. First, consider the evaporation zone (*Zone 1*), shown in **Figure 6-3**. The rate of evaporation of parylene dimers, $r_{Ev}{}^{D}$ is given by

$$r_{Ev}^{D} = k_{Ev} P_{D}^{eq} \tag{6.1}$$

where k_{Ev} and $P_D{}^{eq}$ are the evaporation rate coefficient and equilibrium partial pressure of dimer molecules above the source, respectively. If P_D is the partial pressure of dimer molecules in the vapor, assuming a well-mixed condition, the rate at which the molecules would be transported along the tube out of the sublimation zone is the product of dimer concentration in the vapor and the volumetric flow rate of the carrier gas, Q_{CG} or just Q:

$$r^{D}_{transport} = \frac{QP_D}{RT_{Ev}} = r_D \tag{6.2}$$

where T_{Ev} is the vapor temperature in the evaporation zone and R is the universal gas constant. P_D and P_D^{eq} are related as follows, similar to Ref. [32]:

$$P_D = P_D^{eq} \frac{1}{1 + Q/k_{Ev}RT_{Ev}} \tag{6.3}$$

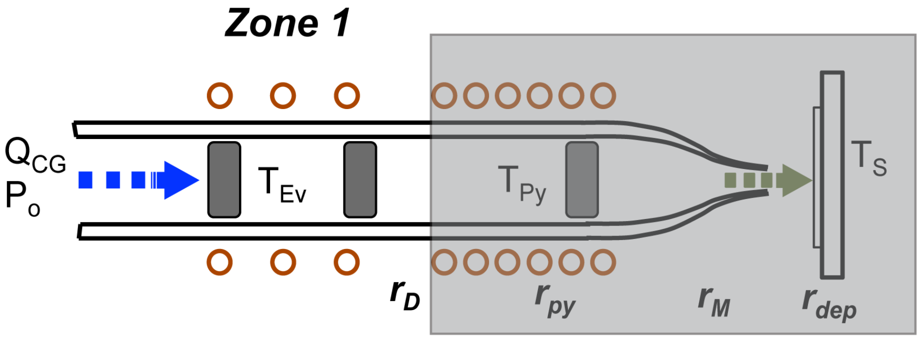

Figure 6-3. Schematic of the Evaporation Zone (*Zone 1*) with all the processing parameters to calculate the rate of dimer transport. [36]

The equilibrium vapor pressure of dimer in the evaporation zone is given by the Clausius-Clapeyron relationship:

$$P_D^{eq} = P_o \cdot \exp\left(\frac{-H_{Ev}}{RT_{Ev}}\right) \tag{6.4}$$

where P_o is a pressure constant, H_{Ev} is the enthalpy of evaporation/sublimation. The rate of dimers transported from the sublimation zone is obtained by combining **Eqs**. (**6.1-6.3**):

$$r_D = \frac{P_D^{eq}}{RT_{Ev}} \frac{Q}{1+Q/k_{Ev}RT_{Ev}} \tag{6.5}$$

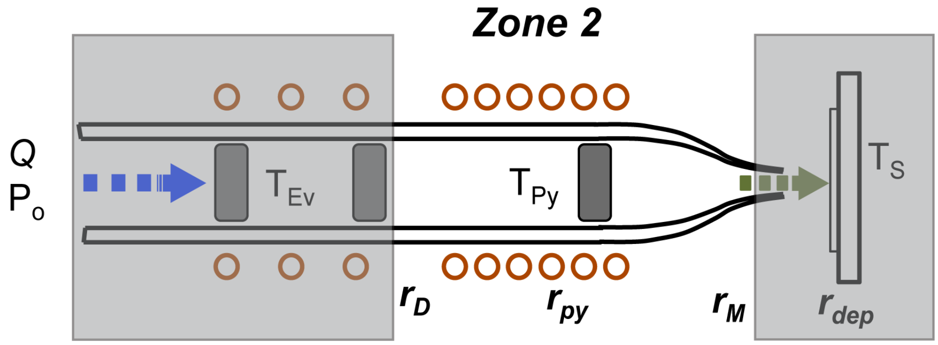

Figure 6-4. Schematic of the Pyrolysis Zone (*Zone 2*) with the processing parameters to calculate the rate of monomer formation and transport. [36]

The rate at which dimers are introduced into the pyrolysis zone (*Zone 2*), shown in **Fig. 6-4**, can be related to the film growth rate, via the rate of monomer creation, i.e. the pyrolysis rate corresponding to the reaction $D \xrightarrow{Tpy} 2M$, expressed as:

$$r_{py} = \frac{-d[D]}{dt} = \frac{1}{2}\frac{d[M]}{dt} = k_{py}[D] \tag{6.6}$$

where [*D*] and [*M*] are dimer and monomer concentrations, respectively and k_{py} is the pyrolysis rate constant, whose Arrhenius form is

$$k_{py} = A_{py} \exp\left(\frac{-E_{py}}{RT_{py}}\right) \tag{6.7}$$

It is convenient to define a pyrolysis efficiency, η_{py}, as the ratio of half the number of monomers generated to the number of dimers entering the pyrolysis zone; η_{py} is a function of the pyrolysis zone temperature, T_{py}, (from **Eq. 6.6** and **6.7**) and residence time, τ, of the dimers in this zone:

$$\eta_{py} = \frac{[M]}{2[D]} = \tau \cdot A_{py} \exp\left(\frac{-E_{py}}{RT_{py}}\right) \tag{6.8}$$

The residence time, τ, is the average time spent by the dimer molecules in the pyrolysis section. Assuming that the dimer vapor concentration in the flow is insignificant compared to the carrier gas and the gas in the tube is well mixed (via diffusion):

$$\tau = \frac{l \cdot A_{CS}}{Q} \tag{6.9}$$

where l and A_{CS} are the length and cross-sectional area of the pyrolysis section, respectively. Combining **Eq. 6.6** and **6.8**:

$$r_M = 2\eta_{py} r_D \tag{6.10}$$

The temperature profile in **Figure 6-2** indicates that the vapor temperature drops below 150°C just before exiting the nozzle, suggesting that some polymerization and/or condensation of the monomers may occur on the nozzle walls, somewhat reducing the monomer flux exiting the nozzle (*Zone 3*) by (1-$\eta_{non\text{-}cond}$):

$$r_M^{Zone3} = 2\eta_{py}\eta_{non-cond} r_D \tag{6.11}$$

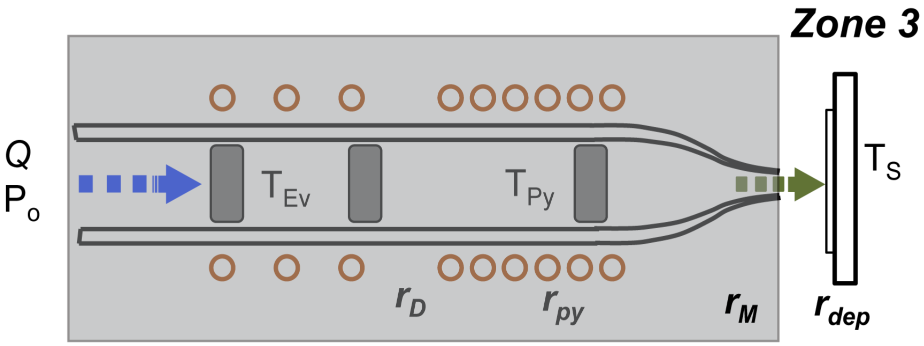

Figure 6-5. Schematic of the Polymerization Zone (*Zone 3*) where the monomers in the jet impinge on to the substrate, diffuse along the film surface, and polymerize at active sites. [36]

The rate of deposition of parylene as a chemical vapor deposition (CVD) process [28] is modeled as:

$$r_{dep} = SJ_M V_M N_a \tag{6.12}$$

where S is the sticking coefficient, which depends on the substrate material and temperature, N_a is Avogadro's number, V_M is the volume of each molecule and the quantity J_M is the flux of the monomers in the jet after exiting the nozzle (*Zone 3*), shown in **Fig. 6-5,** penetrating the boundary layer, derived from Fick's law of diffusion as:

$$J_M = D_M \frac{[M]}{\delta_S} \tag{6.13}$$

where D_M is the monomer diffusivity through the boundary layer of thickness δ_S. Note that, relative to vapor-to-solid transport in the Gorham method, in CVJD the added kinetic energy of the jet can enhance molecular diffusion of monomers along the surface to find polymerization sites. [37] For impinging flows [38]:

$$\delta_S = K_0\sqrt{\frac{\nu d}{Q}} \tag{6.14}$$

where K_0 is a numerical constant, ν is the kinematic fluid viscosity and d is the nozzle-substrate separation. Given that $[M] = \frac{r_M^{Zone3}}{Q}$ and incorporating **Eqs. 6.11**, **6.13** and **6.14** in **Eq. 6.12**, polymer deposition rate is:

$$r_{dep} = \frac{SV_M N_a D_M}{K_0}\frac{2\eta_{py}\eta_{non-cond}}{Q\sqrt{\frac{\nu d}{Q}}}r_D \tag{6.15}$$

Note that S is the sticking coefficient of the monomer on the substrate, given by $S = \left(1 + s_0\exp\left(\frac{-(E_d - E_a)}{RT_S}\right)\right)^{-1}$, E_a and E_d are the adsorption and desorption activation energies (not related to H_{Ev}) and s_0 is a kinetic pre-exponent. [28] Since these factors vary little over the range of substrate temperatures measured here, the expression for the film deposition rate can be reduced to:

$$r_{dep} = \frac{V_M N_a D_M}{K_0}\frac{r_M}{Q\sqrt{\frac{\nu d}{Q}}}\frac{1}{1 + s_0\exp\left(\frac{-(E_d - E_a)}{RT_S}\right)} \tag{6.16a}$$

Note that parylene deposition using the Gorham method typically requires substrate temperatures below 0 °C [28]. In comparison, CVJD uses a carrier gas with jet velocities ~ 200 m/s to transport parylene monomers to the substrate where they polymerize. The additional kinetic energy gained from the carrier gas jet stream enabling deposition at substrate temperatures as high as 50 °C. Additionally, the chain length of the polymer deposited by CVJD can be increased quite easily by decreasing the substrate temperature using a water chiller.

For fixed evaporation zone temperature and flow rate:

$$\ln(1/r_{dep}) = \ln C_0 - \left(\frac{E_d - E_a}{R}\right)\frac{1}{T_S} \tag{6.16b}$$

All the parameters other than the expression containing T_S in **Eq. 6.16a** are independent of substrate temperature and constant for the processing conditions in *Zone 3*. Hence they can be replaced by C_0, a process constant, as in **Eq. 6-16b**. At a given T_S, the deposition efficiency can be evaluated as $\eta_{dep} = r_{dep}/r_M$. Combining the efficiencies of the individual process steps, and with **Eq. 6.11**, $r_{dep} = \eta_{dep} r_M = 2\eta_{py}\eta_{non-cond}\eta_{dep} r_D = 2\eta r_D$ is obtained, where η is the overall process efficiency, which can be evaluated empirically.

6.4. Characterization of CVJD parylene films

The deposition rate can be obtained in terms of the variable process parameter Q and T_{Ev} by combining **Eq. 6.15** with **Eq. 5**:

$$r_{dep} = \frac{SV_M N_a D_M 2\eta_{py}\eta_{non-cond}}{K_0}\frac{1}{\sqrt{vdQ}}\left(\frac{P_D^{eq}}{RT_{Ev}}\frac{Q}{1+Q/k_{Ev}RT_{Ev}}\right) \tag{6.17}$$

For fixed process parameters T_{Ev}, d, T_{py} and T_S **Eq. 6.17** can be modified as:

$$\frac{1}{r_{dep}} = \frac{1}{a\sqrt{Q}} + \frac{\sqrt{Q}}{ak_{Ev}RT_{Ev}} \tag{6.18}$$

where a replaces all the constant factors; $a = \frac{SV_M N_a D_M 2\eta_{py}\eta_{non-cond}}{K_0}\frac{P_D^{eq}}{RT_{Ev}\sqrt{\nu d}}$ and Q, T_{Ev}, are the only independently varied parameters in **Eq. 6.17**. In **Figure 6-6**, the inverse of deposition rate is plotted against the square root of the carrier gas flow rate for two fixed sublimation zone temperatures.

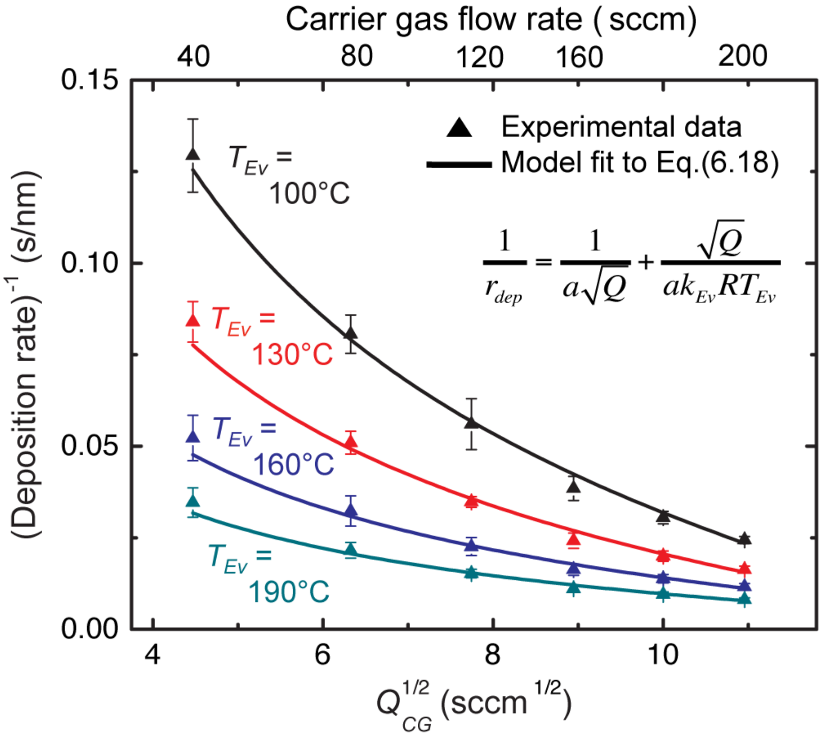

Figure 6-6. The variation of deposition rate with (Carrier gas flow rate)$^{1/2}$ are plotted for four different evaporation zone temperatures are plotted. The solid lines shows the model and symbols represent experimentally measured data. The fitting parameters a and k_{Ev} can be calculated from the fitting. [36]

Fitting **Eq. 6.18** (solid lines) to the data in **Figure 6-6**, values for k_{Ev} and a can be obtained and are listed in **Table 6.1**. k_{Ev} is evaluated to be around $9.5 \cdot 10^{-2}$ mol/s-Pa corresponding to all the T_{Ev} values. At higher carrier gas flow rates the pressure in the sublimation zone is higher which in-turn reduces the k_{Ev}, hence the concentration of evaporated dimer in the vapor reduces, resulting in a slightly lowered deposition rate than predicted by **Eq. 6.18**.

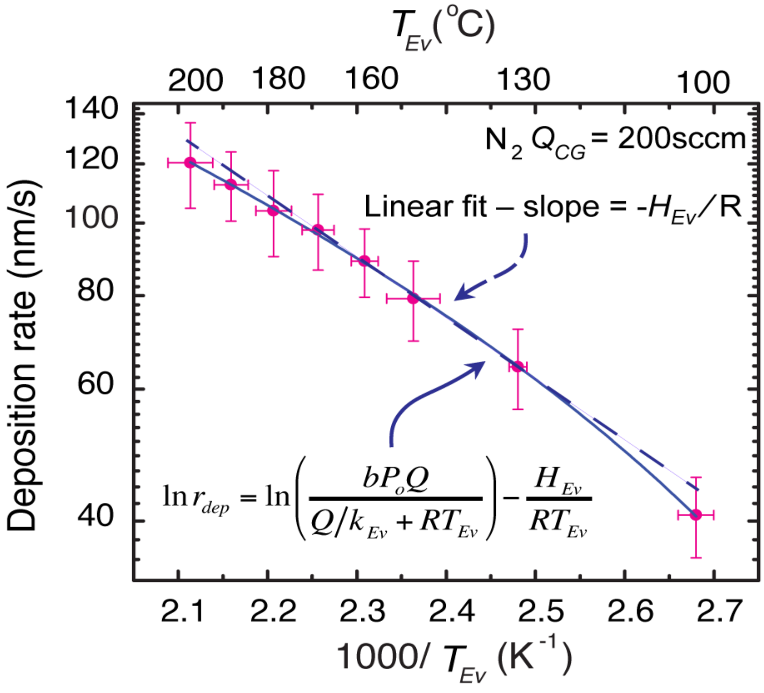

Figure 6-7. The deposition rate obtained at various dimer evaporation temperatures, while holding the carrier gas flow rate constant (Q_{CG} = 200 sccm), is plotted. An exponential increase in the growth rate is expected but the deposition rate appears to saturate at high evaporation rates experimentally. The enthalpy of evaporation is calculated from the slope of the fitted line. [36]

To evaluate the effect of sublimation temperature on the deposition rate a separate experiment was carried out by increasing T_{Ev} while the carrier gas flow rate, separation, pyrolysis and substrate temperatures, Q, d, T_{py} and T_S respectively, were held constant.

The results are plotted in **Figure 6-7**. An exponential increase in the growth rate is expected with T_{Ev} (**Eq. 6.4**). However, the RT_{Ev} term in **Eq. 6.17** limits the deposition rate. The combined rate equation from **Eqs. 6-4** and **6-17**, denoting the combined constant terms in **Eq. 6.17** as $b = \dfrac{SV_M N_a D_M 2\eta_{py}\eta_{non-cond}}{K_0\sqrt{\nu dQ}}$, is:

$$\ln r_{dep} = \ln\left(\frac{bP_oQ}{Q/k_{Ev} + RT_{Ev}}\right) - \frac{H_{Ev}}{RT_{Ev}} \cong C_1 - \frac{H_{Ev}}{RT_{Ev}} \qquad (6.19)$$

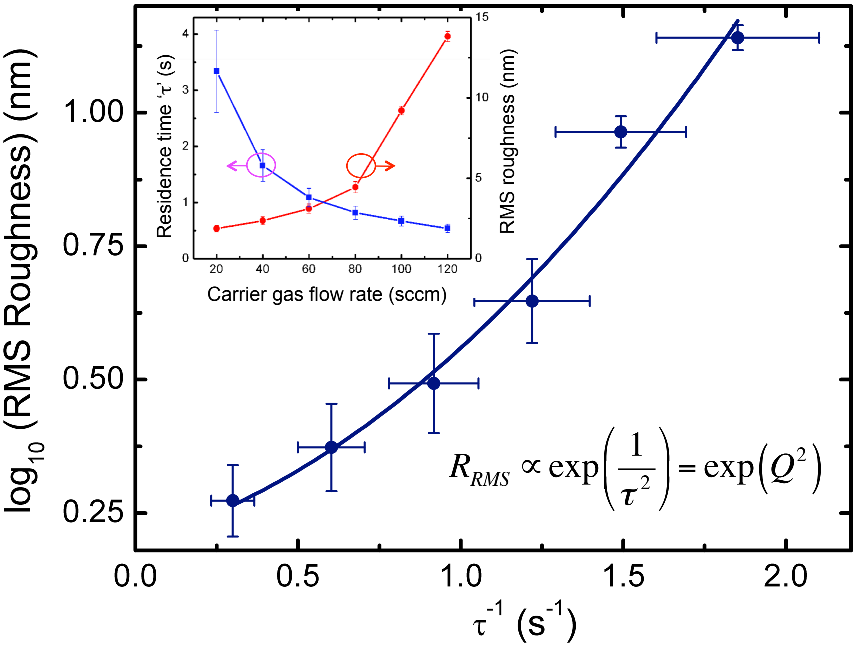

Figure 6-8. Deposited film roughness varies as the exponential of the square of τ^{-1}; the inset shows residence time is inversely proportional to the carrier gas flow rate. [36]

The value of $RT_{Ev} << (Q_{CG}/k_{Ev})$ is approximately 100 kJ/mol, making the argument of the logarithm in Eq. (6.19) independent of T_{Ev} at lower evaporation zone temperatures, which can be approximated as a constant, C_1. The equation becomes approximately linear (**Figure 6-7**), allowing the enthalpy of sublimation to be evaluated from the slope as H_{Ev} = -37.23 kJ/mol. Heat of vaporization of parylene-N dimer has been recorded as -42.4 kJ/mol, [39] which validates the theoretical model presented here. The saturation in the deposition rate at higher T_{Ev} occurs due to dimer and hence monomer transport reentering the flow-limited regime at a given carrier gas flow rate.

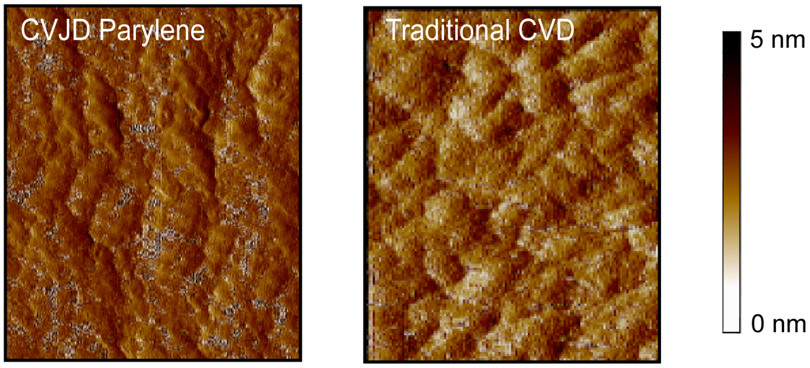

Figure 6-9. At carrier gas flow rates below 120 sccm, CVJD parylene-N films (left) have roughness similar to conventionally CVD deposited films (right), as seen in the AFM images of 110 nm parylene-N films. [36]

Figure 6-8 indicates that the deposited film roughness increases as the exponential of square of the carrier gas flow rate. This phenomenon is explained by the fact that the residence time, τ, decreases with flow rate, increasing the presence of unpyrolysed dimer that could be trapped into the film or result in disruption of the polymerization. [40] The root mean square (RMS) roughness varies inversely with the flow rate as well as τ, as can be seen from the inset.

It has been reported previously that 100% dimer conversion occurs for pyrolysis temperatures above 680°C. [12] However, since the pyrolysis zone in this particular CVJD apparatus is limited to 40 mm, there is a chance of unpyrolyzed, not reactive dimer getting through to the film at higher carrier gas flow rates. One potential solution to mitigate the problem of unpyrolized dimer would be to introduce baffles perpendicular to the nozzle axis, there by artificially increasing the length '*l*' travelled by dimer in the pyrolysis zone. For flow rates below 120 sccm, roughness of the CVJD films are found to be similar to films deposited in traditional Gorham CVD chamber, as shown in the AFM images in **Figure 6-9**.

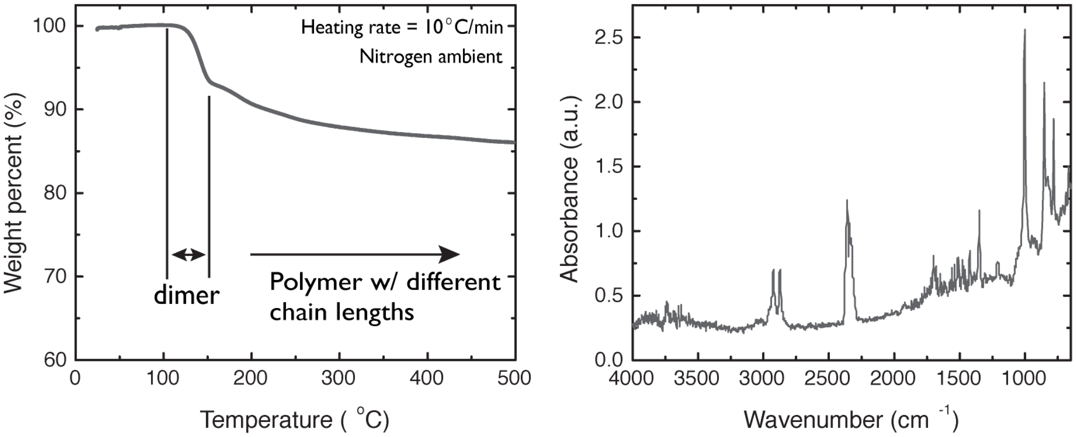

Figure 6-10. TGA and FT-IR spectrum indicate the quality of the CVJD parylene-N films. Dynamic TGA of 2 gm parylene (left) suggests that there is 6% dimer impurities incorporated in the deposited polymer film. FT-IR peaks of CVJD films show a good match to literature [42]. [36]

Polymer film composition and quality is confirmed only by TGA and Fourier transform infrared (FT-IR) spectroscopy; since parylene-N does not dissolve any common solvent at room temperature, its extremely hard to test the polymer quality using techniques like Matrix-assisted laser desorption/ionization (MALDI), differential scanning calorimetry (DSC) or gel permeation chromatography (GPC). Parylene-N films deposited using CVJD in air contain ~ 6% unpyrolyzed dimer in the film for the processing conditions mentioned above. **Figure 6-10** is a plot of the dynamic TGA and FT-IR absorbance spectrum show a good match with literature. [41,42] Shorter polymer chains of parylene are expected for CVJD grown films due to substrate temperatures and deposition rates higher than with conventional growth in vacuum. [43]

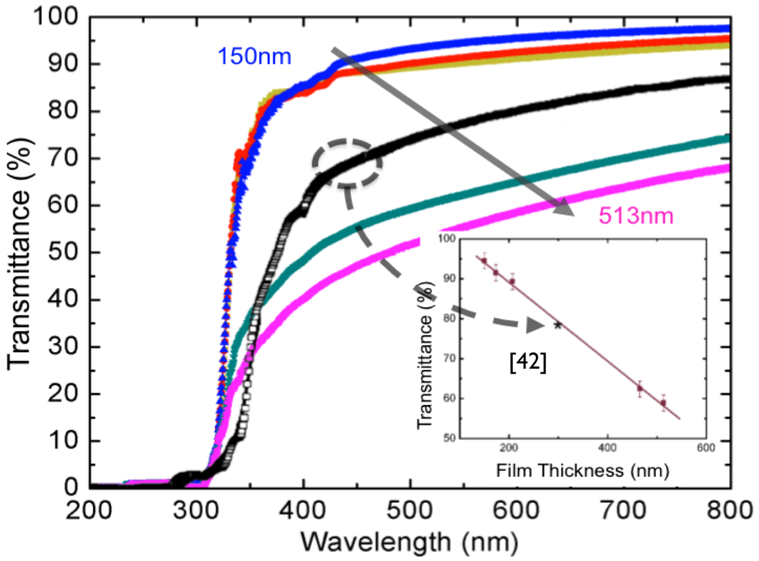

Figure 6-11. Optical spectrum in the visible and UV range as a function of thickness. Inset shows a linearly decreasing trend of transmission with thickness at a wavelength of 555 nm. [36]

Figure 6-11 shows that thicker parylene films are more opaque, as expected. The transmissivity at optical wavelength of 500 nm is plotted in the inset of **Figure 6-11**, for the different film thicknesses. The literature value of transparency for a film thickness of 300 nm lies on the linear fit of the measured transparencies of CVJD grown films. [43] For sufficiently thin films (below 200 nm), the transmission is greater than 90% across the visible wavelength range, important if parylene were to be used as an encapsulant for optoelectronic devices.

6.5. Encapsulation properties of CVJD parylene films

To test the barrier properties of CVJD grown parylene films, a batch of OLEDs was fabricated using vacuum thermal evaporation, followed by encapsulation with 500 nm of parylene (**Figure 6-12**). The current density-voltage (J-V) characteristics and emission spectra for the coated and uncoated devices were comparable, indicating that jet-printing parylene onto the OLEDs did not affect the metal electrodes or active organic semiconductor layers. For convenience and to accelerate aging, devices were stored in ambient air after fabrication. The parylene coating was deposited on the fabricated devices in ambient air. The EQE of the uncoated and coated devices, tested immediately after fabrication, were 0.852% and 0.743%, respectively, at a current density of 1 mA/cm^2 (inset of **Figure 6-12**), the difference most likely due to capping layer induced microcavity effects. The luminous flux of the OLEDs was measured over the course of two days, while being stored in air between each test. CVJD-coated devices exhibited significantly longer lifetimes (**Figure 6-12**), highlighting the usefulness of parylene as an oxygen and moisture barrier for electronic devices. While parylene by itself is not an optimized encapsulation material, it can potentially be used in combination with other materials to further reduce permeation of moisture and oxygen into devices. [44]

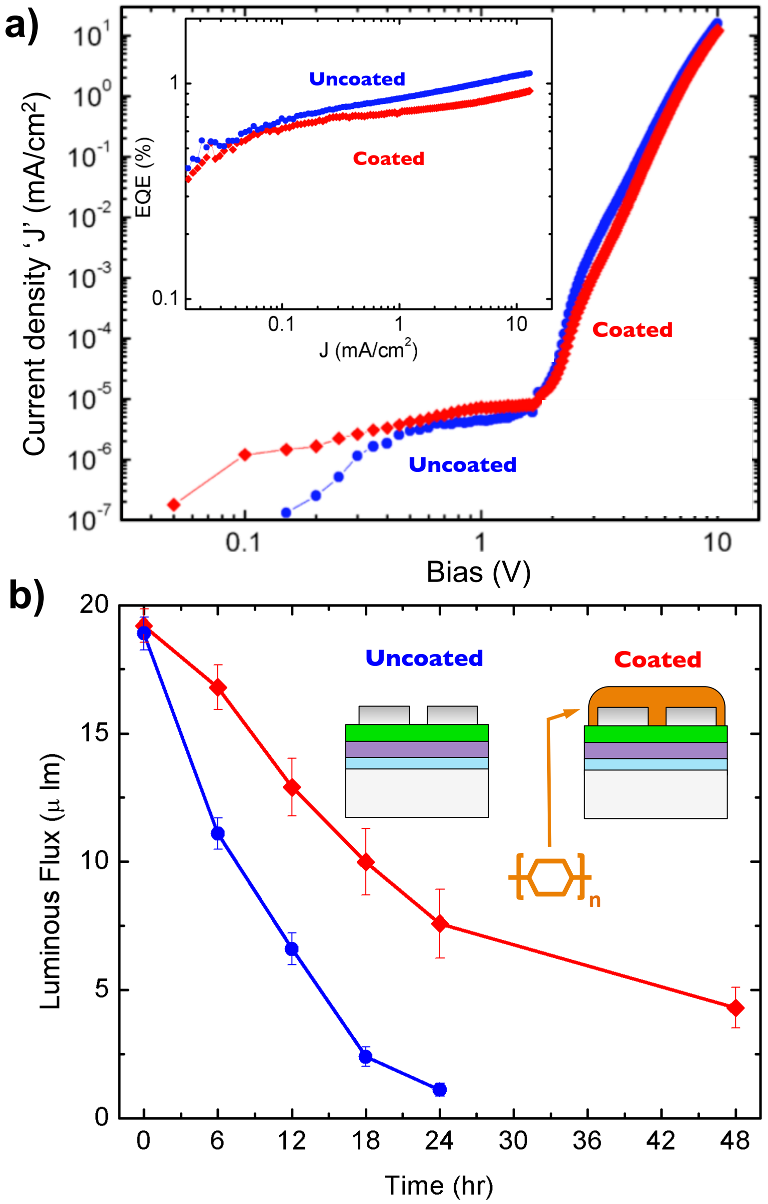

Figure 6-12. Parylene encapsulated OLED performance and lifetime: **(a)** Comparison of I-V characteristics and external quantum efficiency curves of identical OLEDs coated and uncoated with parylene as an encapsulant are plotted. The devices were tested immediately after fabrication. **(b)** Inset cartoon shows OLED structure with ITO on glass substrate, α–NPD (50 nm), Alq_3 (60 nm) and LiF/Al cathode (1/90 nm). The coated devices had 500 nm of parylene deposited on the top while the device was tested for bottom emission. CVJD encapsulated devices show longer lifetimes, confirming deposited parylene's barrier properties. [36]

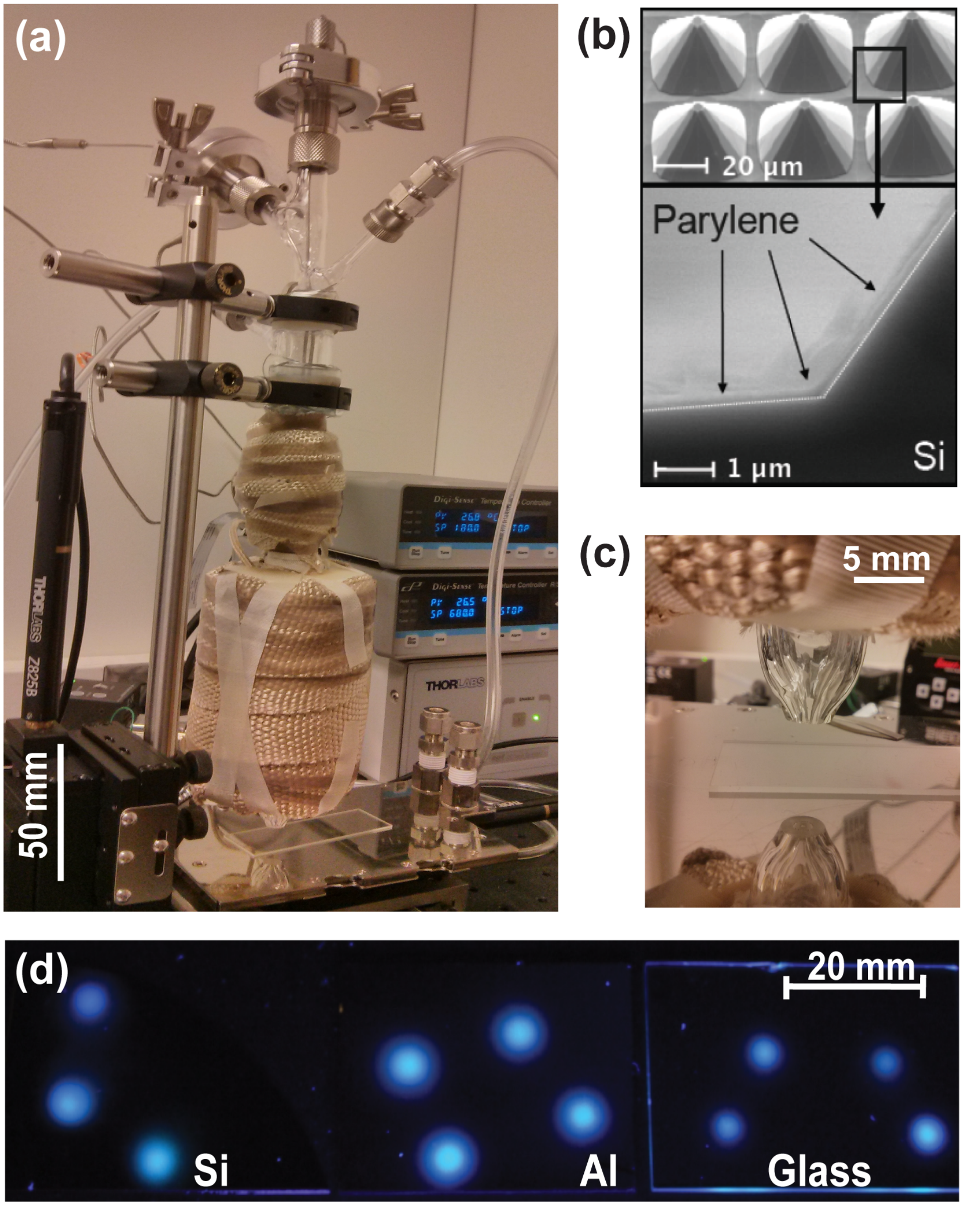

Figure 6-13. Images of CVJD nozzle and parylene-N deposits. (a) The CVJD nozzle is compact (~8”) and can deposit/pattern parylene in air. (c) is the magnified image of the nozzle tip over the substrate. (b) shows an SEM image confirming the capability of CVJD to deposit conformal coatings of parylene-N on non-planar (here pyramidal Si) substrates. (d) Patterns of parylene deposited on Si, Al coated glass and glass substrates shown under UV illumination. Each deposit is < 200 nm thick and is transparent in visible light. The patterns on aluminum (120 nm) coated glass are more dispersed due to the low sticking coefficient of parylene on the Al. [36]

6.6. Summary

A new additive patterning method for parylene deposition has been demonstrated by merging the conventional method of chemical vapor deposition of parylene with the more GF-OVJP. The result is a very compact parylene-printing nozzle that can be integrated with other deposition instruments. This technique allows direct, additive patterning of parylene in one step. Patterning capabilities of CVJD are very similar to those of GF-OVJP. Using the appropriate dimensions of nozzle diameter '*D*' and nozzle-substrate separation '*s*' any desired pattern with high resolution can be printed using CVJD. The inert carrier gas jet surrounded by an inert guard flow jet ensures minimal diffusion of ambient gases such as O_2 and water vapor at the point of polymerization, allowing parylene to be deposited in atmosphere. Furthermore, the carrier gas jet enables deposition by CVJD at substrate temperatures as high as 50°C, thereby reducing the need for substrate cooling. Moreover, high materials utilization efficiency and very high local deposition rates make CVJD a highly desirable tool. **Figure 6-13** shows images of the compact CVJD tool along with deposited patterns of parylene-N on three different substrates. An analytical expression relating the deposition rate of parylene to all other controllable processing parameters is derived in this section and validated with experiments.

Deposition of parylene by this jet printing technique affords high control of deposition rates and properties such as surface roughness, optical transmission, and moderate barrier properties via several process parameters. This technique can potentially be extended to the functional patterning of other similar polymers, [45] and can be implemented as a tool for device encapsulation for lab scale testing. Future applications can also include parylene patterning for bio-functionalized surfaces and chemical sensors.

6.7. References

[1] J. Lahann, “Vapor-based polymer coatings for potential biomedical applications”, *Polymer International* **2006**, *55*, 1361.

[2] P. J. Chen, D. Rodger, S. Saati, M. Humayun, Y. Tai, “Microfabricated Implantable Parylene-Based Wireless Passive Intraocular Pressure Sensors*”, Journal of Microelectromecanical Systems* **2008**, *17*, 1342.

[3] K. Diallo, M. Lemiti, J. Tardy, F. Bessueille, N. Jaffrezic-Renault, “Flexible pentacene ion sensitive field effect transistor with a hydrogenated silicon nitride surface treated Parylene top gate insulator”, *Appl. Phys. Lett.* **2008**, *93*, 183305.

[4] V. Podzorov, V.M. Pudalov, M.E. Gershenson, “Field-effect transistors on rubrene single crystals with parylene gate insulator”, *Appl. Phys. Lett.* **2003**, *82*, 1739.

[5] P. Madakasira, K. Inoue, R. Ulbricht, SB. Lee, M. Zhou, JP. Ferraris, A.A. Zakhidov, “Multilayer encapsulation of plastic photovoltaic devices”, *Synthetic Metals* **2005**, *155*, 332.

[6] TN. Chen, D. Wuu, C. Wu, C. Chiang, Y. Chen, R. Horng, “Improvements of Permeation Barrier Coatings Using Encapsulated Parylene Interlayers for Flexible Electronic Applications” *Plasma Processes and Polymers* **2007,** *4*, 180.

[7] C. Charton, N. Schiller, M. Fahland, A. Hollander, A. Wedel, K. Noller, “Development of high barrier films on flexible polymer substrates”, *Thin Solid Films* **2006***, 502*, 99.

[1] J. Ultley, Y. Gao, J. Gruber and R. Lines, "Electrochemical route to xylylene polymers and copolymers *via* cathodically generated quinodimethanes: preparative and structural aspects", *J. Mater. Chem.* **1995**, *5*, 1297.

[2] W. Gorham, "A New, General Synthetic Method for the Preparation of Linear Poly-*p*-xylylenes", *J. Polymer Science Part A-1* **1966**, *4*, 3027.

[3] K Crain, J Wary, RA Olson, WF Beach, "Parylene deposition apparatus including a quartz crystal thickness/rate controlled", *US Patent 5,536,317*, **1996**.

[4] M. Szwarc, "New monomers of the quinoid type and their polymers", *J. Polymer Science* **1951**, *6*, 319.

[5] J.B. Fortin, T. Lu, *Chemical Vapor Deposition Polymerization: The growth and properties of parylene thin films*, Ed. 1, Kluwer Academic Publishers, Norwell, Massachusetts, **2004**, Ch. 1.

[6] P. Kramer, A. K. Sharma, E. E. Hennecke, H. Yasuda, " Polymerization of para-xylylene derivatives (parylene polymerization). I. Deposition Kinetics for Parylene N and Parylene C", *Journal of Polymer Science: Polymer Chemistry Edition*, **1984** *22*, 475491 (1984)

[7] J. A. DeFranco, B. S. Schmidt, M. Lipson, G. G. Malliaras, "Photolithographic patterning of organic electronic materials", *Organic Electronics*, **2006**, *7*, 22

[8] C. P. Tan, B. R. Cipriany, D. M. Lin and H. G. Craighead, "Nanoscale Resolution, Multicomponent Biomolecular Arrays Generated By Aligned Printing With Parylene Peel-Off" *Nano Lett.*, **2010**, *10*, 719.

[9] H. S. Noha, Y. Huang, P. J. Hesketh, "Parylene micromolding, a rapid and low-cost fabrication method for parylene microchannel", *Sensors and Actuators B: Chemical*, **2004**, *102*, 78.

[10] B. L. Halpern, P. Komarenko, R. F. Graves, P. D. Fuqua, J. F. Mcdonald, G.-R. Yang, L. Wang, T. M. Lu, M. Tomozawa and I. Maitthew, "H-atom assisted jet vapor deposition of Parylene-N polymer", *Plasma Deposition and Treatment of Polymers*, **1999**, *544*, 153.

[11] S. Kubo and B. Wunderlich, "Crystal structure of alpha poly para xylelylene"**,** *J. Appl. Phys.*, **1971**, *42*, 4565.

[12] Y.-S. Yeh, W. J. James, H. Yasuda, "Polymerization of *para*-xylylene derivatives. VI. morphology of parylene N and parylene C films investigated by gas transport characteristics", *J. Polymer Science B: Polymer Physics*, **1990**, *28*, 545.

[13] G. Treiber, K. Boehlke, A. Weitz, and B. Wunderlich, "Crystallization during polymerization of poly-para-xylelylene**"** *J. Polym. Sci. A-2*, **1973**, *11*, 1111.

[14] U. Goschel, H. Walter, "Surface Film Formation by Chemical Vapor Deposition of Di-*p*-xylylene: Ellipsometrical, Atomic Force Microscopy, and X-ray Studies" *Langmuir* **2000,** *16,* 2887.

[15] H. H. G. Jellinek and S. N. Lipovac, "Vacuum and oxidative pyrolysis of poly para-xylelylene", *J. Polym. Sci. A-1*, **1970**, *8*, 2517.

[16] M. A. Spivack and G. Ferrante, "Determination of the Water Vapor Permeability and Continuity of Ultrathin Parylene Membranes", *J. Electrochem. Soc.*, **1969**, *116*, 1592.

[17] T. E. Baker, S. L. Bagdasarian, G. L. Fix, and J. S. Judge, "Characterization of Vapor-Deposited Paraxylylene Coatings", *J. Electrochem. Soc.*, **1977**, *124*, 897.

[18] Y. S. Yoon, H. Y. Park, Y. C Lim, K. G. Choi, K. C Lee, G. B Park, C. J. Lee, D.G. Moon, J. I. Han, Y. B. Kim, S. C. Nam, "Effects of parylene buffer layer on flexible substrate in organic light emitting diode", *Thin Solid Films*, **2006**, *513*,

258.

[19] M. A. Spivack, “Parylene thin films for radiation applications”, *Rev. Sci. Instrum.* **1970**, *41*, 1614.

[20] G. E. Loeb, M. J. Bak, N. Salcman, and E. M. Schmidt, “Parylene as a Chronically Stable, Reproducible Microelectrode Insulator”, *IEEE Trans. Biomed. Eng.*, **1977**, *24*, 121.

[21] J. B. Fortin, T-M. Lu, “A Model for the Chemical Vapor Deposition of Poly(para-xylylene) (Parylene) Thin Films”, *Chemistry of Materials* **2002**, *14*, 1945.

[22] D. J. Cram and N. Allinger, “Macro Rings .12. Stereochemical consequesnces of steric compression in the smallest paracyclophane”, *J. Am. Chem. Soc.*, **1955**, *77*, 6289.

[23] B. O’Connor, K.H. An, Y. Zhao, K.P. Pipe, M. Shtein, “Fiber shaped organic light emitting device”, *Advanced Materials* **2007**, *19*, 3897.

[24] K.H. An, B. O’ Connor, Y. Zhao, K.P. Pipe, M. Shtein, “Scanning optical probe microscopy with submicrometer resolution using an organic photodetector”, *Applied Physics Letters* **2008**, *93*, 033311.

[25] M. Shtein, P. Peumans, J.B. Benziger, and S.R. Forrest, “Direct mask-free patterning of molecular organic semiconductors using organic vapor jet printing” *Journal of Applied Physics* **2004**, *96*, 4500.

[26] Y.R. Sun, M. Shtein, S.R. Forrest, “Direct patterning of organic light-emitting devices by organic-vapor jet printing”, *Applied Physics Letters* **2005**, *86*, 113504.

[27] S. Biswas, K.P. Pipe, M. Shtein, “Solvent-free, direct printing of organic semiconductors in atmosphere”, *Applied Physics Letters* **2010**, *96*, 263301.

[28] S. Biswas, K. A. Luck, M. Shtein, “Guard flow-enhanced organic vapor jet printing of photovoltaic donor materials in air”, *Org. Electron.* **2012**, *13*, 2905.

[29] S. Biswas, T. Arbel, K. P. Pipe, M. Shtein, “Chemical vapor jet deposition of parylene in air”, **2014** (*in preparation*).

[30] G. Odian, *Principles of Polymerization*, Ed. 4. John Wiley & sons, Inc. publication, Hoboken, New Jersey, **2004**, Ch. 2.

[31] P.N. Gadgil, “Single wafer processing in stagnation point flow CVD reactor: Prospects, constraints and reactor design”, *Journal of Electronic Materials* **1993**, *22*, 171.

[32] W.F. Beach, *Xylylene Polymers*: *Encyclopedia Of Polymer Science and Technology*, Ed. Online, John Wiley & sons, Inc., **2004**.

[33] S. Ganguli, H. Agrawal, B. Wang, J. F. McDonald, T. -M. Lu, G.-R. Yang, and W. N. Gill, “Improved growth and thermal stability of Parylene films”, *J. Vac. Sci. Technol. A*, **1997**, *15*, 6.

[34] Y.-P. Zhao, J.B. Fortin, G. Bonvallet, G.-C. Wang, T.-M. Lu, “Kinetic Roughening in Polymer Film Growth by Vapor Deposition”, *Physical Review Letters* **2000**, *85*, 3229.

[35] T. Lee, J. Lee, C. Park, “Characterization of Parylene Deposition Process for the Passivation of Organic Light Emitting Diodes”, *Korean Journal of Chemical Engineering* **2002**, 19, 722.

[36] Y.S. Jeong, B. Ratier, A. Moliton, L. Guyard, “UV–visible and infrared characterization of poly(p-xylylene) films for waveguide applications and OLED encapsulation”, *Synethic Metals* **2002**, 127, 189.

[37] N. Kim, W. J. Potscavage, Jr., B. Domercq, B. Kippelen, S. Graham, “A hybrid

encapsulation method for organic electronics", *Applied Physics Letters* **2009**, 94, 163308.

[38] H. G. Choi, J. P. Amara, T. M. Swager, K. F. Jensen, "Synthesis and characterization of poly(isobenzofuran) films by chemical vapor deposition", *Macromolecules*, **2006**, *39*, 4400.

CHAPTER 7

Conclusions and Future Work

7.1. Achievements of GF-OVJP technique

This doctoral thesis reports the work on the development of a new deposition technique called guard flow-enhanced organic vapor jet printing (GF-OVJP) and the first demonstration of printing/depositing small molecular semiconductor materials and devices in air using this tool. High performance and unique functionality and variety of molecular organic semiconductors open exciting new opportunities in a variety of applications, including information displays, solar energy harvesting, large-area and ubiquitous electronics, and many others. The growing opportunity for manufacturing scale up in turn requires better control of large-scale processing of thin-film, organic semiconductor devices. Over the years, many different deposition techniques have been developed, the most commonly used among them is vacuum thermal evaporation (VTE). These methods require moderately large vacuum chambers and the use of shadow masks to pattern which inherently leads to wastage of majority of the active organic material delivered to the substrate, reducing manufacturing throughput and increases process complexity and cost. Moreover, the processing parameters used to control morphology are usually limited to substrate temperature and rate of deposition of the organics.

GF-OVJP is a physical vapor deposition technique that enables atmospheric, solvent-free, mask-free, direct, additive patterning of the organic films in air. It is compact, inexpensive and scalable with minimal material wastage and extremely high local deposition rates. The technique uses an inert carrier gas to transport sublimated organic vapor towards the substrate in the form of a high velocity, focused jet, surrounded by an annular inert guard jet to prevent degradation of the hot organic material due to ambient oxygen and moisture exposure.

The technique has more than six independently controllable parameters, each of which influences the morphology and electronic properties of the deposited film. In **Chapter 2** these processing parameters are discussed in detail, with their impact of film quality, in order to set up design principles for the implementation of GF-OVJP to any desired future applications. The primary parameter that was focused on in this work was guard jet mass flow rate, since adding the guard flow (*GF*) to the existent OVJP technique [1] is what enables the novel in-air printing. An archetypal green OLED with its emissive layer patterned by GF-OVJP successfully demonstrated that device quality films can be deposited by this technique in air. [2] Moreover, the guard flow rate parameter was used to optimize the film growth conditions to attain comparable high quantum efficiency and luminous power of the fabricated OLEDs as analogous devices deposited by VTE. (**Chapter 3**)

Next, the active layers of organic photovoltaic (OPV) devices were deposited by GF-OVJP in air, in order to understand the influence of guard flow rate on the film morphology. Large area films of the donor and acceptor layers were grown in air by this technique and *GF* mass flow rate was related to the crystallinity and roughness of the deposited layers. The donor layer (SubPc) used in the experiments is usually grown as amorphous films, and need post deposition processing with solvents or annealing to introduce crystalline domains. However, due to the unique flow dynamics of GF-OVJP, the SubPc films deposited at high guard flow rates were crystalline [3] and **Chapter 4** illustrates the process-structure relationship of the technique and it effects on OPV device performance. The acceptor material, C_{60}, was also grown by GF-OVJP and the first demonstration of an inverted structure OPV with all its active layers deposited in air is shown in **Chapter 4**.

With a good understanding of the process-structure relationship of depositing organic thin films with GF-OVJP in air, fabrication organic thin film transistors (TFT) was attempted, with the organic layer patterned in air. Common TFT materials like Tetracene, DNTT, Indigo, Quinacridone, and Pentacene were all used to successfully fabricated working devices with field-effect mobilities ranging from 0.1 – 1 cm^2/V-s. However, pentacene TFTs was the material of choice to explore and understand the effect of air exposure during deposition to the film crystallinity and electronic properties, in order to build the foundation to a ubiquitous process-structure-property relationship of depositing in air. The pentacene films were grown with a controlled amount of air exposure during deposition. The crystallinity of the films were studied using a synchrotron based XRD and an analytical expression was developed relating the Bragg peak intensity of the pentancene films to the amount of air exposure. A similar exercise was carried out to relate the mobility of the films and the air exposure during the growth of TFTs, while isolating the influence of oxygen and moisture interactions with the hot organic molecules during deposition from the influence of thickness, growth rate and other parameters. A direct correlation was established between the growth conditions, crystallinity, hole transport mobility and air exposure in pentacene films grown in air. [4]

Each organic material has a different sensitivity to oxygen and moisture exposure – for example, DNTT is rather insensitive to ambient exposure (shown in **Figure 7-1**), but the analysis presented in **Chapter 5** is valid for all materials deposited in air. Using the same deposition conditions as mentioned in the experimental section, the average mole fraction of oxygen and moisture interacting with the organic molecules during deposition would be identical. The extent of degradation of the material, and therefore, the effect of air exposure on crystallinity and mobility would depend on each material's specific sensitivity.

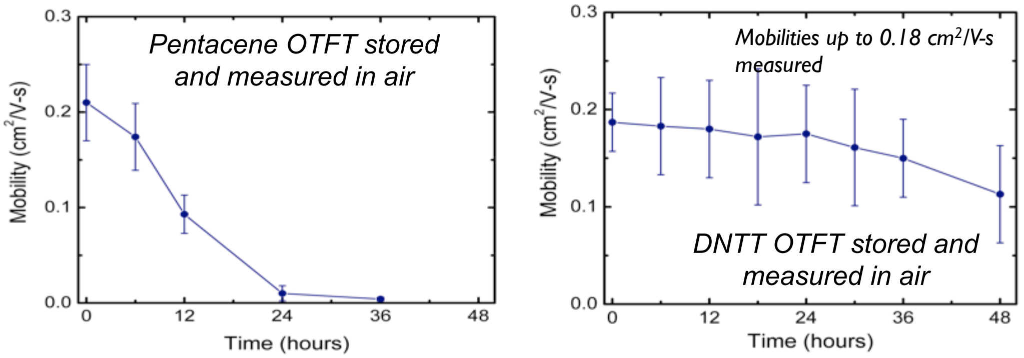

Figure 7-1. Lifetime of OTFT devices, stored and test in air, with pentacene (left) and DNTT (right) deposited in air by GF-OVJP. DNTT is quite insensitive to oxygen and moisture exposure, unlike pentacene. [4]

In **Chapter 6**, the GF-OVJP technique is modified with an additional pyrolysis section in the nozzle, to enable chemical vapor deposition of parylene polymer in air. This technique is called chemical vapor jet deposition or CVJD. Parylene films are commonly used as transparent, flexible coatings in electronic devices and bio-medical applications, exhibiting anti-corrosive properties, low dielectric constant (2.4 – 2.65) and moisture resistance. Reactive vapor deposition of parylene results in conformal coverage of features at room temperature, which is advantageous for passivating organic optoelectronic devices. Conventional parylene deposition systems, however, utilize separate chambers for vaporization, pyrolysis, and polymerization, resulting in a large footprint and limited processing integration ability, especially at a laboratory scale.

The CVJD technique enables the vaporization and pyrolysis of [2,2]paracyclophane (parylene dimer) in a single compact nozzle, producing a jet of monomer that polymerizes into a film upon contact with the substrate at room temperature. The monomer-laden jet is surrounded by an annular guard jet, like GF-OVJP, to shield the metastable monomers from chemically reacting with ambient air. [5] The effects of jet flow dynamics on the deposition rate and film morphology are discussed in detail in **Chapter 6**. Potential advantages of this approach include increased material utilization efficiency, localized conformal coating capabilities, and an apparatus that is compact, inexpensive, and does not require a vacuum pump.

7.2. Future directions

Since GF-OVJP is a relatively new technique, it can be applied to many different applications, while still discovering novel and unique nano-scale morphologies attainable through exploration of its processing parameters and deposition conditions. A few of these directions are listed below.

7.2.1. Improving the resolution of deposited pixels

As mentioned in **Chapters 2** and **3**, GF-OVJP parameters can be used to improve the patterning resolution of deposited pixels for OLED based display and lighting applications. Patterning resolution, however, has not been studied for this method thus far, and is a key factor for scalable commercialization of organic optoelectronic devices. Variation of the mass flow rates of guard flow and carrier gas (*CG*) jets is one possible route to improve pattern resolution. FWHM/Base ratio and 'Useful volume' ratio are two figures of merit mentioned in **Chapter 3** for determine the pattern resolution. **Figure 7.2** shows the improvement in both of these with increase in *GF*/*CG* ratio of mass flow rates.

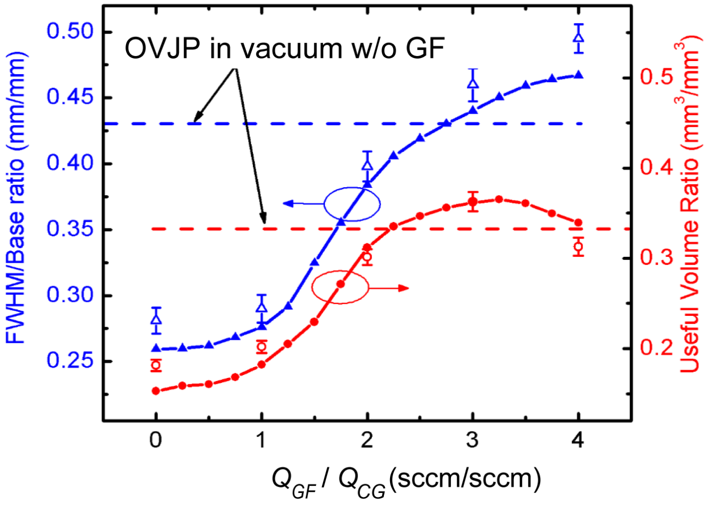

Figure 7-2. Higher FQHM/Base and 'useful volume' ratios plotted for simulated (solid symbols) and experimentally (open symbols) conditions of *GF* and *CG* mass flow rate ratios, indicate better pattern resolution and improved OLED device performance.

Previous studies have shown that choosing low molecular mass gases, like Helium, for the carrier gas reduces the dispersion of the organic vapor jet and thus improves resolution. [1,6] Additionally, varying the guard jet flow rates have a significant impact on crystallinity, roughness and device performance of the patterned films. [3] Future work involving *CG* and *GF* gases (choosing between He, N_2, Ar and CO_2) to show the effect of gas molecular weight, size and structure on the film's pattern resolution and morphology is a promising direction to undertake. Initial theoretical and experimental work has been done [7] to show that diffusivity of sublimated organic molecules and the pattern resolution can be improved by the appropriate combination of *GF*/*CG* gases and therefore enable greater flexibility in choosing deposition conditions (sublimation and substrate temperatures, mass flow rates, etc.) for a given molecular material. For example, using helium as carrier gas leads to improved pattern resolution of the deposit via lower dispersion (or spread) of organic material from the center of the deposit, enhances sublimed organic material diffusivity and subsequently the deposition rate. On the other hand, heavy molecular weight guard jet, like Ar or CO_2 further focuses the organic jet, producing a better patterned deposited and improves the shielding of the hot organic vapor from ambient oxygen and moisture while printing in air.

7.2.2. Nano- and micro- structured films

As mentioned in **Chapter 2**, unique growth modes of organic semiconductor films are available through the GF-OVJP technique, due to the flow dynamics, top-down during-deposition annealing, and gas- and film- phase nucleation mechanisms. However, the nature of film growth and crystallization behavior is not well studied and understood due to the complex molecular structures and van der Waals forces-dominated bonding in the films. During the course of this doctoral work, previously unseen morphologies were discovered while growing a number of molecular organic films, including Boron subphthalocyanine chloride (SubPc), Tris (8-hydroxyquinolinato) aluminum (Alq_3), 3,4,9,10-Perylenetetracarbonsäuredianhydrid (PTCDA). [8] These growth modes are accessed by GF- OVJP, wherein smooth films (obtained up to ~100 nm thickness) evolve into highly crystalline films that exhibit several surprising geometrical features such as spheroids, rods and platelets, at higher thicknesses, shown in **Figure 7-3**. These unique molecular film morphologies have never been reported by any existing deposition technique before. Surface evolution models coupled with material properties can be used to understand the highly kinetic and thermal flow regimes of GF-OVJP deposition and growth mechanism of these unique morphologies in the future.

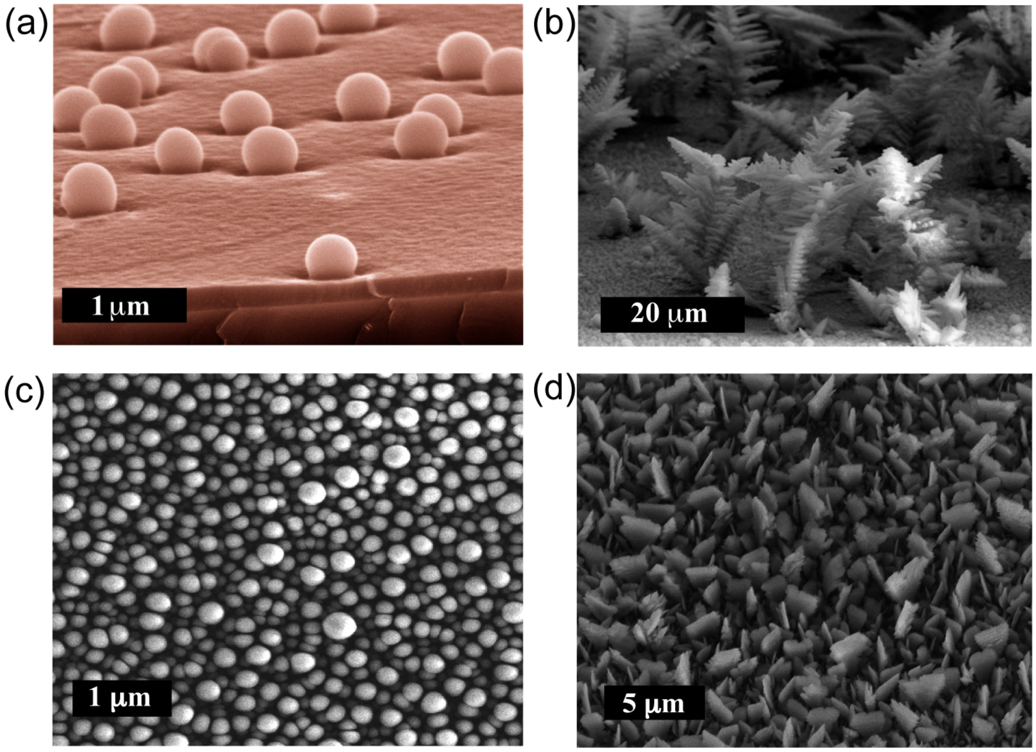

Figure 7-3. Smooth flat thin films (~100 nm) evolve in to thick films with geometric features like lobes, rods and platelets. SubPc planar films evolve into (a) nano-lobes (~800 nm) and (b) micro-ferns (20 μm). Alq_3 lobes and PTCDA plates like features in (c) and (d).

7. 3. Summary

GF-OVJP is a technique to deposit and pattern organic (and some polymer) films and devices in at any ambient conditions (in vacuum, in glovebox or in air). The versatility of the technique with its wide range of independently controllable processing parameters makes it uniquely suited not only for semiconductor material deposition, but also for exploration of surface reaction based metal or inorganic insulator deposition. Since the tool is not limited by a vacuum chamber, it can be scaled up to have multiple nozzles in an array for fabricating multilayered structure of different known materials, or large area deposits of a single materials, or performing rapid, combinatorial studies on morphologies and herterojunction physics of new materials. The nozzle can be mounted on a robotic arm for 3-dimensional motion, for deposition/patterning on non-planar curved surfaces. The possibilities are endless.

7. 4. References

[1] M. Shtein, P. Peumans, J.B. Benziger, and S.R. Forrest, "Direct mask-free patterning of molecular organic semiconductors using organic vapor jet printing", *Journal of Applied Physics* **2004**, *96*, 4500

[2] S. Biswas, K. P. Pipe, M. Shtein, "Solvent-free, direct printing of organic semiconductors in atmosphere", *Appl. Phys. Lett.* **2010**, *96*, 263301

[3] S. Biswas, K. A. Luck, M. Shtein, "Guard flow-enhanced organic vapor jet printing of photovoltaic donor materials in air", *Org. Electron.* **2012**, *13*, 2905.

[4] S. Biswas, Y. Yang, C. M. Schlepütz, N. Geva, R. L. Headrick, R. Pindak, R.

Clarke and M. Shtein, "Spatial mapping of morphology and electronic properties of air-printed pentacene thin films", *Adv. Funct. Mater.*, **2014**, (accepted).

[5] S. Biswas, T. Arbel, K. P. Pipe, M. Shtein, “Chemical vapor jet deposition of parylene in air”, **2014** (*in preparation*).

[6] G. J. McGraw, D. L. Peters, S. R. Forrest, “Organic vapor jet printing at micrometer resolution using microfluidic nozzle array”, *Appl. Phys. Lett.*, **2011**, *8*, 013302.

[7] O. Shalev, S. Biswas, D. Hinz, M. Shtein, “Influence of carrier gas and guard flow gas properties on patterning resolution of molecular semiconductor films deposited by GF-OVJP”, **2014**, (*in preparation*).

[8] O. Shalev, S. Biswas, Y. Yang, R. Clarke, W. Lu, M. Shtein, “Novel crystalline morphologies of molecular semiconductors materials”, **2014**, (*in preparation*).

APPENDIX A

Deposition profile and thickness measurement

A.1. Interferometry

In the GF-OVJP apparatus, when all upstream conditions, including T_{Ev}, T_S, Q_{CG} and Q_{GF} are fixed, the organic vapor flux exiting the nozzle is constant and has cylindrical symmetry. When the nozzle and substrate are stationary relative to each other, at a given value of s, a '*spot deposit*' is obtained which has a bell-shaped cross-sectional profile, with the feature thickness of the spot being determined by the nozzle dwell time. Analysis of the deposited pattern profiles is performed using interference microscopy for the larger patterns. This interferometry method entailed illuminating the substrates with a monochromatic source (with wavelength λ (nm) which lies outside the absorption spectrum of the organic material) and observing the interference fringes formed from the bell-shaped *spot deposit* (**Fig. A-1 a**). The thickness profile is extracted from the digitized pattern image (**Fig. A-1 b**) by counting the number of dark fringes from the edge (**Fig. A-1 c**) and using $t = \frac{(m+1/2)\lambda}{2n}$, where t is the pattern thickness, m (= 0, 1, 2, 3, etc.) is the dark fringe order from the outer edge of the deposit, and n is the refractive index of the organic material.

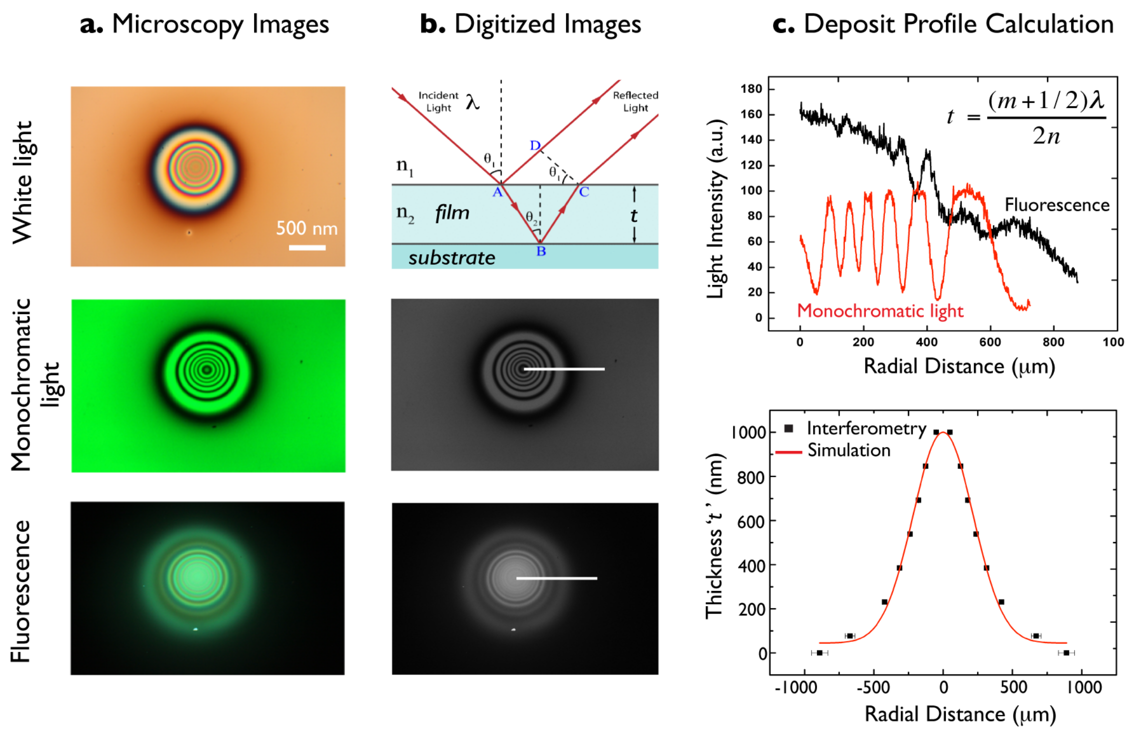

Figure A-1. Procedure to calculate spot deposit thickness profile using interferometry. (**a**) Organic material (Alq_3 here) is deposited by GF-OVJP and White light 'no filter', monochromatic light (green filter, l = 540±5 nm) and fluorescence (UV light) optical microscope images are collected. (**b**) The monochromatic and fluorescence images are digitized (converted to 8 bit, grey scale) and the light intensity is scanned across the diameter. (**c**) From the digitized monochromatic light image, dark fringes are counted from the outer edge (*m* = 0) of the deposit and thickness is calculated using the formula. The base (*t* = 0 nm) is obtained from the spread of the fluorescence image. The interferometry data is fit to the simulated profile to obtain the deposit profile.

The deposit profile is validated by simulation (FLUENT 6.3. computational fluid dynamics modeling). The obtained thickness profile is normalized (as shown in **Fig. 5-3**). Moving the nozzle relative to the substrate at a translation speed v_X, '*line deposit*s' are obtained. Line thicknesses obtained by translating the nozzle are linearly proportional to

$1/v_X$. The thickness of the line deposit is uniform in the direction of motion, while the cross-section thickness profile in the direction perpendicular to motion remains that of a spot deposit. The translation speed of the nozzle relative to the substrate, thus determines the thickness and deposition rate of the line deposit. However, the deposits are all self-similar and collapse on to the same normalized thickness profile, as is evident from **Figure A-2**.

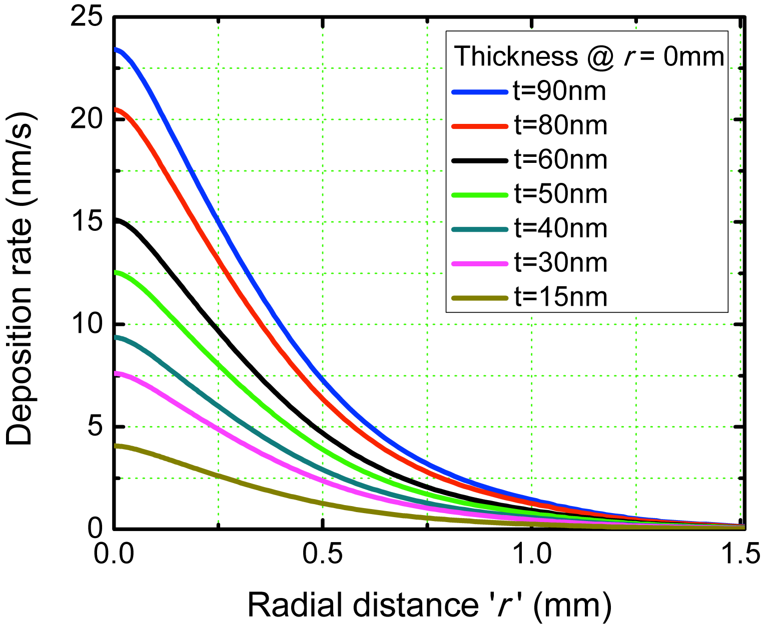

Figure A-2. Simulated deposition rate profiles obtained for different center thicknesses 't' (dependent on the nozzle translation speed v_X) shows that the profiles are self-similar and collapse on to the same normalized profile.

A.2. Ellipsometry of large area deposits

Line deposits are obtained by translating the GF-OVJP nozzle relative to the substrate at translation speed v_X. Rastering the nozzle to draw multiple parallel, adjacent lines with sufficiently narrow line spacing (e.g. 0.1 mm) allow the deposit profiles to overlap and form one "large area deposit" with uniform thickness throughout. **Figure A-3** schematically depicts the 'large area deposit' profile schematically.

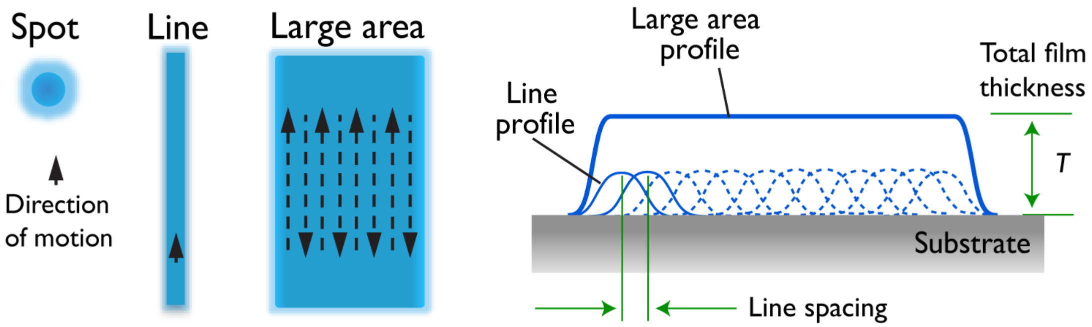

Figure A-3. Spot, line and large area deposits obtainable by GF-OVJP by varying the nozzle's translational velocity, and direction of motion. Large area deposit is comprised of several closely spaced lines, with a total thickness of T, while the line center (r = 0 mm) thickness is $t_{r=0}$.

Ellipsometry is performed on 10x10 mm2 large area deposits to obtain the thickness. It is found that these large area deposits have uniform thickness with negligible variation despite being a collection of closely spaced line deposits. The total thickness (large area) is measured by ellipsometry, and is the composite thickness of several line deposit thicknesses. The total thickness is given by $T = t_{r=0} + 2\sum t_r$, where t_r is thickness of the line deposit at a radial distance of 'r' and $t_{r=0}$ is the thickness of the line at the center. The summation over 'r' is performed at multiple of the 'line spacing'. Hence, for a particular large area deposit obtained with nozzle translation speed of v_X in the direction of motion, ellipsometry gives the total thickness and knowing the normalized thickness profile of line deposit (from interferometry and simulation), the exact thickness of the line profile can be calculated.